Implementation of a Non-Linear Eddy Viscosity Turbulence Model into Hydra-TH for Fuel Related Applications

By

Benjamin Lawrence Magolan

B.S., Nuclear, Plasma, and Radiological Engineering (2013)
University of Illinois at Urbana-Champaign

SUBMITTED TO THE DEPARTMENT OF NUCLEAR SCIENCE
AND ENGINEERING
IN PARTIAL FULFILLMENT OF THE REQUIREMENTS FOR THE DEGREE OF

MASTER OF SCIENCE IN NUCLEAR SCIENCE AND ENGINEERING
AT THE
MASSACHUSETTS INSTITUTE OF TECHNOLOGY

JUNE 2015

Signature of Author: Signature redacted
Benjamin L. Magolan
Department of Nuclear Science and Engineering
May 14, 2015

Certified by: Signature redacted
Emilio Baglietto, Ph.D
Assistant Professor of Nuclear Science and Engineering
Thesis Supervisor

Signature redacted
Kord Smith, Ph.D
KEPCO Professor of the Practice of Nuclear Science and Engineering
Thesis Reader

Accepted by: Signature redacted
Mujid S. Kazimi, Ph.D.
TEPCO Professor of Nuclear Engineering
Chair, Department Committee on Graduate Students

Implementation of a Non-Linear Eddy Viscosity Turbulence Model into Hydra-TH for Fuel Related Applications

By

Benjamin Lawrence Magolan

Submitted to the Department of Nuclear Science and Engineering on
May 14, 2015
in Partial Fulfillment of the Requirements for the degree of

Master of Science in Nuclear Science and Engineering

Abstract

A quadratic *k-ε* non-linear eddy viscosity model (NLEVM) has been implemented into Hydra-TH, a Computational Fluid Dynamics (CFD) software being developed to support the nuclear reactor thermal-hydraulics modeling and simulation needs of the CASL program. This model adopts a non-linear extension of the stress-strain relationship that allows it to capture the anisotropy of flow conditions. Modeling this behavior is essential for the accurate simulation and prediction of the flow profile in fuel rod arrays, where secondary flow vortices arise and act to modify the flow profile. The quadratic model formulation in the greater context of Reynolds-Averaged Navier-Stokes (RANS) turbulence modeling is first presented. This is followed by a discussion of the key aspects of the standard and quadratic *k-ε* model implementations, which have been incorporated into the Hydra-TH source code to supplement the already fully-functioning RNG *k-ε* model. The three *k-ε* model variants are then applied to the 'classic' engineering test cases of flow in a square duct and a U-channel bend in order to highlight the relative merits and deficiencies of the quadratic model. Next, the quadratic model is validated on triangular and square rod fuel array test cases that are representative of the flow profile that develops in nuclear reactor subchannels. This thesis concludes with a rigorous sensitivity study of the triangular fuel rod array simulations, whereby guidelines and best practices for the quadratic model's use for nuclear fuel related applications are derived.

Thesis Supervisor: Emilio Baglietto
Title: Assistant Professor of Nuclear Science and Engineering

Thesis Reader: Kord Smith
Title: KEPCO Professor of the Practice of Nuclear Science and Engineering

Acknowledgements

I am truly grateful for the guidance, support, and wisdom offered by Emilio Baglietto, who not only served as my research advisor, but also calibrated the quadratic model coefficients during the course of his own Ph.D. studies—my work would therefore not be possible without his contributions. I would also like to thank my Hydra-TH comrades, Mark Christon (Los Alamos National Laboratory) and Thomas Smith (Sandia National Laboratories), for working closely with me on both the implementation and validation of the quadratic model. And lastly, I would like to thank Knolls Atomic Power Laboratory (KAPL), the Rickover Fellowship Program, and the CASL project for funding this research endeavor.

Table of Contents

List of Figures

List of Tables

Nomenclature

In this chapter, all symbols, expressions, notations, abbreviations and acronyms used in this text are defined.

Mathematical Notation

Notation	Unit (SI)	Definition
D_e	m	Equivalent diameter
k	$m^2\ s^{-1}$	Turbulent kinetic energy
U	$m\ s^{-1}$	Instantaneous velocity
$\bar{u}$	$m\ s^{-1}$	Time-averaged velocity
u'	$m\ s^{-1}$	Fluctuating velocity component
P	Pa	Instantaneous pressure
$\bar{p}$	Pa	Time-averaged pressure
p'	Pa	Fluctuating pressure component
P_k	$Pa\ s^{-1}$	Production of turbulent kinetic energy
Re	--	Reynolds number
S	--	Mean shear invariant
S_{ij}	s^{-1}	Mean strain rate tensor
V_b	$m\ s^{-1}$	Bulk velocity
$y+$	--	Non-dimensional wall distance

Greek Letters

Notation	Unit (SI)	Definition
δ_{ij}	--	Kronecker delta
ε	$m^2\ s^{-3}$	Turbulent dissipation rate
μ	$kg\ m^{-1}\ s^{-1}$	Dynamic viscosity
μ_t	$kg\ m^{-1}\ s^{-1}$	Turbulent viscosity
υ	$m^2\ s^{-1}$	Kinematic viscosity
ρ	$kg\ m^{-3}$	Density
τ_{ij}	Pa	Reynolds stress tensor
τ_w	Pa	Wall shear stress
Ω	--	Mean rotation invariant
Ω_{ij}	s^{-1}	Mean rotation rate tensor
ω	s^{-1}	Specific dissipation rate

Abbreviations

Abbreviation	Definition
ALE	Arbitrary Lagrangian-Eulerian
ASM	Algebraic Reynolds Stress Model
CASL	Consortium for Advanced Simulation of LWRs
CCINS	Cell-Centered Incompressible Navier-Stokes
CFD	Computational Fluid Dynamics
CIPS	CRUD-Induced Power Shift

CRUD	Chalk River Unidentified Deposit
DES	Detached Eddy Simulation
DNB	Departure from Nucleate Boiling
DNS	Direct Numerical Simulation
DOE	Department of Energy
EARSM	Explicit Algebraic Reynolds Stress Model
EVM	Eddy Viscosity Model
GTRF	Grid-to-Rod Fretting
LES	Large Eddy Simulation
LEVM	Linear Eddy Viscosity Model
LWR	Light Water Reactor
MAMBA	MPO Advanced Model for Boron Analysis
NLEVM	Non-Linear Eddy Viscosity Model
PCI	Pellet-Cladding Interaction
PWR	Pressurized Water Reactor
RANS	Reynolds-Averaged Navier-Stokes
RNG	Re-Normalization Group
RSM	Reynolds Stress Model
SST	Shear Stress Transport
VERA	Virtual Environment for Reactor Applications

1 Introduction

The Consortium for Advanced Simulation of LWRs (CASL) project is a Department of Energy (DOE) initiative to develop a fleet of simulation capabilities to guide the design and optimization of light water reactors. Hydra-TH represents one of the simulation tools, as it is a computational fluid dynamics (CFD) software that is being developed to address the thermal-hydraulics modeling and simulation aspects of light water reactors. Great care is being taken to equip the code with numerical solvers and turbulence models that will maximize its performance and yield accurate predictions for the coolant distribution in the complex geometries intrinsic to nuclear reactor fuel assemblies.

Detailed prediction of the flow distribution inside fuel assemblies is essential for the design and safe operation of nuclear systems. Since the flow distribution cannot be calculated with exact analytical methods, numerical modeling and CFD simulation are needed to characterize this behavior. The high Reynolds number flows characteristic of nuclear reactor fuel assemblies preclude the use of Direct Numerical Simulation (DNS) and Large Eddy Simulation (LES) for full assembly and core calculations. Practical engineering CFD simulations must therefore be based on the Reynolds-Averaged Navier-Stokes (RANS) equations with appropriate turbulence modeling. It is therefore of paramount interest to design and implement RANS turbulence models that are capable of resolving these complex flow structures.

The coolant flow distribution in a fuel assembly is a highly complex, anisotropic phenomenon. The complicated flow structure and turbulence redistribution has been observed in numerous fuel bundle experiments (e.g. Trupp and Azad [1]; Carajilescov and Todreas [2]; Rehme [3]). Anisotropy in the near-wall region leads to the formation of a secondary flow that spirals through the bundle. The secondary motion acts to redistribute the flow and smooth out wall shear stress and axial velocity profiles. Such flows—termed secondary flow of Prandtl 2nd kind—were originally postulated by Nikuradse [4] in 1926, but eluded experimental measurement until 1988 when Vonka [5] demonstrated that such flows are approximately 0.1% that of the primary velocity by using laser Doppler velocimetry.

A myriad of two-equation RANS turbulence models have been developed (e.g. k-ε, k-ω, SST). Such models are predicated on the Boussinesq hypothesis, which assumes the turbulent stresses are proportional to the mean velocity gradients of the flow. This approximation assumes that the eddy viscosity is isotropic, and is therefore incapable of capturing the anisotropy of the Reynolds stresses. Reynolds Stress Models (RSM) can be used to model the flow anisotropy. However, the higher order correlations—although rigorous in their mathematical derivation—are routinely modeled with approximations of unknown validity as it is difficult to associate physically meaningful quantities to these higher order terms.

Non-linear eddy viscosity models (NLEVM) are an extension of standard two-equation turbulence models, whereby a non-linear stress-strain relationship is applied. The concept of NLEVMs originated from Lumley [6] and Pope [7], who demonstrated that a generalized non-linear stress-strain relationship was mathematically equivalent to an explicit algebraic Reynolds stress model (EARSM). The most general formulation is cubic in nature, with the cubic terms pertaining to streamline curvature and rotation. The quadratic terms capture the normal stress anisotropy and have been demonstrated to be sufficient for fuel related applications [8] [9].

A quadratic formulation of the NLEVM has therefore been implemented in Hydra-TH in order to enhance the simulation capability of reactor systems and support the goals of the CASL program. Implementation of this quadratic model necessitated the restructuring of the code architecture—in particular, the k-ε class structure and inheritance schemes—and an explicit treatment of the quadratic stress terms in the momentum equation. The model implementation has been validated through simulation of test cases for triangular and square rod fuel arrays.

1.1 Hydra-TH in VERA

A series of challenge problems that characterize the key phenomena of pressurized water reactors (PWR) have been identified as part of the CASL project. These challenge problems include (among others) grid-to-rod fretting (GTRF), CRUD-induced power shift (CIPS), pellet-clad interaction (PCI), and departure from nucleate boiling (DNB). In order to address these challenge problems through application of modeling and simulation strategies, the virtual environment for reactor applications (VERA) framework has been established.

VERA is not a single simulation tool, but rather a collection of codes and toolkits that can be utilized in combination to address the challenge problems. These toolkits aim to model and simulate the complicated physics of the reactor environment such as radiation transport (MPACT, Insilico), fuel performance (Peregrine), CRUD chemistry and deposition (MAMBA), and structural dynamics and solid mechanics (SIERRA/SDSM). Hydra-TH addresses the fluid dynamics and thermal-hydraulics aspects of nuclear reactor modeling.

Hydra-TH is a hybrid finite-element/finite-volume incompressible/low-Mach solver that is written in C++. The software has the ability to handle unstructured, hybrid mesh elements including tetrahedral, hexahedral, polyhedral, and wedge pyramidal. It supports multiple turbulence models that include LES, detached eddy simulation (DES), Spalart-Allmaras, and RNG k-ε. An arbitrary Lagrange-Eulerian (ALE) formulation has been implemented in order to facilitate modeling of fluid-structure interaction problems such as GTRF. A multi-field solver is also being integrated into the code to advance the capability for simulation of both multiphase (e.g. liquid-vapor) and multi-species (e.g. boron-liquid) flows.

All transported variables are cell-centered. A Lax-Friedrichs advective flux approximation in conjunction with Barth and Jesperson [10] flux limiting is utilized in order to preserve monotonicity. Gresho's second-order "P2" projection method serves as the pressure-velocity coupling scheme [11] [12]. Since the pressure is not collocated with velocity, a Rhie-Chow interpolation scheme is not needed. A non-linear Picard iterative scheme has also been implemented to extend the projection method to a fully-implicit treatment that facilitates large time-steps [13].

The incompressible Navier-Stokes flow solver has undergone a rigorous verification and validation study for 2D and 3D benchmark problems that include Pouiseuille flow, natural convection in a square cavity, and turbulent channel flow [14]. Further, the Hydra-TH software has been used to model GTRF using LES [15] as well as single-phase flow heat transfer in a rod bundle segment using RANS turbulence models [16]. A rigorous validation of the code applied to nuclear fuel applications has also been performed for both the RANS and LES turbulence models [17]. Additional work is in progress to identify and establish a collection of turbulence benchmark problems, referred to as "torture tests," to further aid model development and testing [18].

1.2 Objectives

The objectives of this thesis are organized as follows:

1. To implement the standard and quadratic k-ε turbulence models into Hydra-TH
2. To perform a comprehensive and rigorous validation study of the quadratic k-ε model applied to nuclear reactor test cases
3. To derive best practices for the quadratic k-ε model's application to nuclear fuel applications

1.3 Structure of the Thesis

Chapter 2 provides a necessary introduction to RANS turbulence modeling in Hydra-TH. First, the formulation of the Reynolds-Averaged Navier-Stokes (RANS) equations will be presented. A discussion of eddy viscosity models (EVMs) and Reynolds stress models (RSMs) is also provided in order to highlight the merits and limitations of each. This establishes the framework for a more thorough discussion that delves into the mathematical formulation of the standard and quadratic k-ε models, which were implemented into Hydra-TH during the course of this work.

Chapter 3 chronicles the process of model implementation into the Hydra-TH source code. The restructuring of the k-ε class architecture and inheritance scheme to accommodate the incorporation of the standard and quadratic models are first discussed. Next, the integration of these models with the remainder of the source code is presented. This includes topics such as the explicit treatment of the quadratic terms in the momentum equation, parsing commands for user-specification, and bookkeeping with auxiliary functions.

Chapter 4 presents the results of quadratic, standard, and RNG k-ε models applied to the 'classic' engineering test cases of flow in a square duct and U-channel bend. The test case for the square duct demonstrates the strength of the quadratic model in resolving the secondary flows that arrive in complex geometries. Likewise, the U-channel bend test case demonstrates the limitations of the quadratic model for capturing the effects of streamline curvature and rotation, which require the cubic formulation for adequate prediction.

Chapter 5 provides an assessment for the quadratic model applied to bare rod array experimental data that is representative of nuclear fuel assembly configurations. The triangular array of Mantlik et al. [19] and the square array of Hooper and Wood [20] are both examined. This is used to glean insights and recommendations for the model's applications to fuel related applications as well as highlight future areas of work for the Hydra-TH toolkit.

Chapter 6 presents the results of a rigorous sensitivity study that has been performed for the triangular fuel rod array experiments conducted by Mantlik et al. [19]. The treatment of the near-wall region, size of the computational domain, axial grid refinement, and time integration scheme are each explored, and their impact on the resulting simulation convergence, performance, and run-time are all explored.

Chapter 7 concludes this work by highlighting future areas of improvement for the quadratic NLEVM, as well as commenting on the model's readiness for nuclear applications.

2 Background

The continuity and momentum conservation equations are used to describe the behavior of a fluid element as it travels through a domain of interest. Together, these two equations are collectively referred to as the Navier-Stokes equations, which assume the following form in Cartesian tensor notation:

$$\frac{\partial \rho}{\partial t} + \frac{\partial(\rho U_i)}{\partial x_i} = 0 \tag{2.1}$$

$$\frac{\partial(\rho U_i)}{\partial t} + \frac{\partial(\rho U_i U_j)}{\partial x_j} = -\frac{\partial P}{\partial x_i} + \frac{\partial}{\partial x_j}\left(\mu \frac{\partial U_i}{\partial x_j}\right) \tag{2.2}$$

Here, U is the instantaneous velocity, P is the instantaneous pressure, ρ is the density, μ is the dynamic viscosity, and the subscripts i and j denote the coordinate direction (i.e. x, y, z). During the course of this study, constant fluid properties and incompressible flow are modeled. For an incompressible flow, the density of a fluid element does not change in time as it flows through space. The continuity equation therefore does not act as a mass conservation equation, but rather as a constraint on the behavior of the velocity field, whereby the divergence of the velocity field is mandated to be zero:

$$\frac{\partial(U_i)}{\partial x_i} = 0 \tag{2.3}$$

The Reynolds number is a non-dimensional number that is used as a metric to characterize the flow behavior and is defined as follows:

$$Re = \frac{\rho U L}{\mu} \tag{2.4}$$

Here, L is a characteristic length of the domain, which for nuclear fuel assemblies is taken to be the equivalent diameter of the coolant subchannel. For laminar flow ($Re < 2{,}000$), the flow profile is uniform and the form of the instantaneous Navier-Stokes equations expressed in Eqs. (2.2) and (2.3) is suitable for characterizing the flow behavior. However, for turbulent flow ($Re > 2{,}000$-$10{,}000$), the flow profile consists of random, small-scale, chaotic perturbations as depicted in Figure 2.1.

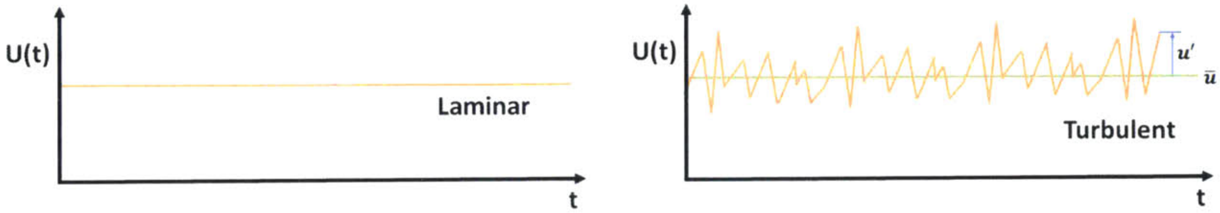

Figure 2.1 Laminar vs. turbulent flow

A time-averaging procedure is used to derive the RANS equations, which can be used to provide a statistical treatment of the turbulent phenomena. This averaging process introduces an additional term into the momentum equation that captures these turbulent fluctuations and must be modeled through the application of a suitable turbulence model. A broad spectrum of RANS-based turbulence models have been devised in order to model these fluctuating components, which vary with respect to their mathematical rigor, physical appropriateness, and computational cost. A schematic of this spectrum is presented in Figure 2.2.

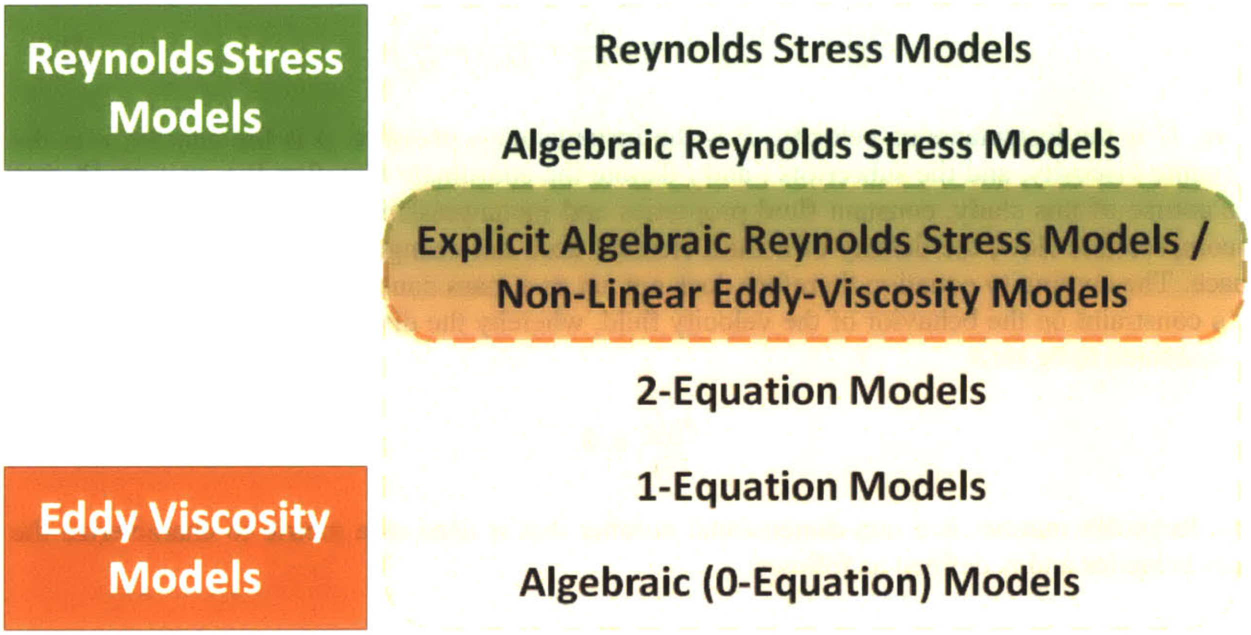

Figure 2.2 RANS turbulence modeling spectrum

In the subsequent text, a brief introduction to RANS turbulence modeling is established in order to provide context and motivation for the selection of the non-linear eddy viscosity model (NLEVM) that was implemented into Hydra-TH during the course of this work.

2.1 RANS Equations

The Reynolds-averaged Navier-Stokes equations are time-averaged equations for the motion of fluid. A Reynolds decomposition is performed, whereby an instantaneous field quantity (A) is separated into its mean ($\bar{a}$) and fluctuating components (a'), as displayed in Figure 2.1. The resulting decomposition of the pressure and velocity terms is:

$$\boldsymbol{U}(\boldsymbol{x},t) = \overline{\boldsymbol{u}}(\boldsymbol{x},t) + \boldsymbol{u}'(\boldsymbol{x},t) \tag{2.5}$$
$$P(\boldsymbol{x},t) = \bar{p}(\boldsymbol{x},t) + p'(\boldsymbol{x},t) \tag{2.6}$$

whereby a time-averaged quantity is defined as:

$$\bar{a}(\boldsymbol{x},t) = \frac{1}{T}\int_0^T A(\boldsymbol{x},t)\,dt \tag{2.7}$$

Substitution of the decomposed pressure and velocity terms into the instantaneous form of the Navier-Stokes equations—Eqs. (2.2) and (2.3)—yields the following result:

$$\frac{\partial(\bar{u}_i+u_i')}{\partial x_i}=0 \tag{2.8}$$

$$\frac{\partial\rho(\bar{u}_i+u_i')}{\partial t}+\frac{\partial\rho(\bar{u}_i+u_i')(\bar{u}_j+u_j')}{\partial x_j}=-\frac{\partial(\bar{p}+p')}{\partial x_i}+\frac{\partial}{\partial x_j}\left(\mu\frac{\partial(\bar{u}_i+u_i')}{\partial x_j}\right) \tag{2.9}$$

After further time-averaging of the resulting equations and through application of the following averaging principles,

$$\bar{\bar{a}}=\bar{a} \tag{2.10}$$

$$\overline{a+b}=\bar{a}+\bar{b} \tag{2.11}$$

$$\overline{a'}=0 \tag{2.12}$$

$$\overline{a'\bar{b}}=0 \tag{2.13}$$

$$\overline{\frac{\partial a}{\partial x}}=\frac{\partial\bar{a}}{\partial x} \tag{2.14}$$

Eqs. (2.8) and (2.9) can be simplified to the following form:

$$\frac{\partial(\bar{u}_i)}{\partial x_i}=0 \tag{2.15}$$

$$\frac{\partial(\rho\bar{u}_i)}{\partial t}+\frac{\partial(\rho\bar{u}_i\bar{u}_j)}{\partial x_j}=-\frac{\partial\bar{p}}{\partial x_i}+\frac{\partial}{\partial x_j}\left(\mu\frac{\partial\bar{u}_i}{\partial x_j}\right)-\frac{\partial(\rho\overline{u_i'u_j'})}{\partial x_j} \tag{2.16}$$

Inspection of the resulting RANS equations reveals that all but one of the terms are based on time-averaged quantities. The final term in Eq. (2.16) is called the Reynolds Stress tensor, which denotes the additional momentum transport due to the turbulent fluctuations in the velocity field. This tensor is symmetric and has six unique quantities. Appropriate closure of this term requires the application of a turbulence model, as depicted in Figure 2.2.

2.2 Eddy Viscosity Models

Eddy viscosity models are predicated on the Boussinesq hypothesis, which assumes that the turbulent stresses are proportional to the mean velocity gradients of the flow:

$$\tau_{ij}=-\rho\overline{u_i'u_j'}=\mu_t\left(\frac{\partial\bar{u}_i}{\partial x_j}+\frac{\partial\bar{u}_j}{\partial x_i}\right)-\frac{2}{3}\rho k\delta_{ij} \tag{2.17}$$

This proportionality constant is termed the turbulent (or eddy) viscosity μ_t. In contrast to the molecular viscosity μ, this term is not a fluid property, but rather depends on the turbulence structures in the flow. Consequently, the turbulent viscosity can vary considerably throughout the flow domain. The turbulent kinetic energy (per unit mass) k describes the energy of these turbulent eddies in the flow:

$$k=\frac{1}{2}\left(\overline{u'^2}+\overline{v'^2}+\overline{w'^2}\right) \tag{2.18}$$

Here, the terms *u'*, *v'*, and *w'* represent the fluctuating velocity components in the *x*, *y*, and *z* directions, respectively. The definition of the mean strain rate tensor S_{ij} can be used to simplify the formulation of the Reynolds stress tensor in Eq. (2.17) as follows:

$$S_{ij} = \frac{1}{2}\left(\frac{\partial \bar{u}_i}{\partial x_j} + \frac{\partial \bar{u}_j}{\partial x_i}\right) \tag{2.19}$$

$$\tau_{ij} = 2\mu_t S_{ij} - \frac{2}{3}\rho k \delta_{ij} \tag{2.20}$$

The first term on the right hand side of Eq. (2.20) represents a linear constitutive relation between the stress and strain exerted on a fluid element. Hence, models based on this formulation are commonly referred to as linear eddy viscosity models (LEVM). The second term enforces the condition that the sum of the normal stresses is equal to $2k$ in flow regimes where the velocity gradients are equal to zero, as is mandated by Eq. (2.18).

The primary goal of eddy viscosity models is to devise a way to calculate the turbulent viscosity μ_t. Various model formulations exist, including algebraic, one-equation, and two-equation models. In general, algebraic (zero-equation) and one-equation models suffer from an incomplete formulation as a mixing length that is geometry-dependent needs to be specified by the user, and therefore are not discussed here. (An exception to this claim is the Spalart-Allmaras model [21], in which a one-equation model is used to solve a single transport equation for the turbulent viscosity). For a complete discussion on turbulent viscosity models, the interested reader is referred to Pope, Chapter 10 [22].

Two-equation models have been by far the most popular for a diverse array of engineering and research applications. Such models consist of two independent transport equations, one for the turbulent kinetic energy *k*, and one for an equivalent turbulent length scale parameter. Specification of two transport variables leads to a complete model, in which no additional information about the flow regime (e.g. mixing length) is needed to model the turbulence. Examples of turbulent length scale parameters include the turbulent dissipation rate ε in the standard k-ε model by Launder and Sharma [23], the specific dissipation ω in the k-ω model by Wilcox [24], and the turbulent time scale τ ($=1/\omega$) in the k-τ model by Speziale et al. [25]. Further, the shear stress transport (SST) model posed by Menter [26] is a hybrid of the k-ε and k-ω models, whereby a blending function—in combination with a multitude of limiters—is used to enforce the k-ω model in the near wall region and the k-ε model in the bulk flow.

Linear eddy viscosity models are limited by the two main assumptions used to construct them: namely, local equilibrium and turbulent stress isotropy. The local equilibrium assumption posits that the production and dissipation of turbulent kinetic energy are equal locally. The transport effects of these turbulent stresses are neglected, which therefore assumes that the history of the flow profile is negligible. In short, the turbulent viscosity is modeled at a moment in time in the domain whereby the Reynolds stresses change instantaneously when the mean rate of strain changes.

The linear stress-strain relationship also leads to turbulent stress isotropy, in which the turbulent fluctuations *u'*, *v'*, and *w'* are assumed to be locally isotropic or equal. The assumption of isotropy implies that one component of the turbulent stress (e.g. *u'u'*) does not affect the other stress components (*v'v'*, *w'w'*). In reality, the turbulent stress in one direction indeed affects the stresses in the other directions (e.g. much like the act of stretching a rubber band in one direction, which causes it to shrink in the lateral directions). This physical process is referred to as turbulent normal stress anisotropy.

Two-equation LEVMs work well for simple turbulent shear flows, where the turbulence characteristics and mean velocity gradients change relatively slowly (e.g. round jet, channel flow, mixing layer). However, models based on this framework break down in complicated flows where there are sudden changes in the mean flow strain rate such as flow impinging against a wall, curved surfaces, secondary flows, and swirling, in which the modeling assumptions of local equilibrium and turbulent stress isotropy are grossly violated. More advanced turbulence models have therefore been devised in order to address these phenomena.

2.3 Reynolds Stress Models

Reynolds stress models (RSM) consist of solving six differential transport equations to calculate the individual Reynolds stresses (*u'u'*, *v'v'*, *w'w'*, *u'v'*, *u'w'*, *v'w'*). The idea was pioneered by Rotta 1951 [27], but was not formalized into a complete Reynolds stress closure form until Launder et al. 1975 [28]. There have been many forms of the model correlations, examples of which include the linear pressure strain formulation of Gibson and Launder 1978 [29] and the quadratic pressure strain of Speziale et al. 1991 [30]. The transport equations for the six Reynolds stress terms are defined as follows:

$$\frac{\partial(\tau_{ij})}{\partial t}+\frac{\partial(\bar{u}_k\tau_{ij})}{\partial x_k}= -\frac{\partial(T_{kij})}{\partial x_k}+\mathrm{P_{ij}}+\Phi_{\mathrm{ij}}-\epsilon_{\mathrm{ij}} \tag{2.21}$$

where

$$T_{kij} = \rho\overline{u_i'u_j'u_k'}+\overline{p'(\delta_{kj}u_i'+\delta_{ik}u_j')} - \mu\frac{\partial\left(\overline{u_i'u_j'}\right)}{\partial x_k} \tag{2.22}$$

$$P_{ij} = -\rho\left(\overline{u_i'u_k'}\frac{\partial\bar{u}_j}{\partial x_k}+\overline{u_j'u_k'}\frac{\partial\bar{u}_i}{\partial x_k}\right) \tag{2.23}$$

$$\Phi_{ij} = \overline{p'\left(\frac{\partial u_i'}{\partial x_j}+\frac{\partial u_j'}{\partial x_i}\right)} \tag{2.24}$$

$$\epsilon_{\mathrm{ij}} = 2\mu_{\mathrm{t}}\overline{\frac{\partial u_i'}{\partial x_k}\frac{\partial u_j'}{\partial x_k}} \tag{2.25}$$

are the Reynolds flux, production, pressure-rate-of-strain, and dissipation tensors, respectively. The Reynolds flux tensor T_{kij} corresponds to the diffusion due to turbulent convection, pressure transport, and molecular viscous transport, respectively. The pressure-rate-of-strain Φ_{ij} is considered to be a composite of slow, rapid, and harmonic components that act to redistribute the flow to return the turbulence levels to isotropy as they decay.

RSMs are classified as a second moment closure, which unfortunately consist of higher order terms that need to be modeled. The production term P_{ij} is closed since it is defined in terms of the Reynolds stresses, which are the quantities being solved for at this level. All remaining terms on the right hand side of Eq. (2.21)—with the exception of the molecular diffusion term—require modeling to close the systems of equations. A full discussion on the development and formulation of adequate closure relations is beyond the scope of this discussion, and the interested reader is referred to Pope, Chapter 11 [22] and Durbin and Reif, Chapter 7 [31].

This, in essence, represents the challenge of turbulence modeling. While higher order closure relations can be derived to model all six components of the Reynolds stresses, the resulting formulations consist of even higher order terms that need to be closed. The identification of appropriate physical mechanisms to describe these higher order terms (e.g. the triple fluctuating velocity field $\overline{u_i'u_j'u_k'}$) can be quite difficult. Further, the assumptions used to approximate these higher order terms have unknown validity in many cases.

In comparison to LEVMs, RSMs require considerably more computational resources as six transport equations need to be solved, and demonstrate a higher sensitivity to the computational mesh resolution. Consequently, LEVMs are the preferred choice for most simple engineering applications. However, RSMs are routinely employed for more complex flow scenarios where modeling the effects of normal stress anisotropy are critical, such as cyclone separators, swirlers, and combustors.

2.3.1 Algebraic RSMs

Algebraic Reynolds stress models (ASM) are an attempt to reduce the computational complexity of RSMs while still preserving the ability to model the Reynolds stress tensor. Rodi 1972 [32], 1976 [33] pioneered this approach by simplifying the six partial differential equations into a set of algebraic equations. This was accomplished through the application of a "weak-equilibrium" assumption, whereby the transport of the Reynolds stress terms was assumed to be proportional to the advection of the turbulent kinetic energy k, and the diffusion of the Reynolds stress terms in Eq. (2.22) was assumed to be negligible. These assumptions lead to the simplification of Eq. (2.21) to the following form:

$$\frac{\rho\overline{u_i'u_j'}}{k}(P_k - \epsilon) = \mathrm{P_{ij}} + \Phi_{\mathrm{ij}} - \frac{2}{3}\rho\epsilon\delta_{\mathrm{ij}} \tag{2.26}$$

Here, P_k and ε are the production and dissipation of k. Likewise, P_{ij} and Φ_{ij} are the production and pressure-rate-of-strain tensors, as defined in Eqs. (2.23) and (2.24), respectively. Transport equations for k and ε also need to be solved, which is accomplished through application of the two-equation k-ε turbulence model.

While ASMs reduce the complexity of RSMs in order to model the Reynolds stresses, the equation is implicit in nature since the Reynolds stress term appear on both sides of Eq. (2.26). An iterative scheme is therefore needed to solve these coupled set of non-linear equations, which poses issues with respect to numerical stability and convergence for complex flows. Consequently, the application of ASMs to engineering flows is not a common practice and has been almost entirely abandoned altogether.

2.3.2 Explicit Algebraic RSMs

ASMs, while a considerable step in the right direction for turbulence anisotropy modeling, are plagued by a couple of deficiencies. These include the fact that the set of algebraic equations still consist of higher order terms (i.e. the production P_{ij} and pressure-rate-of-strain Φ_{ij} tensors) that require modeling simplifications of unknown validity. Further, the implicit nature of the equations poses numerical issues. These observations influenced the pursuit and development of an explicit constitutive relation for the Reynolds stress tensor. Models based on this framework are classified as explicit algebraic Reynolds stress models (EARSM).

The formulation of EARSMs originated with Lumley and Pope. It was Lumley 1970 [6] who first suggested the possibility of a constitutive relation to characterize the non-linearity of turbulence. Pope 1975 [7] mathematically derived this non-linear turbulent constitutive relation using the Cayley-Hamilton theorem and invariance principles applied to the second rank mean velocity gradient tensor. The resulting explicit expression for the Reynolds stress tensor is defined as:

$$\begin{aligned} \rho\overline{u_i'u_j'} &= \tfrac{2}{3}\rho k\delta_{ij} - 2\mu_t S_{ij} \\ &+ 4\mu_t \frac{k}{\epsilon}\left\{C_1\left[S_{ik}S_{kj} - \tfrac{1}{3}\delta_{ij}S_{kl}S_{kl}\right] + C_2\left[\Omega_{ik}S_{kj} + \Omega_{jk}S_{ki}\right] + C_3\left[\Omega_{ik}\Omega_{jk} - \tfrac{1}{3}\delta_{ij}\Omega_{kl}\Omega_{kl}\right]\right\} \\ &+ 8\mu_t \frac{k^2}{\epsilon^2}\left\{C_4\left[\Omega_{lj}S_{ki}S_{kl} + \Omega_{li}S_{kj}S_{kl}\right] + C_5\left[\Omega_{il}\Omega_{lm}S_{mj} + \Omega_{mj}\Omega_{lm}S_{il} - \tfrac{2}{3}S_{lm}\Omega_{mm}\Omega_{nl}\delta_{ij}\right]\right\} \\ &+ 8\mu_t \frac{k^2}{\epsilon^2}\left\{C_6\left[S_{kl}S_{kl}S_{ij}\right] + C_7\left[\Omega_{kl}\Omega_{kl}S_{ij}\right]\right\} \end{aligned} \tag{2.27}$$

where the mean strain rate S_{ij} and mean rotation rate Ω_{ij} tensors are defined as:

$$S_{ij} = \frac{1}{2}\left(\frac{\partial \bar{u}_i}{\partial x_j} + \frac{\partial \bar{u}_j}{\partial x_i}\right) \tag{2.28}$$

$$\Omega_{ij} = \frac{1}{2}\left(\frac{\partial \bar{u}_i}{\partial x_j} - \frac{\partial \bar{u}_j}{\partial x_i}\right) \tag{2.29}$$

After further model development and CFD experience, the non-linear constitutive relation in Eq. (2.27) has been simplified to the following form:

$$\begin{aligned} \rho\overline{u_i'u_j'} &= \tfrac{2}{3}\rho k\delta_{ij} - 2\mu_t S_{ij} \\ &+ 4\mu_t \frac{k}{\epsilon}\left\{C_1\left[S_{ik}S_{kj} - \tfrac{1}{3}\delta_{ij}S_{kl}S_{kl}\right] + C_2\left[\Omega_{ik}S_{kj} + \Omega_{jk}S_{ki}\right] + C_3\left[\Omega_{ik}\Omega_{jk} - \tfrac{1}{3}\delta_{ij}\Omega_{kl}\Omega_{kl}\right]\right\} \\ &+ 8\mu_t \frac{k^2}{\epsilon^2}\left\{C_4\left[S_{ki}\Omega_{lj} + S_{kj}\Omega_{li}\right]S_{kl} + C_5\left[S_{kl}S_{kl} - \Omega_{kl}\Omega_{kl}\right]S_{ij}\right\} \end{aligned} \tag{2.30}$$

The first line in Eq. (2.30) is the linear stress-strain relation provided by the Boussinesq hypothesis. The quadratic terms on the second line capture the effects of normal stress anisotropy. Lastly, the cubic terms on the final line denote the contributions due to curvature and rotation, respectively.

EARSMs are an extension of the linear eddy viscosity models described in Section 2.2, whereby a two-equation model (typically the k-ε model) is solved. The non-linear constitutive relation in Eq. (2.30) is substituted in place of the linear assumption defined by the Boussinesq hypothesis (Eq. (2.17)).

Most EARSM turbulence models adopt the relation for the turbulent stresses displayed in Eq. (2.30). Examples of such models include the formulations by Shih-Zhu-Lumley [34], Craft-Launder-Suga [35], Lien-Chen-Leschziner [36], and Baglietto-Ninokata [37]. Where such models differ, however, is with respect to the prescription of model coefficients (i.e. C_1-C_5). These differences arise from variances in the calibration methodology and access to experimental/DNS data that was used to tune the coefficients.

As a final thought, let us reconsider Figure 2.2 in the context of non-linear constitutive stress-strain relations. The expression in Eq. (2.30) can be derived starting from an RSM and adopting simplifying assumptions to lead to the desired formulation; this process typically leads to the naming convention of an explicit algebraic Reynolds stress model (EARSM). Correspondingly, Eq. (2.30) can also be formulated by starting with a two-equation linear eddy-viscosity model (LEVM) and tacking on the quadratic and cubic non-linear terms; this process typically leads to the naming convention of a non-linear eddy viscosity model (NLEVM). Note that both formulations—NLEVMs and EARSMs—are mathematically equivalent, and represent a nice balance of the anisotropic modeling capabilities of RSMs and the computational speed/stability features of LEVMs.

2.4 *k-ε* Turbulence Modeling in Hydra-TH

During the course of this work, the standard *k-ε* and quadratic *k-ε* (NLEVM) model formulations were implemented into Hydra-TH to supplement the already present RNG *k-ε* formulation. The precise formulations of these three models are each discussed in order.

2.4.1 Standard k-ε Model

Jones and Launder 1972 [38] are credited with the development of the 'standard' *k-ε* model, with modifications to the model coefficients later provided by Launder and Sharma 1974 [23]. (Note that significant earlier contributions to the model development include Davidov [39], Harlow and Nakayama [40], and Hanjalic [41]). The turbulent kinetic energy (per unit mass) *k* and turbulent dissipation rate *ε* transport equations are defined as:

$$\frac{\partial}{\partial t}(\rho k) + \frac{\partial(\rho u_j k)}{\partial x_j} = \frac{\partial}{\partial x_j}\left[\left(\mu + \frac{\mu_t}{\sigma_k}\right)\frac{\partial k}{\partial x_j}\right] + P_k - \rho\epsilon \tag{2.31}$$

$$\frac{\partial}{\partial t}(\rho\epsilon) + \frac{\partial(\rho u_j \epsilon)}{\partial x_j} = \frac{\partial}{\partial x_j}\left[\left(\mu + \frac{\mu_t}{\sigma_\epsilon}\right)\frac{\partial \epsilon}{\partial x_j}\right] + \mathrm{C}_{\epsilon 1}\frac{\epsilon}{k}P_k - \mathrm{C}_{\epsilon 2}\rho\frac{\epsilon^2}{k} \tag{2.32}$$

where the production term P_k and turbulent viscosity μ_t are

$$P_k = -\rho\overline{u_i' u_j'}\frac{\partial \bar{u}_i}{\partial x_j} \tag{2.33}$$

$$\mu_t = C_\mu \frac{\rho k^2}{\epsilon} \tag{2.34}$$

The Reynolds stress tensor is defined by the following expression:

$$\rho\overline{u_i' u_j'} = \frac{2}{3}\rho k \delta_{ij} - 2\mu_t S_{ij} \tag{2.35}$$

The mean strain rate tensor S_{ij} has the same formulation as in Eq. (2.28). The empirical coefficients developed by Launder and Sharma [23] are displayed in Table 2.1.

Table 2.1 Standard *k*-ε Model Coefficients

σ_k	σ_ε	$C_{\varepsilon 1}$	$C_{\varepsilon 2}$	C_μ
1.0	1.22	1.44	1.92	0.09

2.4.2 Quadratic k-ε Model

As highlighted above, all NLEVMs are founded on the same basic stress-strain relationship, differing with respect to the formulation of model coefficients. The quadratic form of the NLEVM developed by Baglietto and Ninokata [37] was selected for implementation in Hydra-TH, as the model coefficients are formulated based on a more rigorous approach that separated the turbulence effects, which provide improved generality and robustness. This formulation respects the constraints of realizability, which mandate that the turbulent normal stresses must remain positive $\left(\overline{u_i' u_i'} \geq 0\right)$ and Schwarz' inequality must be satisfied between fluctuating quantities $\left(\overline{u_i' u_j'}\right)^2 \leq \overline{u_i'^2}\,\overline{u_j'^2}$. Satisfaction of these constraints leads to model coefficients that are not constant, but rather vary with the mean flow deformation rate.

The transport equations for *k* and ε share the same formulation as the standard model in Eqs. (2.31) and (2.32). Likewise, the turbulent viscosity μ_t also shares the same formulation as the standard model in Eq. (2.34). Lastly, the empirical coefficients σ_k, σ_ε, $C_{\varepsilon 1}$, and $C_{\varepsilon 2}$ share the same values as the standard model in Table 2.1.

The realizability of the model is enforced by the C_μ coefficient, which is no longer a constant as in the original formulation, but rather is expressed as a function of the mean shear invariant *S* and mean rotation invariant *Ω*:

$$C_\mu = \frac{C_{A0}}{C_{A1} + S * C_{A2} + \Omega * C_{A3}} \tag{2.36}$$

$$S = \frac{k}{\epsilon}\sqrt{2 S_{ij} S_{ij}} \tag{2.37}$$

$$\Omega = \frac{k}{\epsilon}\sqrt{2 \Omega_{ij} \Omega_{\mathrm{ij}}} \tag{2.38}$$

The Reynolds stress tensor is defined by the following expression:

$$\begin{aligned} \rho\overline{u_i' u_j'} &= \frac{2}{3}\rho k \delta_{ij} - 2\mu_t S_{ij} \\ &+ 4\mu_t \frac{k}{\epsilon}\left\{C_1\left[S_{ik}S_{kj} - \frac{1}{3}\delta_{ij}S_{kl}S_{kl}\right] + C_2\left[\Omega_{ik}S_{kj} + \Omega_{jk}S_{ki}\right] + C_3\left[\Omega_{ik}\Omega_{jk} - \frac{1}{3}\delta_{ij}\Omega_{kl}\Omega_{kl}\right]\right\} \end{aligned} \tag{2.39}$$

As can be seen, this equation is the first two lines of Eq. (2.30) as the cubic terms have been neglected. The first line of Eq. (2.39) represents the linear formulation of the Reynolds stresses that is adopted in isotropic linear eddy viscosity models such as the standard *k*-ε model. The second line denotes the quadratic stress terms that serve to provide a more complete description of the normal stress anisotropy. The coefficients C_1-C_3 are not model constants, but instead vary with the mean flow deformation rate:

$$C_1 = \frac{C_{NL1}}{(C_{NL4} + C_{NL5}S^3)C_\mu} \tag{2.40}$$

$$C_2 = \frac{C_{NL2}}{(C_{NL4}+C_{NL5}S^3)C_\mu} \tag{2.41}$$

$$C_3 = \frac{C_{NL3}}{(C_{NL4}+C_{NL5}S^3)C_\mu} \tag{2.42}$$

where the model coefficients C_{NL1}-C_{NL5} are summarized in Table 2.2.

Table 2.2 Quadratic *k*-ε Model Coefficients

C_{A0}	C_{A1}	C_{A2}	C_{A3}	C_{NL1}	C_{NL2}	C_{NL3}	C_{NL4}	C_{NL5}
0.667	3.9	1	0.0	0.8	11	4.5	1000	1.0

2.4.3 RNG k-ε Model

The Hydra-TH package selected the RNG *k*-ε model as a first "all-purpose" model, which was therefore implemented as the default option for two-equation RANS. Yakhot et al. [42] derived the RNG model based on Re-Normalization Group (RNG) methods. In this approach, RNG techniques are used to develop a theory for the larger turbulent scales in which the effects of the smaller scales are represented by modified transport coefficients. The overall structure of the transport equations remains the same as with the standard *k*-ε model, but with a modified definition and coefficient values. Most importantly, Yakhot et al. included an additional term in the ε transport equation, which is an ad hoc model not derived from RNG theory, but nonetheless plays a dominant role in extending the capabilities of the RNG closure in comparison to the standard *k*-ε approach.

The *k*-ε transport equations for the RNG model are defined as:

$$\frac{\partial}{\partial t}(\rho k) + \frac{\partial(\rho u_j k)}{\partial x_j} = \frac{\partial}{\partial x_j}\left[\left(\mu + \frac{\mu_t}{\sigma_k}\right)\frac{\partial k}{\partial x_j}\right] + P_k - \rho\epsilon \tag{2.43}$$

$$\frac{\partial}{\partial t}(\rho\epsilon) + \frac{\partial(\rho u_j \epsilon)}{\partial x_j} = \frac{\partial}{\partial x_j}\left[\left(\mu + \frac{\mu_t}{\sigma_\epsilon}\right)\frac{\partial \epsilon}{\partial x_j}\right] + \mathrm{C}_{\epsilon 1}\frac{\epsilon}{k}P_k - \left[\mathrm{C}_{\epsilon 2} + \frac{C_\mu \eta^3(\eta/\eta_0)}{1+\beta\eta^3}\right]\rho\frac{\epsilon^2}{k} \tag{2.44}$$

The production term P_k, turbulent viscosity μ_t, and Reynolds stresses are identical to the formulation of the standard model, as displayed in Eqs. (2.33)-(2.35). The term η signifies the mean shear invariant *S*, with the same prescription as in Eq. (2.37). The model coefficients are summarized in Table 2.3.

Table 2.3 RNG *k*-ε Model Coefficients

σ_k	σ_ε	$C_{\varepsilon 1}$	$C_{\varepsilon 2}$	C_μ	β	η_0
0.72	0.72	1.42	1.68	0.085	0.012	4.38

The last term on the right hand side in Eq. (2.44) is the additional ad hoc modification. This term is largely responsible for the differences in performance of the standard and RNG models. Here, the η term includes "some" effect of the mean flow distortion of the turbulence dissipation, and such capability leads to improved predictions on high strain rate and high streamline curvature flows. It should be noted from a rigorous point of view that the RNG model yields more realistic flow features by grossly overestimating the level of ε. In reality it is the production of *k* that is overestimated by the eddy viscosity assumption, and not the levels of ε, and therefore the RNG model often predicts the right trends for the wrong reason.

3 Model Implementation

The implementation of the standard and quadratic k-ε models into the Hydra-TH source code consisted of three phases: class structure redesign, standard model implementation, and quadratic model implementation. Each of these phases are explored herein.

3.1 Class Structure Redesign

As described in Section 2.4, the RNG, standard, and quadratic k-ε models have similar formulations for the k and ε transport equations, differing only with respect to model coefficients, source terms, and stress-strain constitutive relation. When programming the standard and quadratic k-ε models into Hydra-TH, it was desirable to do so in an efficient manner that grouped general functions intrinsic to all models together, yet kept the model-specific functions separate. This methodology led to the reconstruction of the class inheritance scheme for the k-ε model.

The original class inheritance scheme is depicted on the left side of Figure 3.1. As can be seen, the RNG k-ε class originally derived directly from the Turbulence class. The redesigned class architecture is illustrated on the right side of Figure 3.1. A "general" k-ε class has been crafted during this work, from which the specific formulations of the RNG, standard, and quadratic k-ε models now derive. This framework will allow for easy implementation of additional k-ε turbulence models, including the Realizable k-ε model by Shih [43] that will be implemented in future CASL milestones.

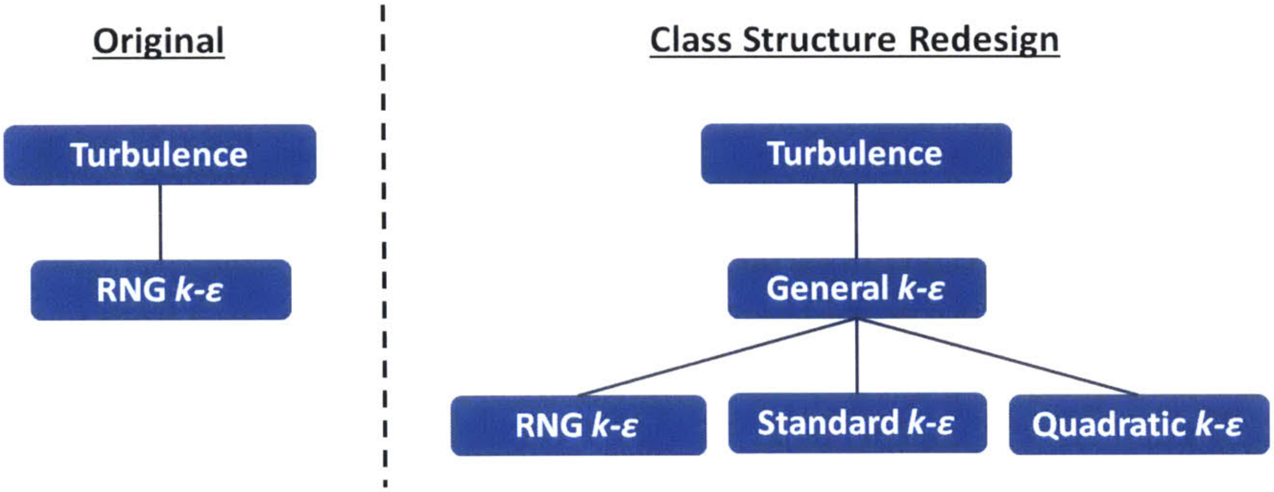

Figure 3.1 Redesign of k-ε class inheritance scheme

The "general" k-ε class comprises functions and operations inherent to all k-ε models, such as the allocation of boundary conditions and the formulation of the right- and left-hand sides of the k and ε transport equations. The RNG, Standard, and Quadratic classes pertain to the model-specific variants, which facilitate the calculation of model-dependent source terms and the Reynolds stress tensor.

During this phase, the original RNG class was deconstructed into its constituent functions so that it could be reassembled into the redesigned General and RNG class frameworks. This process is depicted in Figure 3.2, where the preceding notation (CCINS) signifies cell-centered incompressible Navier-Stokes.

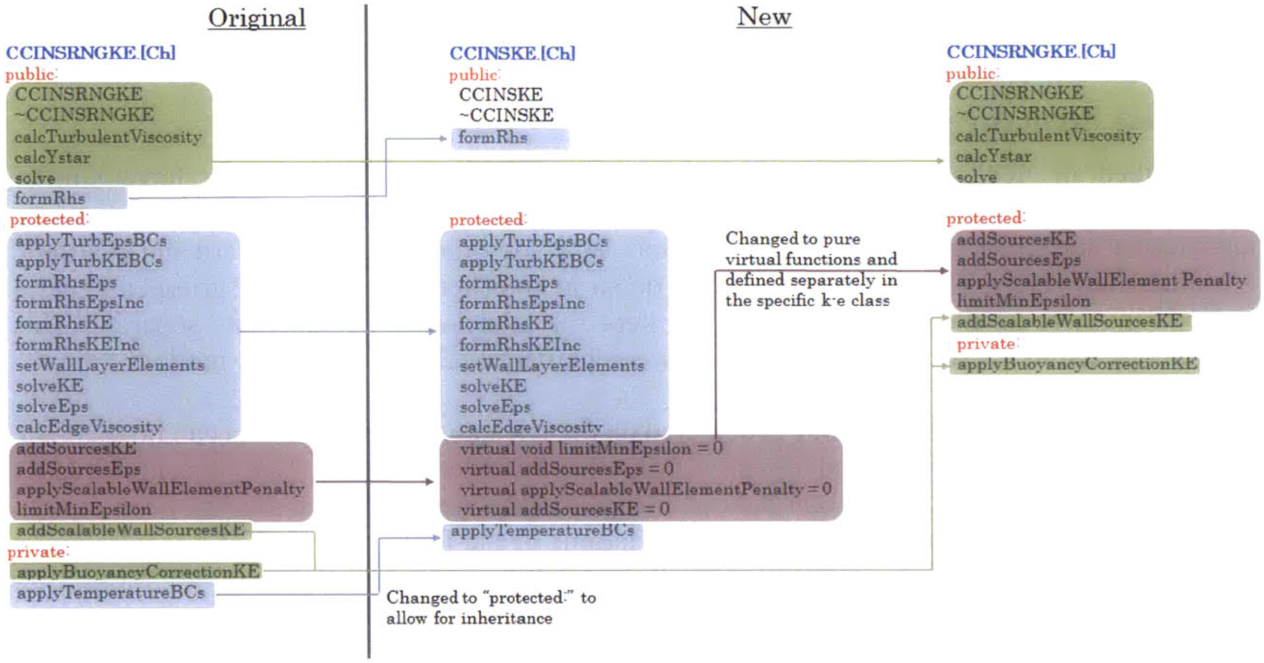

Figure 3.2 Reconstruction of the base and derived *k-ε* class structure

After the General and RNG *k-ε* class framework had been created, a series of regression, verification, and validation tests were performed for the RNG *k-ε* model to ensure that this reconstruction did not damage the performance of the RNG *k-ε* model. Upon successful completion of these tests, work progressed to the implementation of the standard model.

3.2 Standard *k-ε* Model Implementation

Implementation of the standard *k-ε* model was rather straightforward. This process consisted of first creating the file structure for the Standard class and then copying the contents of the RNG class into these file structures. Next, the functions inside the Standard class were modified to incorporate the standard *k-ε* model coefficients and source term formulation in the *ε* transport equation. Lastly, several simulations for the standard model were performed and compared to the results of the RNG model. The simulation results were quite comparable, which demonstrated confidence in the model's implementation.

3.3 Quadratic *k-ε* Model Implementation

The integration of the quadratic *k-ε* model into Hydra-TH was considerably more challenging than that of the standard model. The model implementation required the creation of new variable data structures and functions, an explicit treatment of the quadratic turbulent stress terms, and the selection of appropriate test cases for validation. Each of these aspects are illustrated in the following subsections.

3.3.1 Creation of New Variables and Functions

As discussed in Section 2.4.2, the quadratic model adopts a quadratic formulation for the stress-strain constitutive relation. To facilitate the tensor algebra mathematical operations that are described in Eq. (2.39), a series of functions for tensor algebra operations were first created to perform the requisite calculations. The mean strain rate S_{ij} and mean rotation rate Ω_{ij} tensors are symmetric and antisymmetric tensors, whose general properties are demonstrated below:

$$S_{ij} = \begin{bmatrix} S_{11} & S_{12} & S_{13} \\ S_{12} & S_{22} & S_{23} \\ S_{13} & S_{23} & S_{33} \end{bmatrix} \tag{3.1}$$

$$\Omega_{ij} = \begin{bmatrix} 0 & \Omega_{12} & \Omega_{13} \\ -\Omega_{12} & 0 & \Omega_{23} \\ -\Omega_{13} & -\Omega_{23} & 0 \end{bmatrix} \tag{3.2}$$

As can be seen, a symmetric stress tensor consists of six unique values, whereas an antisymmetric tensor consists of only three. Therefore, to save on computational cost and memory requirements, the data structures for the symmetric and antisymmetric tensors are stored in the compressed format displayed in Figure 3.3.

```
struct SymTensor {
   Real XX;
   Real YY;
   Real ZZ;
   Real XY;
   Real YZ;
   Real ZX;
}
```

```
struct AntiTensor {
   Real XY;
   Real YZ;
   Real ZX;
}
```

Figure 3.3 Symmetric and antisymmetric data structures

It was therefore necessary to develop the tensor algebra functions in a manner that was consistent with these data structures. After these prerequisite tensor algebra functions had been implemented, tested, and verified, it was then possible to begin developing the quadratic model.

The quadratic model also makes use of a model coefficient C_μ that is no longer constant, but rather varies with the mean deformation flow rate as described in Eq. (2.36). Further, the calculation of the production term P_k is considerably more intricate than that of the standard model (Eqs. (2.33) and (2.39)). It was therefore desirable to develop two new variables inside Hydra-TH to store these cell-centered values: namely, CMU and PK. Additionally, two new functions to facilitate their calculation were also constructed: *calcElemCMU* and *calcReynoldStress*. The resulting production term PK would then plug into the same source term as in the Standard and RNG models. The general structure of both of these functions are expressed in pseudocode form in Figure 3.4 and Figure 3.5. While some of the steps are excluded from these figures—such as tensor transpose and inner product operations—the general methodology of breaking the terms up into its components and adding them together is readily demonstrated.

```
void calcElemCMU() {
.
.
.
// Looping through all global element ID's (gid) between cells and edges

        // Create Symmetric and Antisymmetric tensors
        // Calculate double inner product of tensors
        Calculate $S_{ij}S_{ij}$
        Calculate $\Omega_{ij}\Omega_{ij}$
        // Create Symmetric and Antisymmetric tensors
        Calculate S                 [Eq. (2.37)]
        Calculate $\Omega$                 [Eq. (2.38)]
        // Calculate and assign the nonlinear Cmu for each element
        Calculate $C_\mu$[gid]          [Eq. (2.36)]
}
```

Figure 3.4 Pseudocode for *calcElemCMU* function

```
void calcReynoldStress() {
.
.
.
// Initialize Variables
// Creation of nested for loop structure between cells

        // COMPUTE LINEAR STRAIN
        Calculate Lin       Eq. (2.39)-row 1

        // COMPUTE QUADRATIC STRAIN
        // Calculate Coefficients
        Calculate $C_1$        Eq. (2.40)
        Calculate $C_2$        Eq. (2.41)
        Calculate $C_3$        Eq. (2.42)

        // Compute First Term
        Eq. (2.39)-row 2
        -   A: Calculate $S_{ik}S_{kj}$
        -   B: Calculate $-\frac{1}{3}\delta_{ij}S_{kl}S_{kl}$
        -   Q1: Add A and B, multiply by $C_1$

        // Compute Second Term
        Eq. (2.39)-row 2
        -   A: Calculate $\Omega_{ik}S_{kj}$
        -   B: Calculate $\Omega_{jk}S_{ki}$
        -   Q2: Add A and B, multiply by $C_2$
        // Compute Third Term
        Eq. (2.39)-row 2
        -   A: Calculate $\Omega_{ik}\Omega_{jk}$
        -   B: Calculate $-\frac{1}{3}\delta_{ij}\Omega_{kl}\Omega_{kl}$
        -   Q3: Add A and B, multiply by $C_3$
        // Combine Quadratic Terms
        -   $T_{ij}$: Add Q1, Q2, Q3
        -   I: calculate $T_{ij}\frac{\partial \bar{u}_i}{\partial x_j}$        Eq. (2.33)
        -   Quad: $I * 4\frac{k}{\epsilon}\mu_t$

        // Update Production term
        PK[gid] = Lin - Quad
}
```

Figure 3.5 Pseudocode for calcReynoldStress function

3.3.2 Momentum Equation Treatment

For finite volume methods, it is common practice to solve the Navier-Stokes equations in integral form. The integral form of the RANS-averaged momentum equation defined in Eq. (2.16) is written in vector form as:

$$\rho\frac{\mathrm{d}}{\mathrm{dt}}\int_{\Omega^e}\bar{\boldsymbol{u}}\,d\Omega^e+\oint_{\Gamma^e}\rho\bar{\boldsymbol{u}}(\bar{\boldsymbol{u}}\cdot\boldsymbol{n})d\Gamma^e-\oint_{\Gamma^e}\boldsymbol{\tau}\cdot\boldsymbol{n}\,d\Gamma^e+\int_{\Omega^e}\nabla\bar{p}\,d\Omega^e-\int_{\Omega^e}\mathbf{f}\,d\Omega^e=0 \tag{3.3}$$

Here, $\bar{\boldsymbol{u}}$ is mean velocity vector, $\boldsymbol{n}$ is the normal direction, $\bar{p}$ is the mean pressure, $\boldsymbol{f}$ is the vector of all body forces, and $\boldsymbol{\tau}$ denotes both the regular and turbulent stresses. The terms Ω and Γ denote volume and surface integrals, respectively, with the superscript e signifying that the integrals are edge-based. Before proceeding, let us first define the following mass, advective, viscous, gradient, and body-force operators:

$$\mathrm{M}^{\mathrm{e}}=\rho\Omega^{\mathrm{e}} \tag{3.4}$$

$$\mathrm{A}^{\mathrm{e}}(\rho,\bar{\boldsymbol{u}})\bar{\boldsymbol{u}}=\oint_{\Gamma^e}\rho\bar{\boldsymbol{u}}(\bar{\boldsymbol{u}}\cdot\boldsymbol{n})d\Gamma^e \tag{3.5}$$

$$K^{\mathrm{e}}\bar{\boldsymbol{u}}=\oint_{\Gamma^e}\boldsymbol{\tau}\cdot\boldsymbol{n}\,d\Gamma^e \tag{3.6}$$

$$\boldsymbol{B}^{\mathrm{e}}\bar{p}\Omega^e=\int_{\Omega^e}\nabla\bar{p}\,d\Omega^e \tag{3.7}$$

$$\boldsymbol{F}^{\mathrm{e}}=\int_{\Omega^e}\mathbf{f}\,d\Omega^e \tag{3.8}$$

After substituting Eq. (3.4)-(3.8) into Eq. (3.3), and then applying both forward- and backward-Euler time discretization, the momentum equation reduces to the following form:

$$\begin{aligned}\mathrm{M}\frac{\bar{\boldsymbol{u}}^{n+1}-\bar{\boldsymbol{u}}^{n}}{\Delta t}&=(1-\theta)K\bar{\boldsymbol{u}}^{n}+\theta K\bar{\boldsymbol{u}}^{n+1}+(1-\theta)\mathbf{F}^{\mathrm{n}}+\theta\boldsymbol{F}^{n+1}-(1-\theta)A(\rho,\bar{\boldsymbol{u}})\bar{\boldsymbol{u}}^{n}\\&\quad-\theta A(\rho,\bar{\boldsymbol{u}})\bar{\boldsymbol{u}}^{n+1}-\boldsymbol{B}\bar{p}^{n}-\theta\boldsymbol{B}(\bar{p}^{n+1}-\bar{p}^{n})\end{aligned} \tag{3.9}$$

Here, $0\leq\theta\leq1$, where $\theta=0$ corresponds to a forward-Euler scheme, $\theta=1$ a fully-implicit treatment, and $\theta=½$ a Crank-Nicholson scheme. The user is able to specify the value of θ for each term: that is, θ_A, θ_F, and θ_K. However, it is best practice to set all θ values equal to 1 so that a fully-implicit time marching scheme can be utilized in order to facilitate large time-steps.

An implicit treatment of the quadratic terms displayed in Eq. (2.39) was not feasible due to the complexity of the terms. Consequently, these quadratic terms were treated fully explicitly. The auxiliary functions *calcAuxTurbRhs* and *calcQuadStress* were developed to accommodate this process. The function *calcAuxTurbRhs* constructed the edge-based value for the turbulent quadratic stress, which consisted of interpolating cell-centered values to the edges. This function then called *calcQuadStress* in order to calculate the edge-based stresses. The quadratic stresses were then added to the right hand side.

3.3.3 Model Implementation Assessment

The implementation of the model was assessed through simulation of two experimental test cases for fuel rod arrays. These were the triangular rod array experiments of Mantlik et al. [19] and the square rod array experiments of Hooper and Wood [20]. The selection of both these test cases was important, as the presence of secondary flows due to the complex geometry was prominent. Turbulence driven secondary flows redistributed pertinent flow properties, including the velocity and wall shear stress profiles. Model assessment therefore consisted of a comparison between the standard and quadratic k-ε models. Important metrics of comparison for the quadratic model included the prediction of the magnitude and direction of these secondary flows, in addition to better resolution of the axial velocity and wall shear stress profiles. The model assessment of the Mantlik et al. [19] and Hooper and Wood [20] experimental test cases is thoroughly examined in Section 5.

3.4 Bookkeeping with the Coding

The standard and quadratic models needed to be integrated into the remainder of the code framework in order to ensure proper calculation and activation of the models. This consisted of modifying numerous files as outlined below as well as developing the appropriate parsing structure for user activation.

3.4.1 Modification of Files

Numerous other files in the code make calls to the activated turbulence model for calculation of important field quantities such as turbulent viscosity, wall normal distance, and $y+$. These calculations rely on the model-specific coefficients and equations. Managing these instances was typically handled through the prescription of *if* and/or *switch* statements for the requisite k-ε model. Further, functions to facilitate plotting of important field quantities such as CMU and PK needed to be developed so that the data could be exported and post-processed. Examples of this usage include the following, where the terms on the left and right side of the double-colon signify the class and function, respectively:

- CCINSEnergy::calcElemConductivityWallFunctionKEps
- CCINSFlow::calcWallShear
- CCINSFlow::getTurbPrandtl
- CCINSFlow::formAllRhs
- CCINSFlow::formTurbulenceTransportRhs
- CCINSFlow::applySimpleICs
- CCINSFlow::initTransportSolvers
- CCINSFlow::writeElemYstarField
- CCINSFlow::writeElemCMUField
- CCINSFlow::writeElemPKField

3.4.2 Parsing Structures

The relevant files dedicated to parsing the input control file needed to be updated to allow activation of the desired k-ε turbulence model. Within the turbulence specification parsing block, the user need only specify "rng_ke", "std_ke", or "nl_ke" for activation of the RNG, standard or quadratic models. The following functions inside the file *CCIncNavierStokesParse.C* needed to be modified and created in order to establish this parsing framework:

- parseCCINSTMODEL
- parseCCINSTURB
- parseRNGKEOpt
- parseSTDKEOpt
- parseNLKEOpt

4 Quadratic Model Assessment of 'Classic' Engineering Test Cases

The quadratic model has been applied to 'classic' engineering test cases designed to test the strength of the model for complex engineering problems as part of the validation process. These include the prediction of turbulence driven secondary flows that arise in a square duct and the resolution of the streamline curvature effects in a U-channel bend. Each of these test cases are explored in the subsequent pages of text. A brief description of the experimental apparatus, computational setup, and simulation results are performed for all test cases whereby the performance of the quadratic, standard, and RNG *k-ε* models are examined. Appendices A and B contain the Hydra-TH control files and experimental data considered in this study, respectively.

At the conclusion of each test case, a grid refinement study is also performed in order to demonstrate the convergence of the simulation results. Richardson extrapolation [44] [45] was attempted to estimate the error on the finest grid. The order of accuracy p can be quantified by using the following equation:

$$p = \frac{\ln\left(\frac{\phi_{2h}-\phi_{4h}}{\phi_h-\phi_{2h}}\right)}{\ln r} \tag{4.1}$$

Here, r is the factor by which the grid density is increased (for example, r equals 2 signifies that the spacing between grids is halved); φ is a field quantity that is used as a metric for comparison (e.g. centerline velocity); and h denotes the mesh refinement—the coarsest mesh has subscript $4h$, and the finest mesh has subscript h. The error on the finest grid h is estimated by application of the following expression:

$$\epsilon_h \approx \frac{\phi_h-\phi_{2h}}{r^p} \tag{4.2}$$

Note that while a Richardson extrapolation has been attempted, the difference between the various grid refinements is minimal and the order of convergence is masked by the nonlinearities in the solution methods. While the order of convergence is reported for the following test cases, it does not have any proper meaning. Consequently, the difference between the grids is therefore the best estimator of the error.

4.1 Square Duct

A square duct, although simple in its design, in fact leads to the creation of complex turbulent structures. These structures give rise to secondary flows that serve to redistribute the flow profile. The quadratic terms—which resolve the turbulent normal stress anisotropy—are sufficient to resolve these secondary flows as well as their redistribution of the flow profile.

4.1.1 Experimental Setup

An extensive compendium of the flow distribution in a square duct with 5" sides was compiled by Hoagland [46] as part of his Ph.D. thesis earned at MIT. A duct with a length of 32 feet (L/D_e = 77) was used to ensure the development of fully developed flow. Pitot tubes were used to record the velocity measurements in the bulk of the flow, whereas hot wire probes were used to record the measurements near the duct walls. The Reynolds number considered in this study is 66,000.

4.1.2 ***Computational Setup***

The inherent symmetry of the problem was exploited in order to simulate a quarter section of the duct, as demonstrated in Figure 4.1. A length of 11.5 m was modeled in order to ensure that a fully developed flow was achieved. This was necessary because Hydra-TH currently does not support the capability for periodic flow boundary conditions. In order to achieve a Reynolds number equal to 66,000, the values listed in Table 4.1 were imposed in the Hydra-TH control file that is displayed in Appendix A.1.

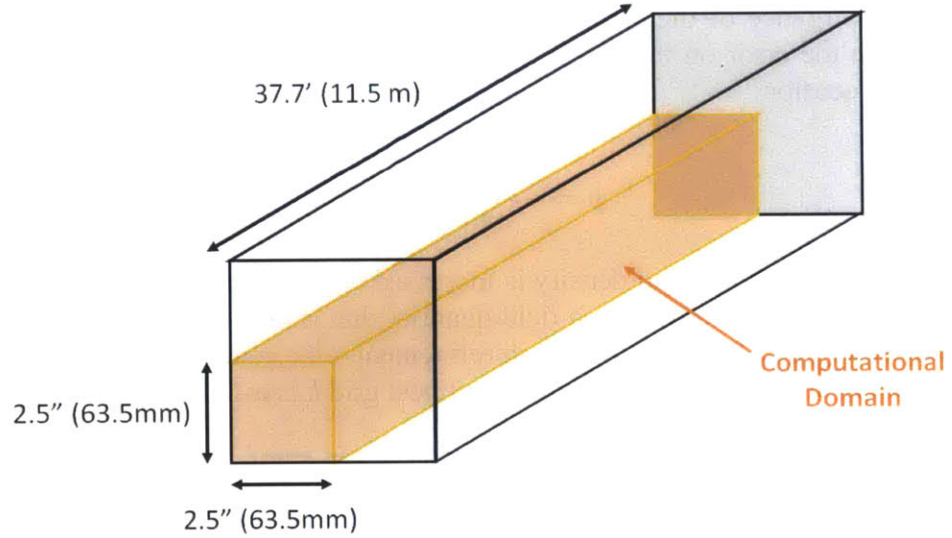

Figure 4.1 Square duct computational domain

Table 4.1 Flow parameters specified for square duct simulation

ρ [kg/m³]	*μ [kg/m/s]*	*V_b [m/s]*	*D [m]*	*Re*
1	$1\text{x}10^{-5}$	5.1969	0.127	66,000

The boundary conditions specified for the problem are displayed in Figure 4.2. A velocity of 5.196 m/s was specified at the inlet (sideset 1) and a zero reference pressure boundary was set at the outlet (sideset 2).Wall boundary conditions (no-slip) were specified for the left (sideset 3) and bottom (sideset 6) walls of the duct. Symmetry velocity boundary conditions were established for sidesets 4 and 5 by setting the velocity component normal to the surface equal to zero.

Three grids of increasing refinement were used for this study. Refinement in the axial direction (z) was fixed constant at 100 elements, while the cross-sectional spacing was refined by a factor of 2. Two wall layer elements, each of 3.175 mm thickness, were used for all mesh sizes. This ensured the correct behavior of the wall treatment, which is based on a two-layer scalable wall-function approach. The cross-sectional view of all three mesh sizes is illustrated in Figure 4.3 and the mesh sizes are listed in Table 4.2. A grid refinement study has been performed, but is deferred until later in this section.

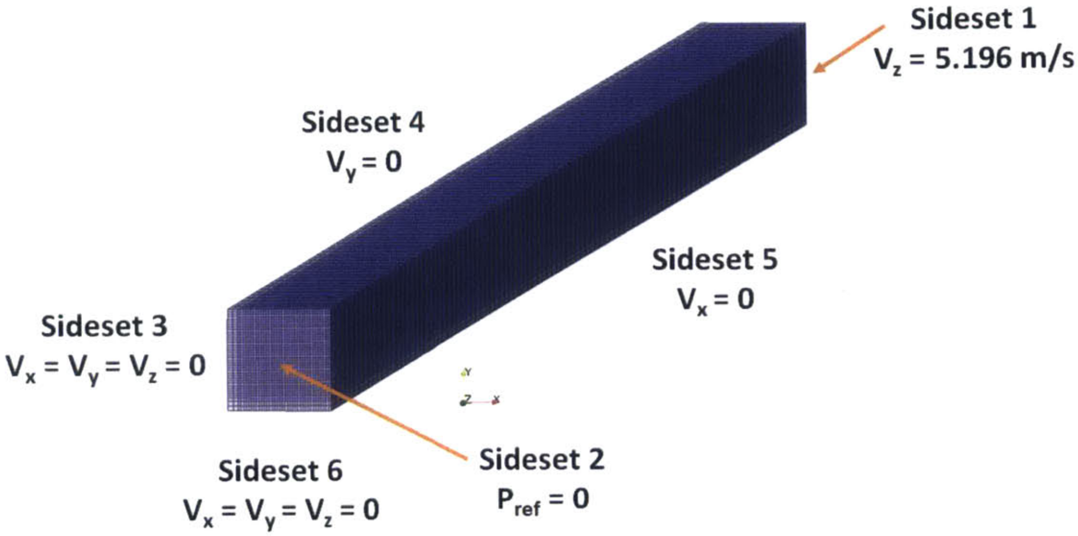

Figure 4.2 Boundary conditions for square duct simulations

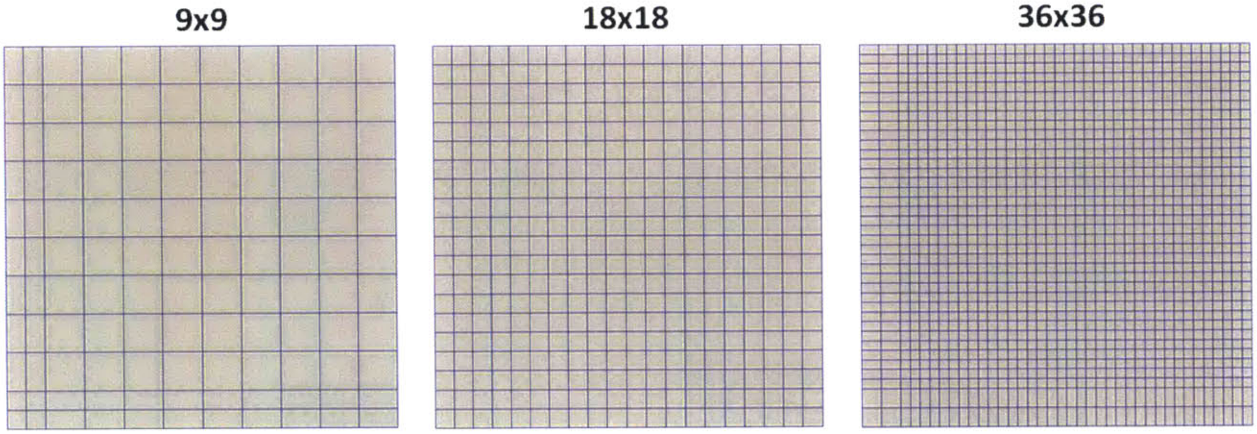

Figure 4.3 Mesh refinements examined for square duct simulations

Table 4.2 Mesh refinements examined for square duct simulation

Wall Elements	*x*	*y*	*z*	*Total Elements*
2	9	9	100	12,100
2	18	18	100	40,000
2	36	36	100	144,400

4.1.3 ***Results***

Here, the simulation results for the most refined mesh (36x36) are presented and compared with the Hoagland [46] experimental data. The axial velocity profiles for 6 different *y*/*a* slices are compared for the quadratic, standard, and RNG *k*-*ε* models. The data slices were constructed by fixing the position *x*, and measuring the velocity profile as a function of *y*. All 6 slices are presented in Figure 4.4, whereas Figure 4.5 overlays the predictions from the three *k*-*ε* models atop a selected single *x*/*a* profile. As can be seen in Figure 4.5, the standard and RNG models behave near identically for all six slices, as they underpredict the axial velocity profile in the near wall region and overpredict it in the bulk of the flow. The quadratic model performs noticeably better, as it yields predictions closer to the experimental values for both the near wall and bulk flow regions. The quadratic model does yield a noticeably lower prediction in the near wall region for the *x*/*a* =0.1 slice. This is most likely attributable to the wall layer elements that arise and overlap in the corner of the duct in this region.

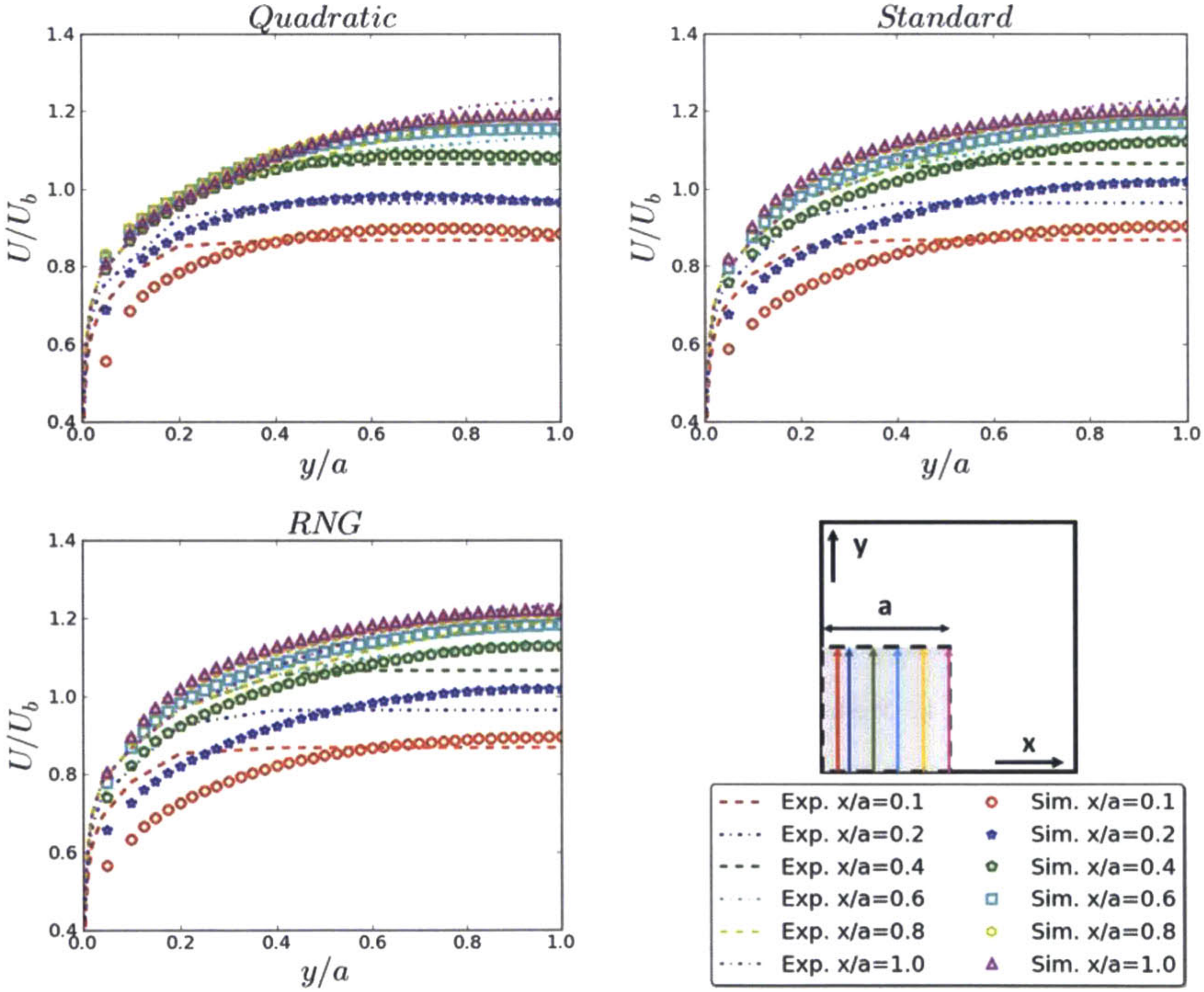

Figure 4.4 Square duct simulation predictions vs. experimental results

The secondary flow profiles at the plane of measurement are illustrated in Figure 4.6. As can be seen, the quadratic model accurately predicts the formation of two vortices. Conversely, the standard and RNG models do not capture this phenomena, and rather predict secondary flows that accelerate to the center of the duct. Further, the magnitude of the secondary flows is on the order of 0.1% of the axial velocity for the quadratic model; in contrast, it is on the order of 0.0001% for the standard and RNG models and is most likely spurious velocities produced as a consequence of the linear eddy viscosity model. The ability of the quadratic model to resolve these secondary flows is important as they allow it to capture the turbulence redistribution of the axial velocity profile, which leads to the better predictions for the quadratic model presented in Figure 4.5.

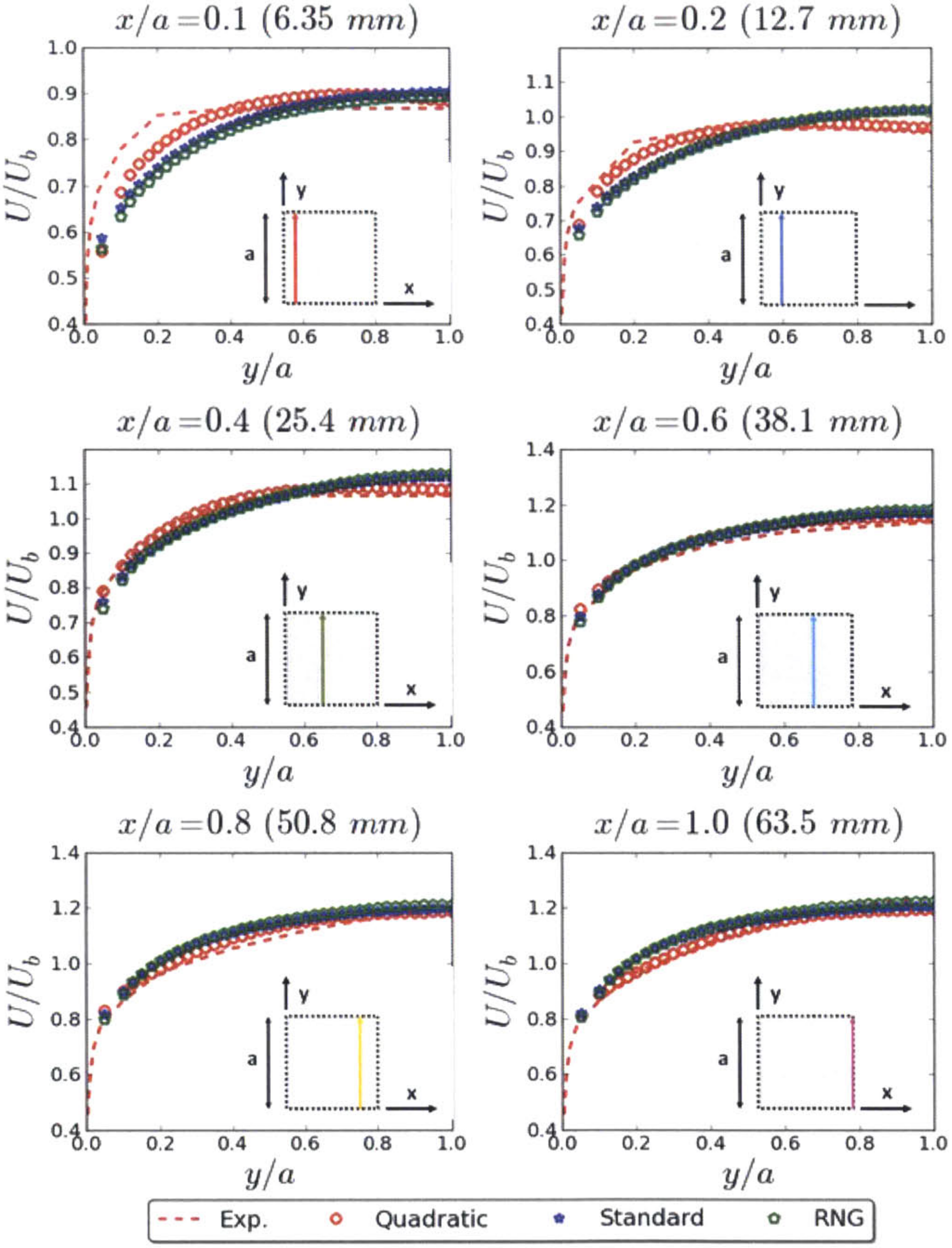

Figure 4.5 Comparison of *k*-ε model performance for square duct

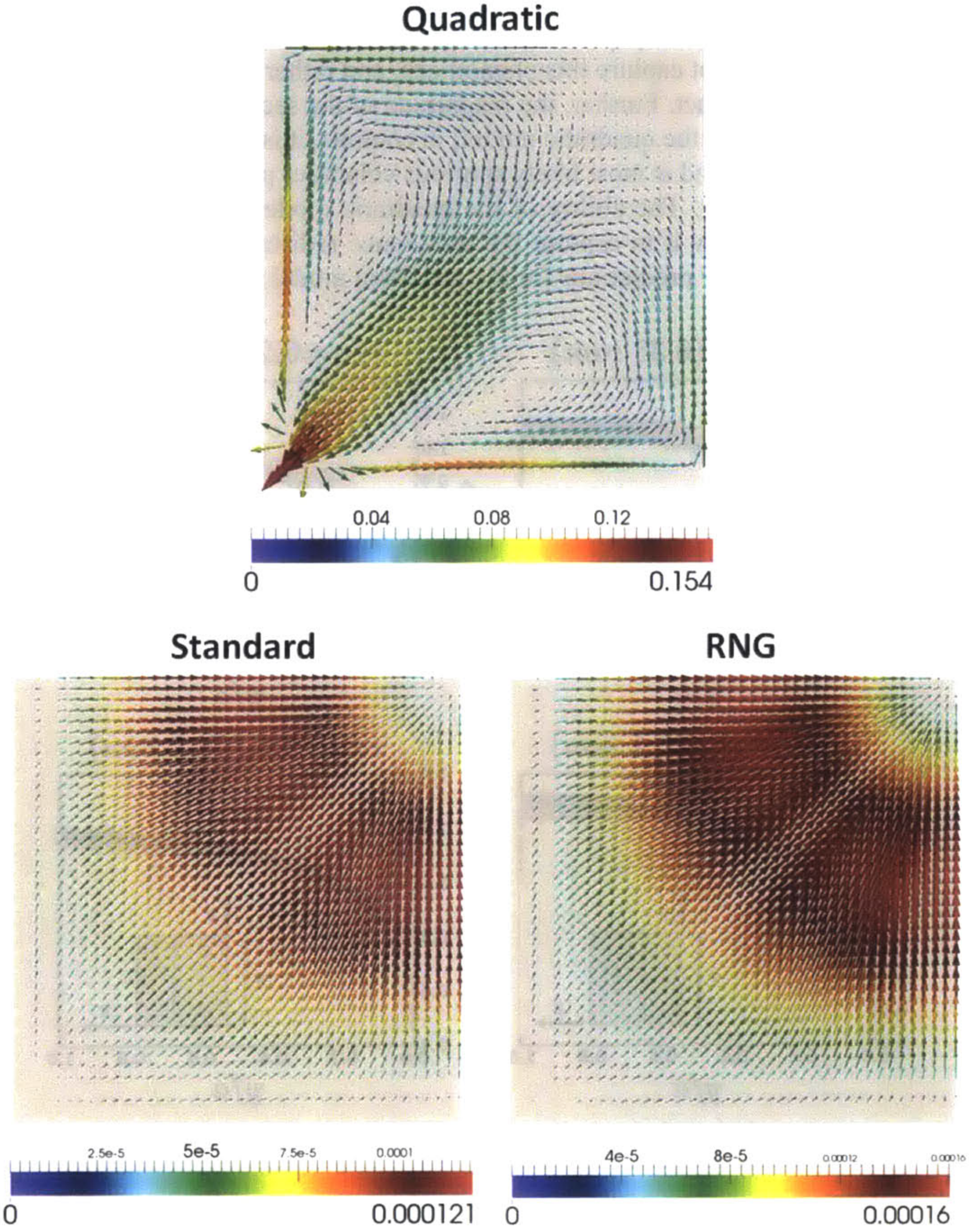

Figure 4.6 Secondary flow magnitudes [m/s] for square duct simulations at x/D_e = 77

4.1.4 *Grid Refinement Study*

The axial velocity profiles at $x/a = 1$ are plotted in Figure 4.7 for each model to demonstrate the convergence of the mesh to the axial velocity profiles. As can be seen, the axial velocity profiles are overlaid upon one another for all three refinements, which suggests that a converged result has been achieved. A Richardson extrapolation of the centerline velocity at the plane of measurement was performed for all three models, and the order of convergence and error on the finest grid are listed in Table 4.3.

The results of the Richardson extrapolation reveal surprising results. One would expect there to be an order of accuracy near two that would reflect the grid refinement ratio. While this is almost observed for the RNG case, the standard and quadratic cases demonstrate significantly lower orders of accuracy. This apparent discrepancy can be resolved by considering the centerline velocities for all three grid refinements that are also listed in Table 4.3. As can be seen, the centerline velocities for all three grid refinements are very close in magnitude. This suggests that grid refinement for the simplistic geometry of a square duct has negligible impact on the simulation results as both the coarse and fine meshes perform near identically.

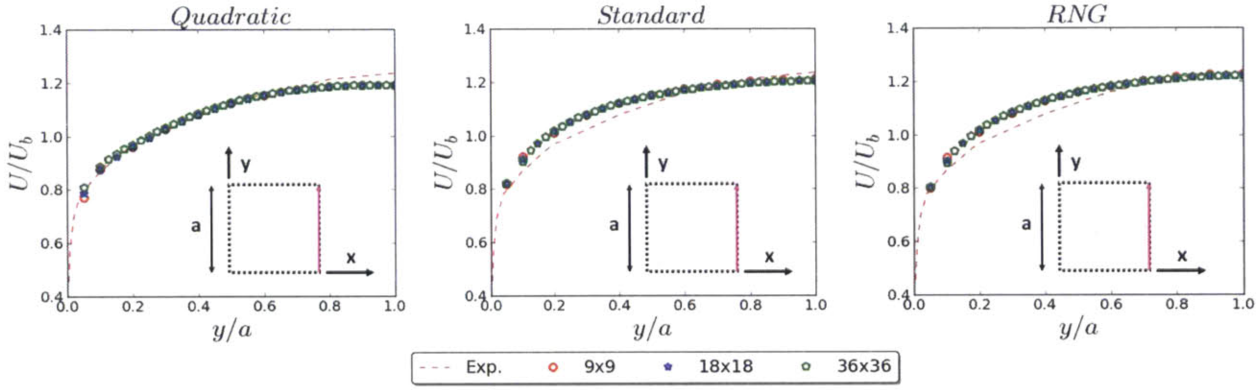

Figure 4.7 Grid convergence study for square duct test case

Table 4.3 Square duct Richardson extrapolation results

	Quadratic	***Standard***	***RNG***
V_{CL}/V_b: h	1.1929	1.2051	1.2221
V_{CL}/V_b: 2h	1.1916	1.2085	1.2255
V_{CL}/V_b: 4h	1.1928	1.2111	1.2264
Max Spread [Absolute]	0.00127	0.00598	0.00435
Order of Accuracy	0.0671	0.364	1.816
Error on Finest Grid [%]	2.67	1.17	0.13

4.2 U-Channel

A two-dimensional U-channel duct that has a 180° bend has been simulated to assess the ability of the k-ε models to capture the effects of streamline curvature and rotation. Recall that the cubic terms of NLEVMs account for streamline curvature and rotation; it is therefore expected that the quadratic model should not be able to fully reproduce the complex flow phenomena in the bend.

The U-channel was investigated experimentally and numerically by Monson et al. [47], and also numerically by Shur et al. [48]. The test case has also recently been simulated with special attention given to the curvature correction features of the Spalart-Allmaras turbulence model in Hydra-TH as part of a CASL milestone report by Smith and Christon [49].

4.2.1 Experimental Setup

The experiment by Monson et al. [47] was performed at the NASA Ames High Reynolds Number Channel I facility, which was an air blowdown wind tunnel. The channel was rectangular with an aspect ratio of 10. The velocity measurements were recorded using two-component laser Doppler velocimetry and the static pressures were measured using an electronically-scanned pressure system. The Reynolds number considered in this study is 1,000,000.

4.2.2 Computational Setup

The computational domain is displayed in Figure 4.8 and the flow parameters utilized to enforce a Reynolds number of 1,000,000 are presented in Table 4.4. Flow enters at the lower left boundary and exits at the upper right. The bend is a half circle with an inner and outer radius of 0.5 and 1.5 m, respectively. The arc length s normalized by the channel height H (s/H) is used as a metric for comparing the pressure coefficients for both the inner and outer walls later in this section. The inlet corresponds to $s/H = -10$, the beginning of the bend is at $s/H = 0$, the bend ends at $s/H = \pi$, and the outlet is at $s/H = 12 + \pi$. The primary velocity component at several angles in the bend will also be plotted as a function of the normal distance y from the inner wall. At the inner wall, $y/H = 0$, and at the outer wall $y/H = 1$.

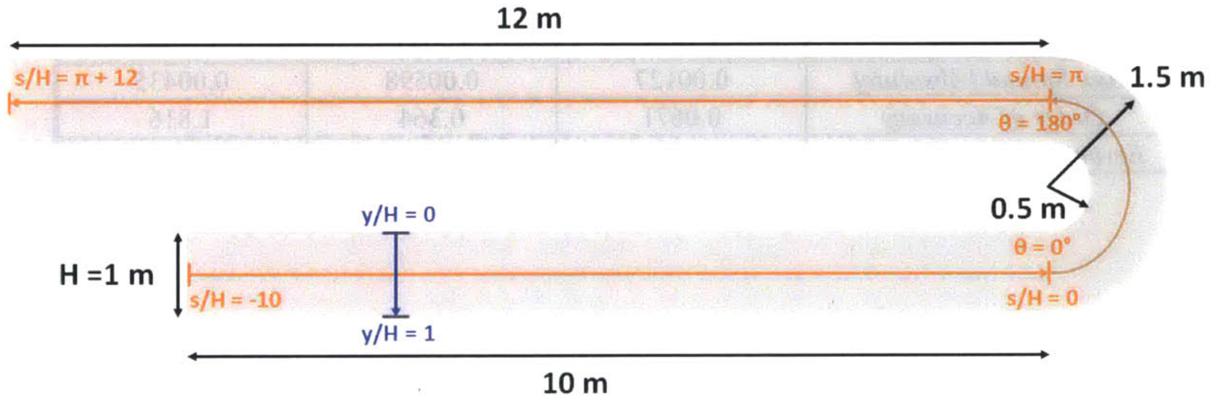

Figure 4.8 U-Channel computational domain

Table 4.4 U-channel simulation flow parameters

ρ [kg/m³]	*μ [kg/m/s]*	*V_b [m/s]*	*H [m]*	*Re*
1	$1\text{x}10^{-6}$	1.0	1	1,000,000

Three meshes of increasing refinement were generated using the Sandia mesh generator CUBIT. A picture of the coarsest mesh is displayed in Figure 4.9 and the mesh refinements examined are listed in Table 4.5. A biasing growth scheme in the primary flow direction was used for the top and bottom ducts; the number of elements in the primary flow direction is referred to as N_x. A dual-biasing growth scheme in the cross-flow direction was used. The number of grids in the cross-flow direction N_y was fixed at 111 for all three refinements, which corresponded to a $y+$ in the range of 20-30. A uniform interval spacing in the primary flow direction in the azimuthal bend was adopted, which is denoted as N_{az}. Only one element was modeled in the *z*-direction, as it was a 2-D simulation.

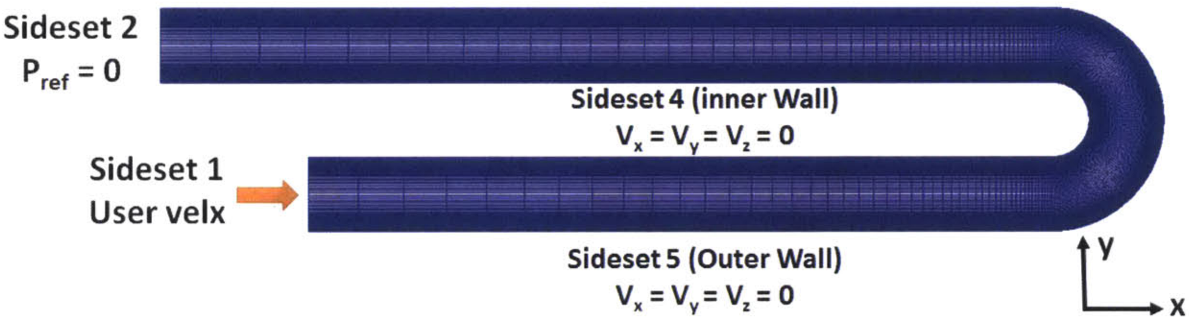

Figure 4.9 Boundary conditions for U-channel simulations

Table 4.5 Mesh refinement for U-channel

Top Duct		*Bottom Duct*		*Cross-flow*		*Bend*	*Total Elements*
N_x	*Growth Factor*	*N_x*	*Growth Factor*	*N_y*	*Dual-Growth Factor*	*N_{az}*	
56	1.058	48	1.067	111	1.05	100	22,644
112	1.03	96	1.04	111	1.05	200	45,288
224	1.015	192	1.02	111	1.05	400	90,576

The boundary conditions used for the mesh are also illustrated in Figure 4.9. A pressure boundary condition was set at the outlet (sideset 2). Wall boundary conditions were specified for the inner (sideset 4) and outer (sideset 5) duct walls. To enforce a 2-D solution, the *z*-component of velocity was set to zero for both the front and back surfaces (sideset 3). A fully developed turbulent flow was enforced at the inlet (sideset 1) through application of a user-defined velocity boundary condition in the file "*CCINSVelBC.C*" that uses the following 1/7th power law:

$$U(y) = U_{in}\left[1 - 2\frac{|y-y_c|}{H}\right]^{1/7} \tag{4.3}$$

Here, $U_{in} = 1/0.875$, y is the position, y_c is the value at the center of the channel, and H is the total height of the duct.

4.2.3 ***Results***

The results for the finest mesh are presented in this section. The primary flow predictions for the quadratic, standard and RNG models are compared with the experimental measurements for the various angles in the channel curve in Figure 4.10. As can be seen, all three models behave near identically and match the experimental trends at $\theta = 0°$. At $\theta = 90°$, the quadratic and RNG models behave similarly, with the standard model yielding an underprediction near the inner wall. At $\theta = 180°$, there are noticeable differences between all three models. The standard model yields a near flat distribution. The quadratic and RNG models perform similarly near the outer wall, but they begin to diverge when approaching the inner wall, with the RNG model giving slightly better agreement with the experimental values. The differences between all three models is even more pronounced at $s/H = 2 + \pi$. All three models fail to resolve the velocity profile in the outer wall region; interestingly, the RNG model does a better job at capturing the trends near the inner wall.

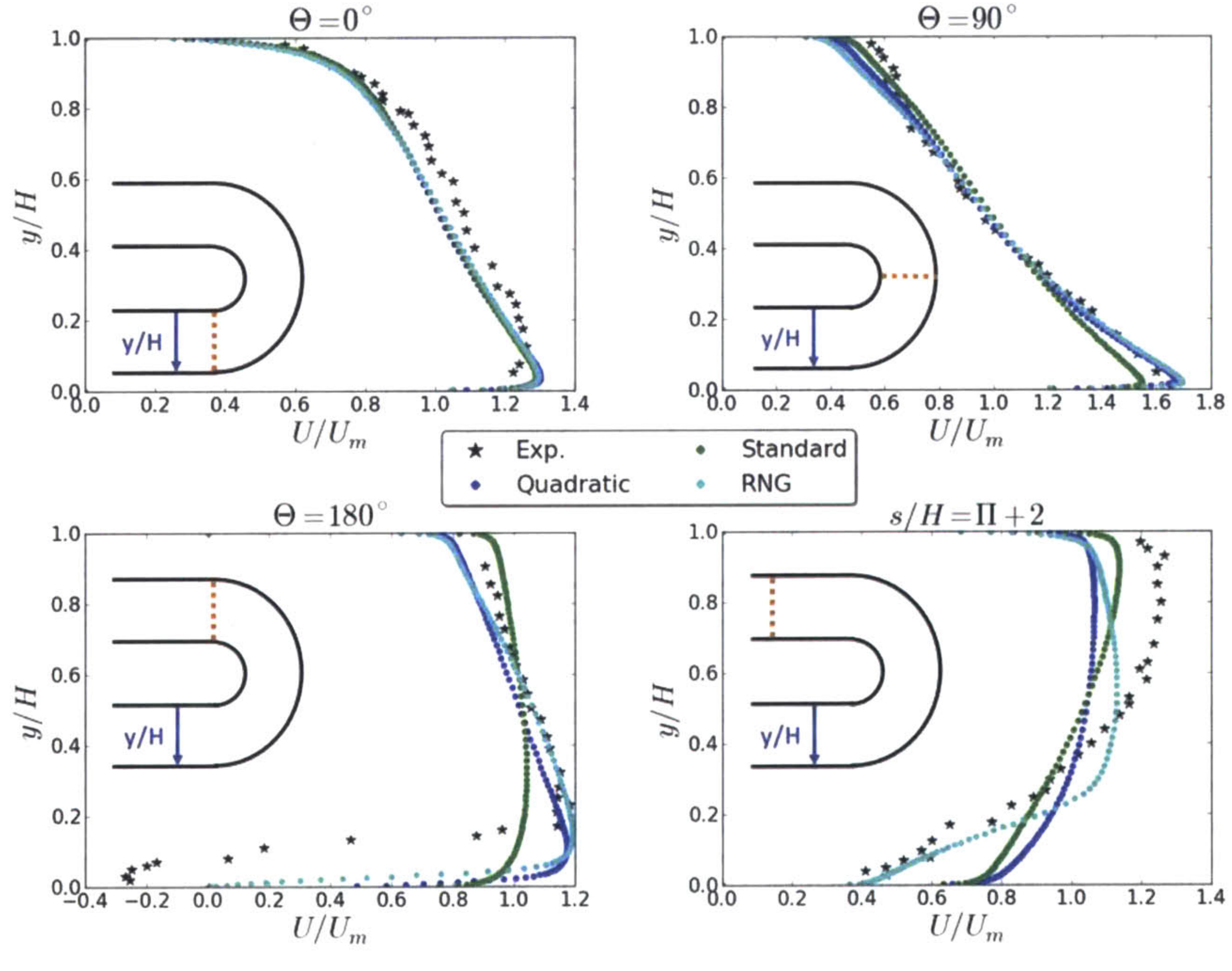

Figure 4.10 U-channel mean velocity profiles

The pressure coefficient as a function of arc length (*s*/*H*) is plotted for both the inner and outer walls in Figure 4.11, and is calculated by the following expression:

$$C_p = \frac{(P-P_{ref})}{\frac{1}{2}\rho V_b^2} = 2(P - P_{ref}) \tag{4.4}$$

Here, P is the pressure at the wall, with the reference pressure P_{ref} being taken at $s/H = -5$. As can be seen in Figure 4.11 for the inner wall, all three models behave near identically before the bend is encountered at $s/H = 0$. After the pipe bend begins, all three models overpredict the magnitude of the pressure coefficient, with the standard model giving a closer prediction in the duct after the bend. Interestingly, the RNG and quadratic models behave near identically for the whole span.

For the outer wall, again, all three models behave identically before going into the pipe bend, and give similar and better predictions for the pressure coefficient inside the pipe bend. After the pipe bend, however, all three models diverge from the experimental results, with the standard model being closer to the experimental values. The RNG model exhibits a small dip after the bend, and then its solution merges with the quadratic result.

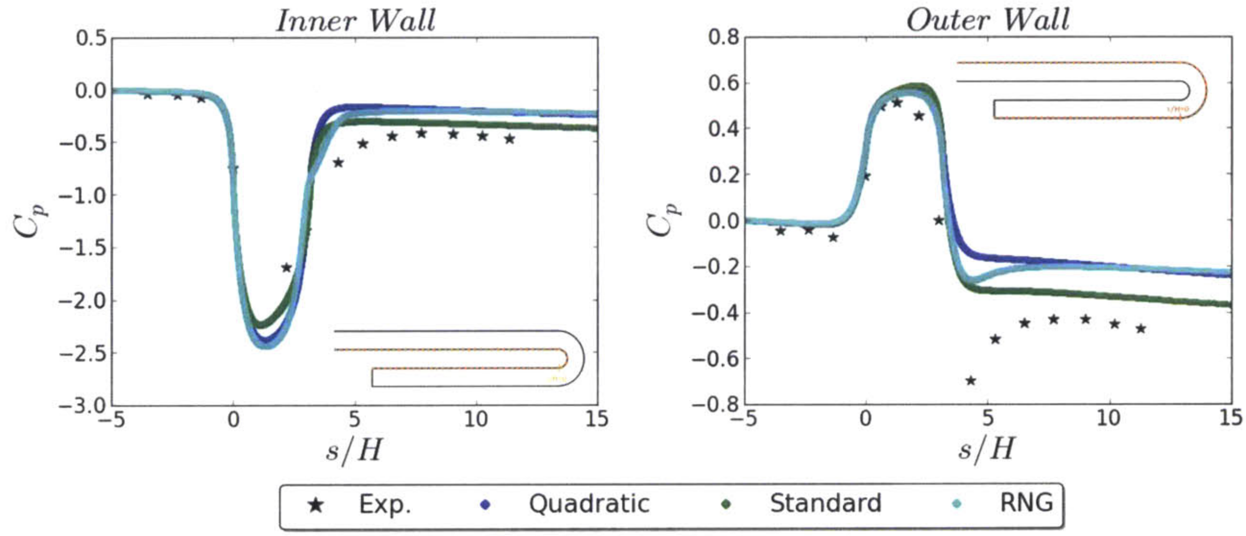

Figure 4.11 U-channel pressure coefficients on the wall

To gain a better understanding for the mechanisms underlying the differing performances between the quadratic, standard, and RNG *k*-ε models, the velocity, turbulent kinetic energy, and turbulent viscosity profiles have been examined. The *x*- and *y*-components of velocity are displayed in Figure 4.12 and Figure 4.13, respectively. As can be seen, all three models yield similar distributions for the *x*- and *y*-components of velocity inside the 180° bend. Both the RNG and quadratic models resolve the separation region that occurs immediately after the pipe bend; however, the RNG model predicts a substantially larger separation region.

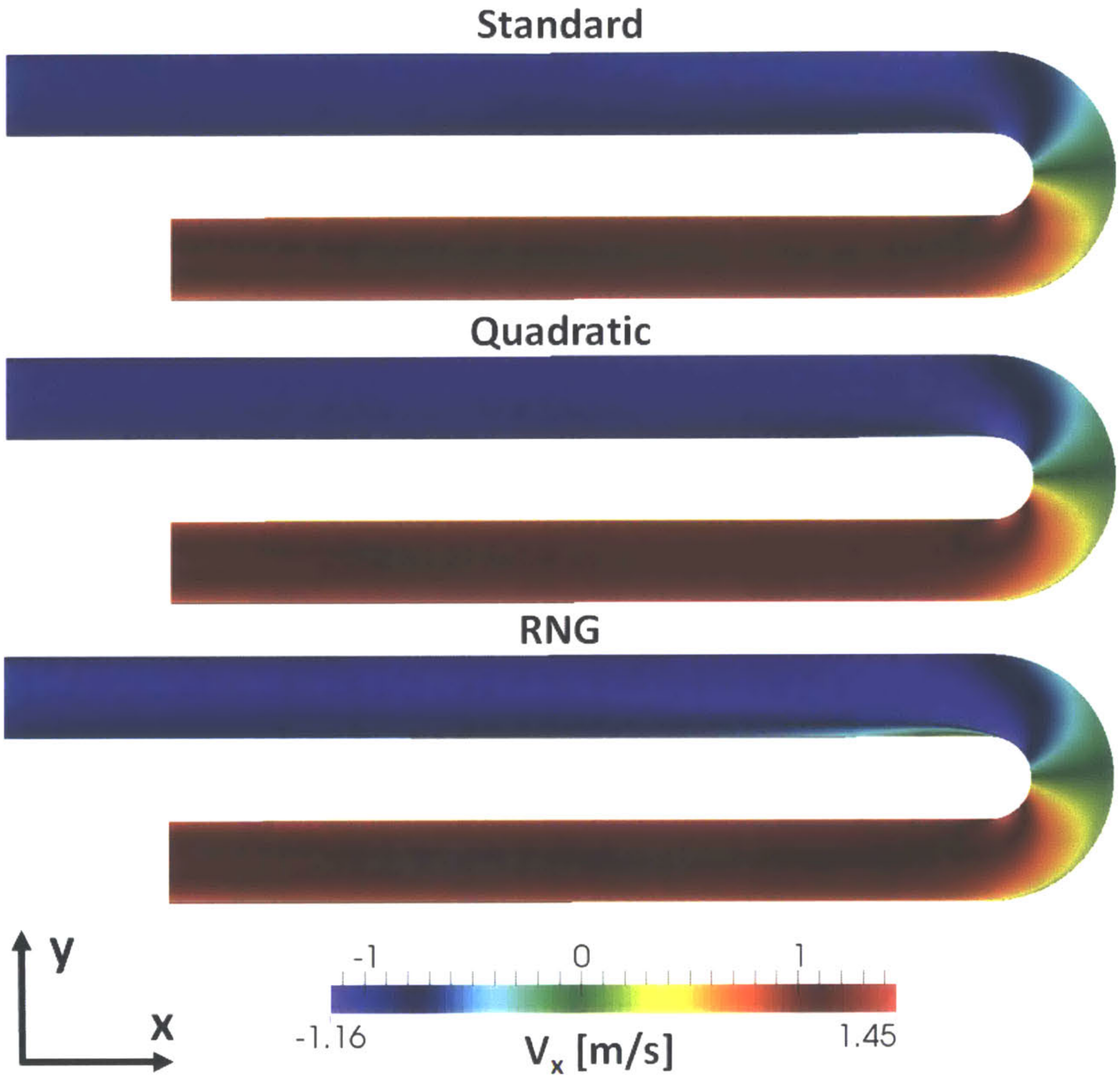

Figure 4.12 U-channel x-component of velocity

The turbulent kinetic energy for all three models is displayed in Figure 4.14. The quadratic and standard models have similar profiles throughout the domain, but differ with respect to their magnitudes, with the standard model predicting roughly twice the value of the quadratic model. Likewise, the RNG and quadratic models have similar magnitudes for the turbulent kinetic energy, but differ with respect to the distribution. The quadratic model predicts a larger value of k for the bulk flow at the end of the bend that extends into the duct for quite some distance; the RNG model predicts a weaker distribution of k in the bulk flow at the end of the bend, but rather peaks near the inner wall immediately after the bend in the separation region.

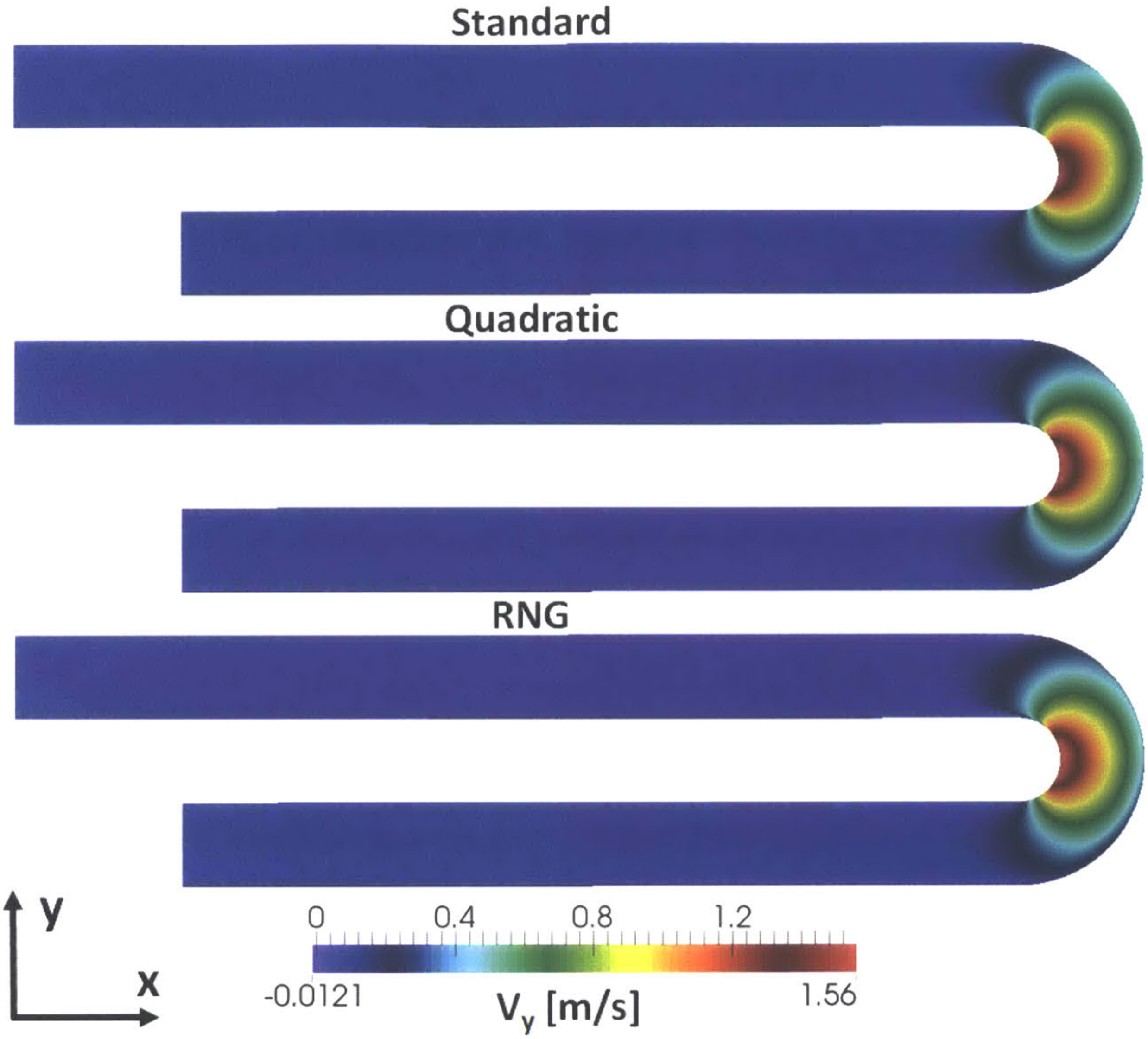

Figure 4.13 U-channel y-component of velocity

Lastly, the turbulent viscosity is shown in Figure 4.15, and it is different for all three models. The standard and quadratic model predict similar magnitudes for the turbulent viscosity, but the standard model predicts its strong development at the beginning of the pipe bend, whereas the quadratic model predicts it towards the end of the bend. The RNG model prediction is an order of magnitude smaller.

In consideration of the velocity, turbulent kinetic energy, and turbulent viscosity distributions, let us revisit the U-channel mean velocity plots in Figure 4.10. Recall from Section 2.4 that the differences between the standard and quadratic model formulations include the quadratic stress-strain constitutive relation and the variable C_μ coefficient, which allow the quadratic model to resolve the turbulent normal stress anisotropy. Both of these factors prevent the quadratic model from overpredicting the magnitude of the turbulent kinetic energy and turbulent viscosity, which thereby allow it to achieve a better prediction of the velocity distribution at θ=180°.

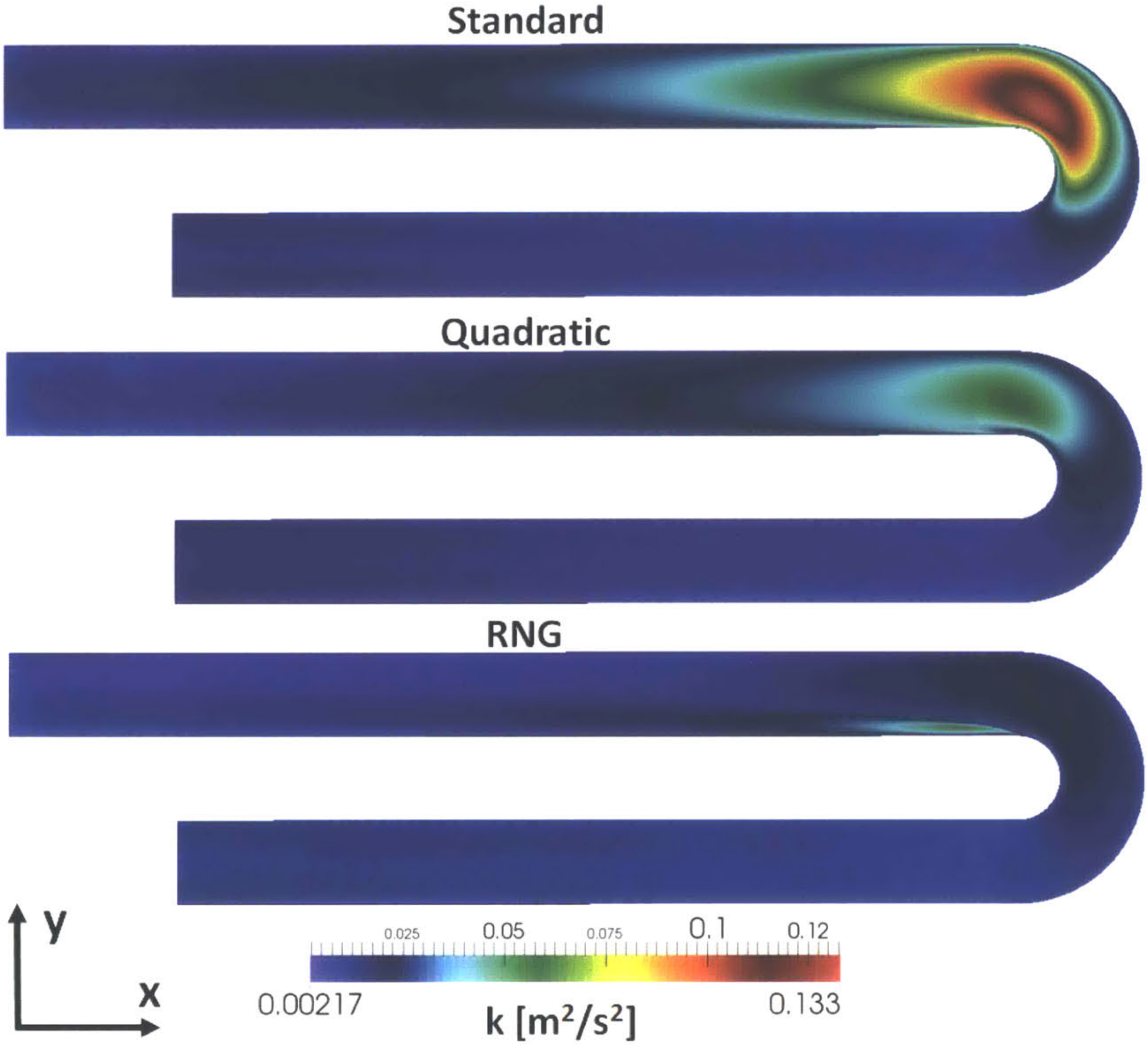

Figure 4.14 U-channel turbulent kinetic energy profiles

Even so, the quadratic model still struggles with this test case and yields predictions for the velocity profiles that differ considerably with the experimental results. This is attributable to the fact that the quadratic terms are not sufficient for modeling this type of flow problem. The cubic stress-strain terms—which pertain to streamline curvature and rotation—are needed to adequately model this type of problem. Since only the quadratic terms have been implemented and validated, it is entirely expected that it would struggle with the U-channel problem. Future work will seek to incorporate the cubic terms into the model, and the U-channel case will be revisited.

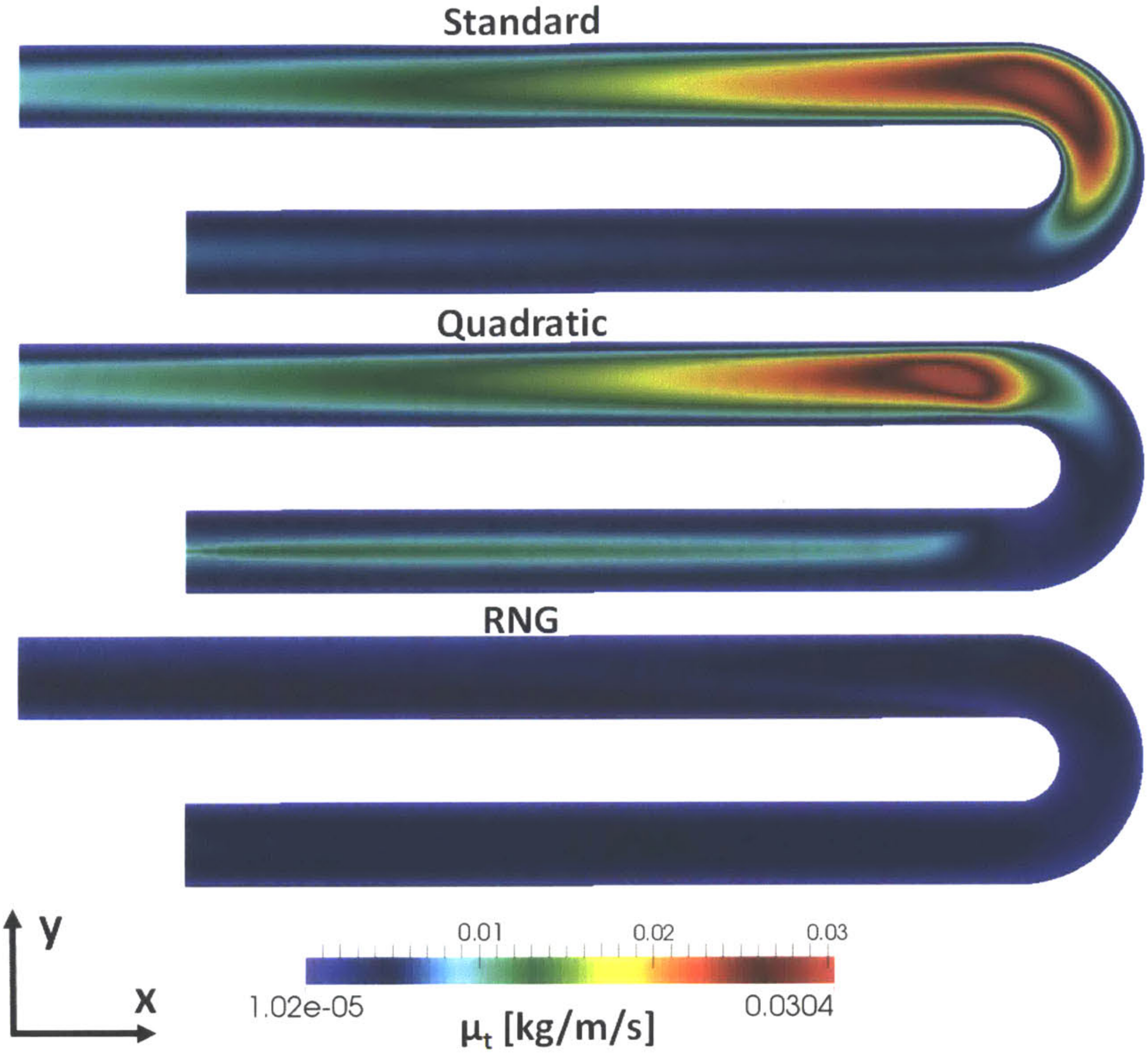

Figure 4.15 U-channel turbulent viscosity profiles

The RNG model's ability to predict the flow separation region immediately after the 180° bend is the key to its better predictions. This is due to the additional ad hoc source term in the ε transport equation (Eq. (2.44)). This term accounts for "some" of the effect of the mean flow distortion of the turbulence dissipation, and such capability leads to improved predictions on high strain rate and high streamline curvature flows.

4.2.4 Grid Refinement Study

The velocity profiles at $s/H = 2 + \pi$ and the pressure coefficients at the inner wall are plotted for each model in Figure 4.16 and Figure 4.17 to demonstrate the convergence of the solution for the fine mesh results presented in the previous section. As can be seen, the velocities and pressure coefficients are overlaid upon one another for all three mesh refinements, which suggests that a converged result has been obtained. A Richardson extrapolation of maximum velocity in the computational domain was performed for all three models, and the order of convergence and error on the finest grid are listed in Table 4.6.

As with the square duct test case, the results of the Richardson extrapolation yield counterintuitive results for the order of accuracy and error on the finest grid. Table 4.6 lists the maximum velocity values for all three grid refinements. The spread of these values is quite small, which suggests that grid refinement has negligible impact on the simulation result due to the relatively simplistic geometry of the U-channel.

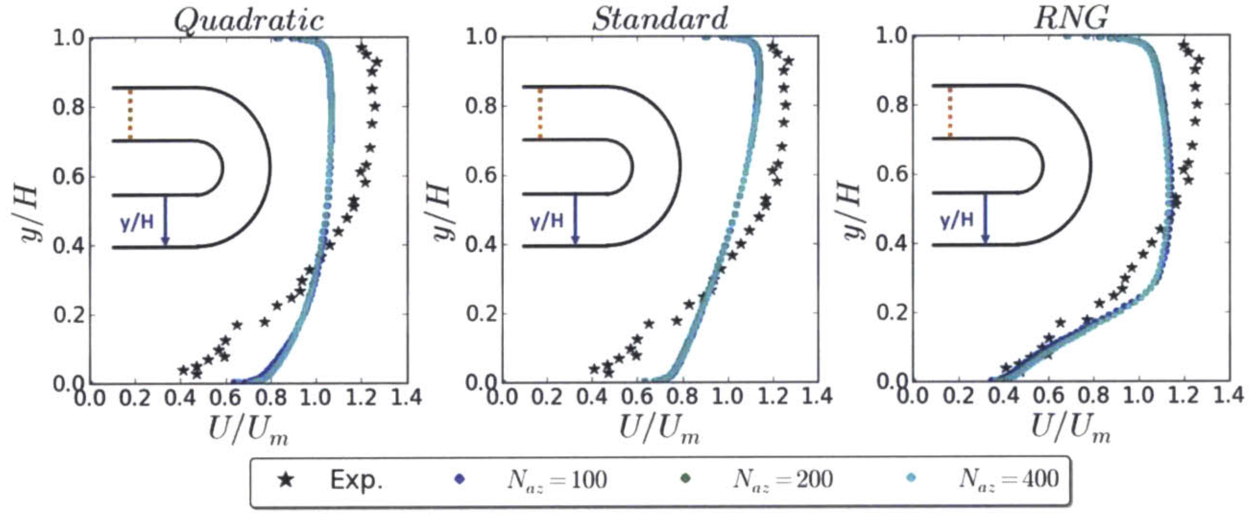

Figure 4.16 Convergence of velocity profile at $s/H = \pi + 2$

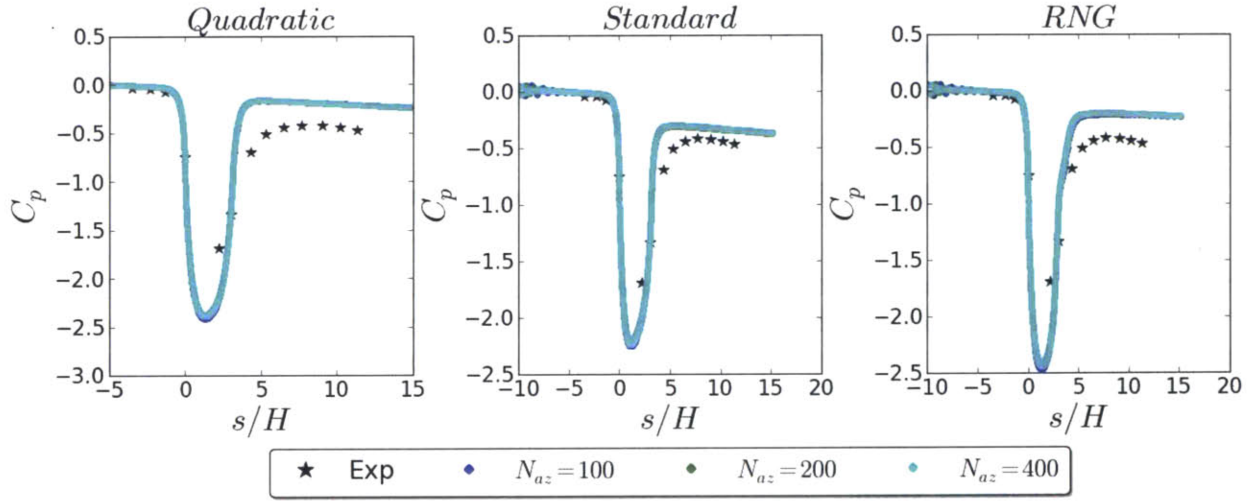

Figure 4.17 Convergence of pressure coefficient on inner wall

Table 4.6 U-channel Richardson extrapolation results

	Quadratic	***Standard***	***RNG***
V_{max}/V_b: ***h***	1.0655	1.1370	1.1309
V_{max}/V_b: ***2h***	1.0662	1.1397	1.1335
V_{max}/V_b: ***4h***	1.0664	1.1350	1.1431
Max Spread [Absolute]	0.0009	0.0047	0.0122
Order of Accuracy	1.807	0.800	1.885
Error on Finest Grid [%]	0.0280	0.365	0.0966

5 Quadratic Model Validation of Nuclear Fuel Configurations

The quadratic model has been applied to triangular and square fuel rod arrays in order to assess its implementation and readiness for reactor simulations. A comparison with the standard k-ε model has been performed in order to highlight the importance of capturing the secondary flows generated by normal stress anisotropy.

5.1 Triangular Fuel Rod Array

5.1.1 *Experimental Setup*

A series of velocity and wall shear stress measurements for several Reynolds numbers were performed by Mantlik et al. [19] on a bare triangular rod array at NRI in the Czech Republic. The experiments were performed in a wind tunnel, using nineteen 120 mm outer diameter (OD) rods of 6 m length, with a pitch-to-diameter ratio of 1.17. Measurements were recorded at a distance of 5.6 m from the inlet to ensure that fully-developed flow had been achieved. Pitot and Preston tubes of 0.8 mm (OD) were used to measure the velocity and wall shear stress profiles. The measurements were performed in a central subchannel so that it could be considered to be an elementary flow cell of an infinite rod bundle. The Reynolds number considered in these simulations is 181,200, and the experimental conditions for this experiment are summarized in Table 5.1.

Table 5.1 Experimental conditions for Mantlik et al. [19]

ρ [kg/m^3]	μ [kg/m/s]	V_b [m/s]	Re
1.131	$1.8\text{x}10^{-5}$	47.16	181,200

5.1.2 *Computational Setup*

Due to the inherent symmetry of the problem, it is sufficient to describe a smaller domain with the prescription of appropriate symmetry boundary conditions (Figure 5.1). The domain comprises six elementary flow cells. The rationale for this domain selection originates from leveraging the current implementation of the symmetry (zero-gradient) boundary conditions in Hydra-TH, which are required to be specified at a surface where its normal directly coincides with a coordinate direction.

The dimensions of an elementary flow cell are displayed in Figure 5.2. Three prism layers—each with a thickness of 1 mm—were employed in order to ensure stability to the wall functions to lead to a converged solution. A grid refinement study has also been performed for these simulations, but is deferred until later in this section.

The boundary conditions applied to the computational domain are highlighted in Figure 5.3, where the sidesets are also shown for clarity. Wall boundary conditions ($V_x = V_y = V_z = 0$) were applied at both of the fuel rod surfaces. Symmetry boundary conditions were enforced by setting the velocity component normal to the surface equal to 0. An inlet velocity (sideset 1) of 47.16 m/s was prescribed and a reference pressure equal to 0 was specified for the outlet (sideset 2).

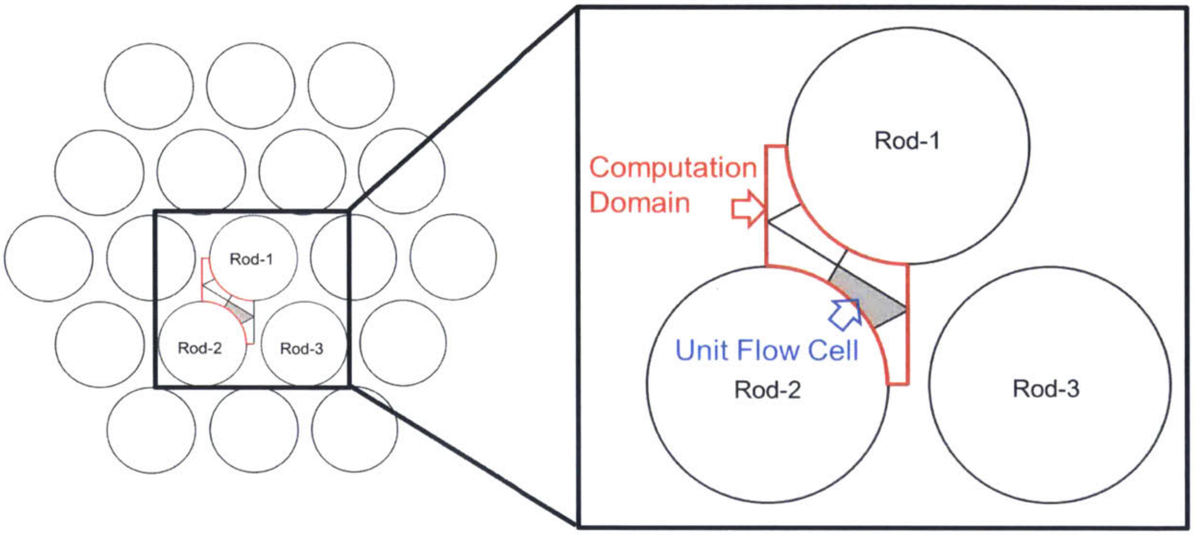

Figure 5.1 Triangular fuel rod array computational domain

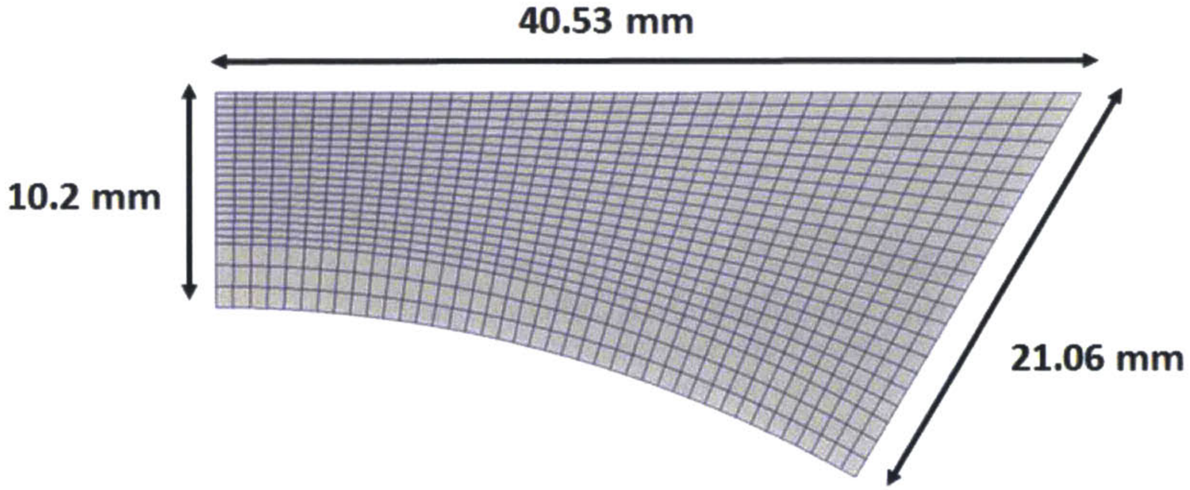

Figure 5.2 Elementary flow cell dimensions for triangular fuel rod array [19]

Three grids of increasing refinement were used for this study. Refinement in the axial direction (z) was fixed constant at 60 elements, while the radial and azimuthal spacing was refined by a factor of 2. Three wall layer elements, each of 1 mm thickness were used for all mesh sizes. The cross-sectional view of all three elementary flow cell mesh sizes is illustrated in Figure 5.4 and the mesh sizes are listed in Table 5.2.

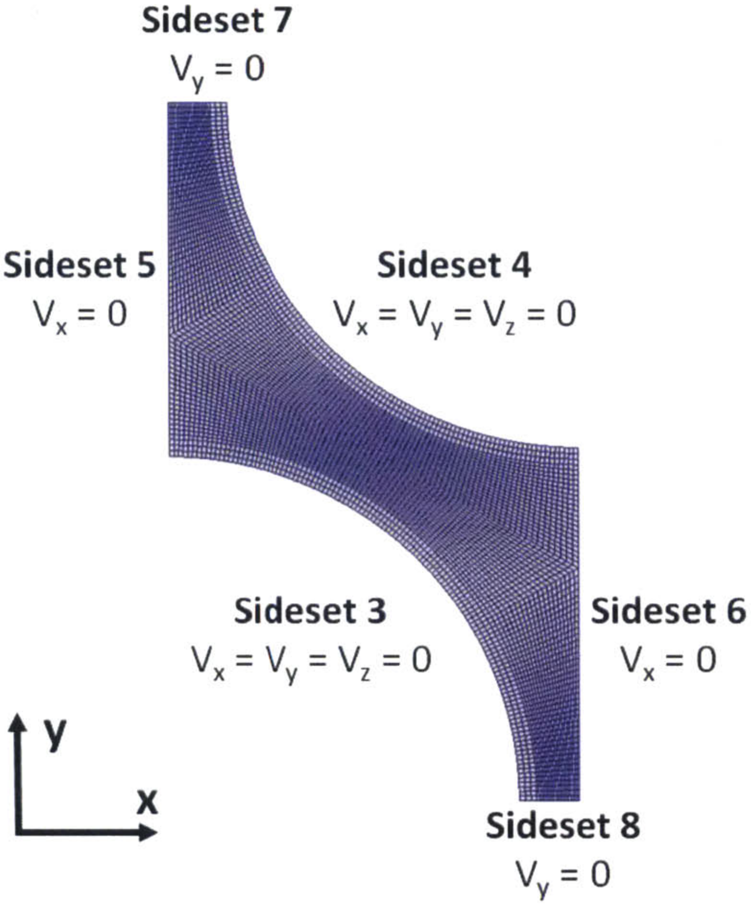

Figure 5.3 Boundary conditions for triangular fuel rod array simulations

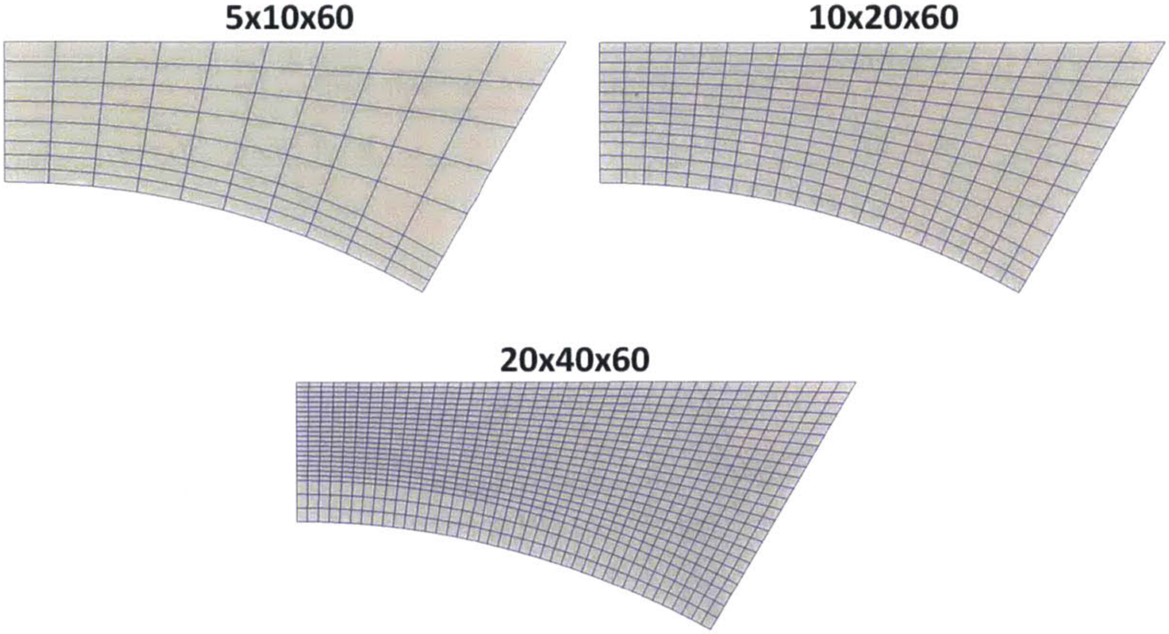

Figure 5.4 Mesh refinements examined for triangular fuel rod array simulations

Table 5.2 Mesh refinements examined for triangular fuel rod array simulations

Wall Elements	*r*	*θ*	*z*	*Total Elements*
3	5	10	60	28,800
3	10	20	60	93,600
3	20	40	60	331,200

5.1.3 Results

The radial velocity profile predictions for the quadratic model are presented in Figure 5.5 along with the experimental results. As can be seen, the quadratic model matches the velocity profiles at the angular locations of φ=15° and φ=30°. For the φ=0° case, the model accurately predicts the velocity in the near wall region, but steadily drifts away from the experimental results as the normal distance to the wall is increased. The quadratic model is also able to match the shape of the wall shear stress distribution measurements, but with a slight underprediction in the φ=0-12° region.

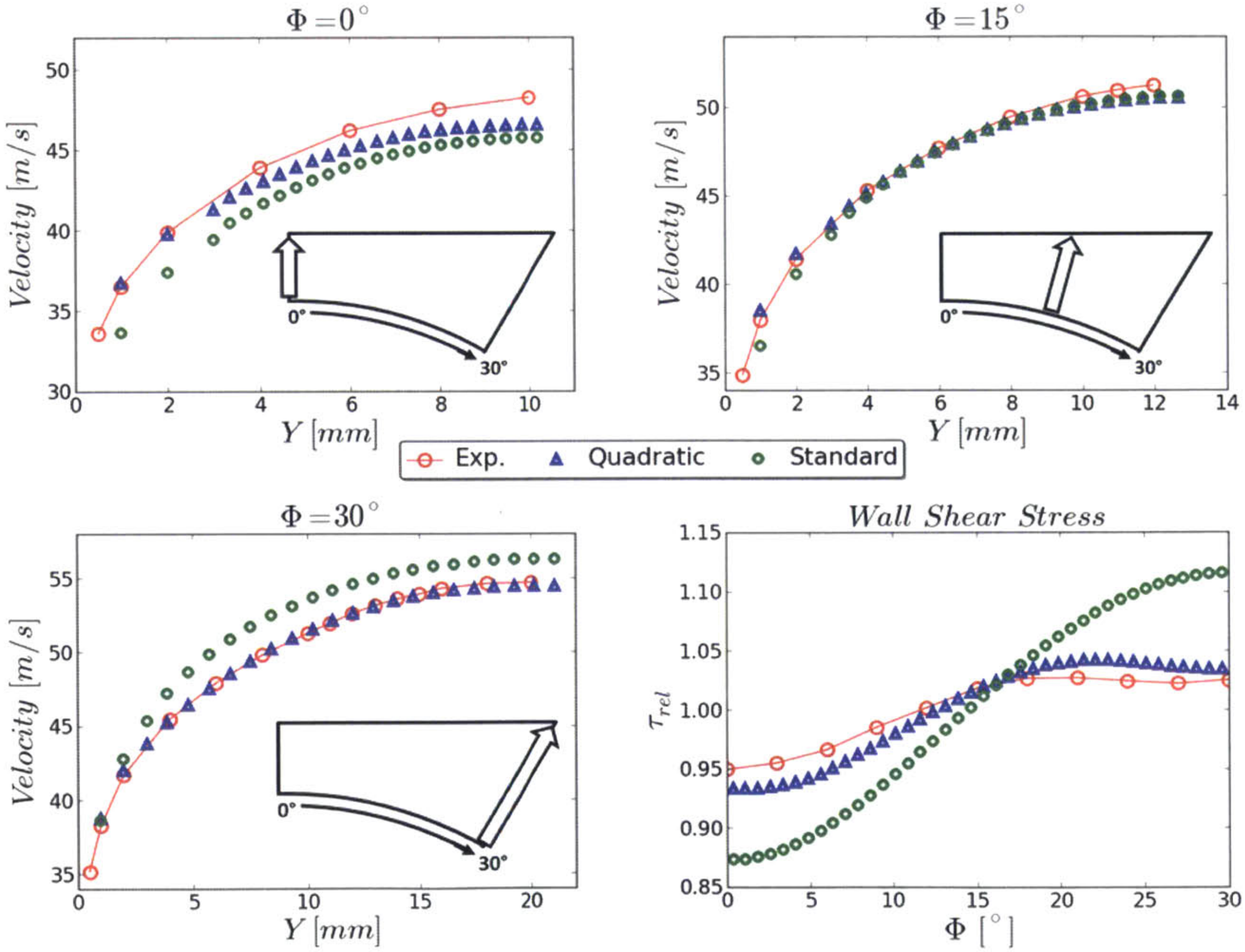

Figure 5.5 Velocity and wall shear stress distributions (Mantlik et al. [19])

The results of standard k-ε model applied to the triangular rod array are also displayed in Figure 5.5. Accurate predictions are achieved for the velocity profile at φ=15°; however, the standard model underpredicts the velocity profile in the narrow region (φ=0°) and overpredicts it at the φ=30° location. Further, the standard model yields predictions for the wall shear stress that monotonically increase from φ=0-30° and consequently do not coincide with the experimental values. Such behavior is a common observation and known limitation of the standard k-ε model that is attributed to the lack of secondary flow prediction, which acts to redistribute the turbulence levels and velocities inside the channel.

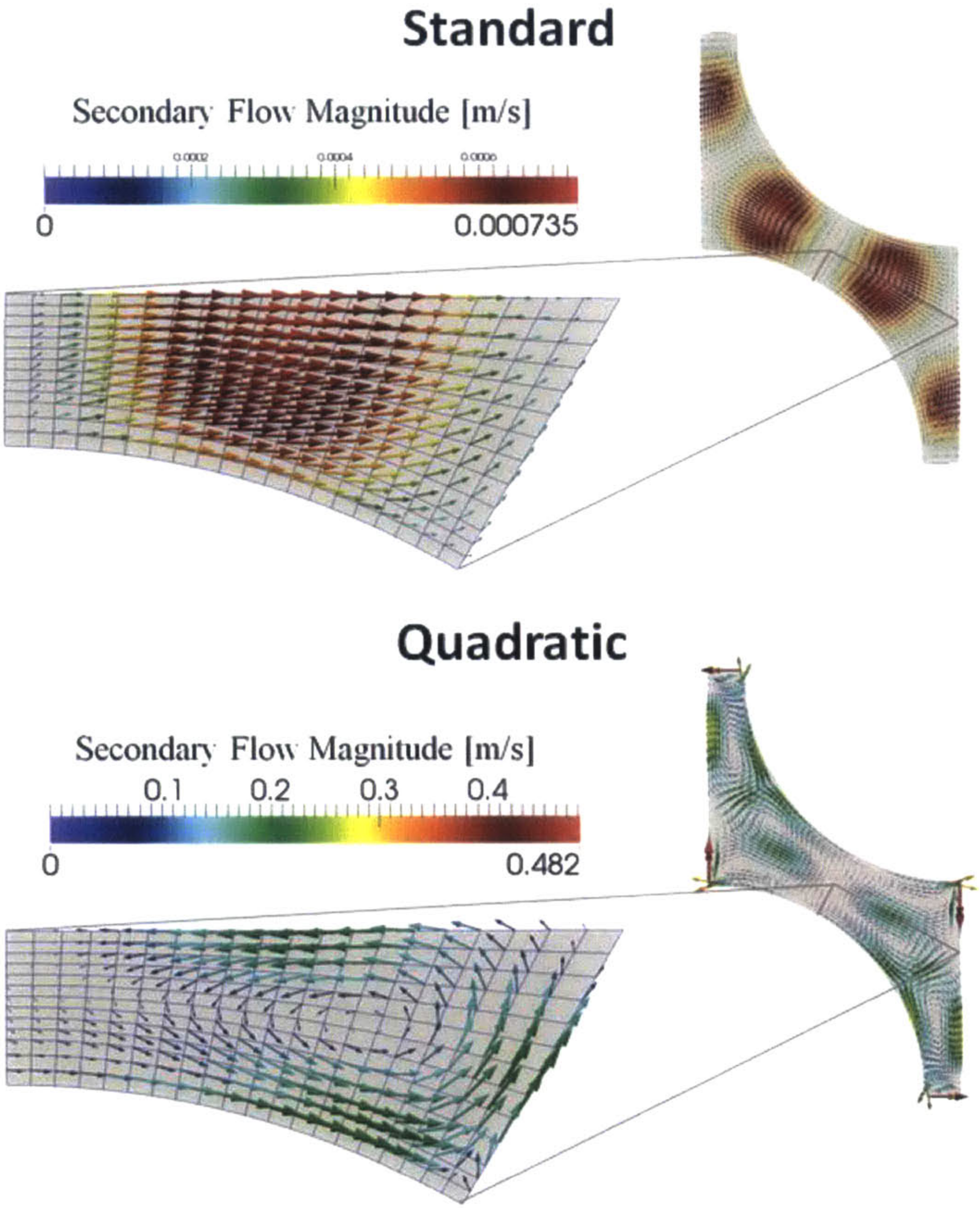

Figure 5.6 Secondary flow profiles for triangular fuel rod array simulations

Figure 5.6 illustrates the secondary flows at the plane of measurement for both the quadratic and standard models. A vortex that spans the entire elementary flow cell is observed for the quadratic model, whereas the standard model predicts negligible secondary motion that is most likely spurious velocities produced as a consequence of the linear eddy viscosity model. Further, the quadratic model predicts magnitudes on the order of 0.1% (in accordance with the experimental measurements of Vonka [5]). These observations confirm that the quadratic model is able to capture the anisotropy driven secondary flow profile, which allows it to resolve the turbulence redistribution, leading to the more uniform axial velocity and wall shear stress profiles depicted in Figure 5.5.

Greater inspection of the secondary flows predicted by the quadratic model sheds insight into why the velocity profile and wall shear stress distributions were underpredicted in the φ=0-12° regime. The secondary flow profile is noticeably weaker in this region, which suggests an insufficient redistribution of turbulence to smooth out the flow profile. This is an artifact of the code framework that will have to be examined further. One possible source for this may be an insufficient boundary condition prescription. The quadratic model predicts strange values in the corners of the geometry that leads to large vectors pointing outside of the domain. This is an indication that the symmetry boundary conditions need to be revised to accommodate anisotropic stress tensors.

5.1.4 Grid Refinement Study

The grid convergence of the axial velocity profile at φ=30° and wall shear stress distribution for the quadratic and standard k-ε models for the triangular array are displayed in Figure 5.7 and Figure 5.8, respectively. The standard model behaves near identically for all three refinements for both cases, which is a prime indicator that grid convergence is achieved. Conversely, the quadratic model did not achieve proper convergence for the coarsest mesh. The two finer meshes did achieve convergence and their values are almost superimposed, which implies that good convergence is achieved for the two fine grids.

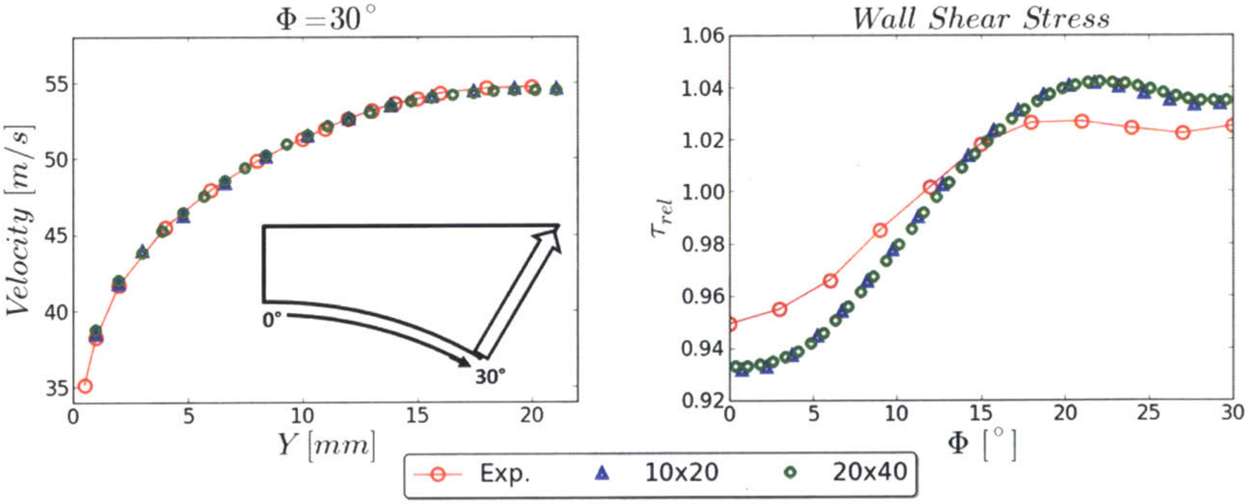

Figure 5.7 Triangular fuel rod mesh convergence (quadratic k-ε model)

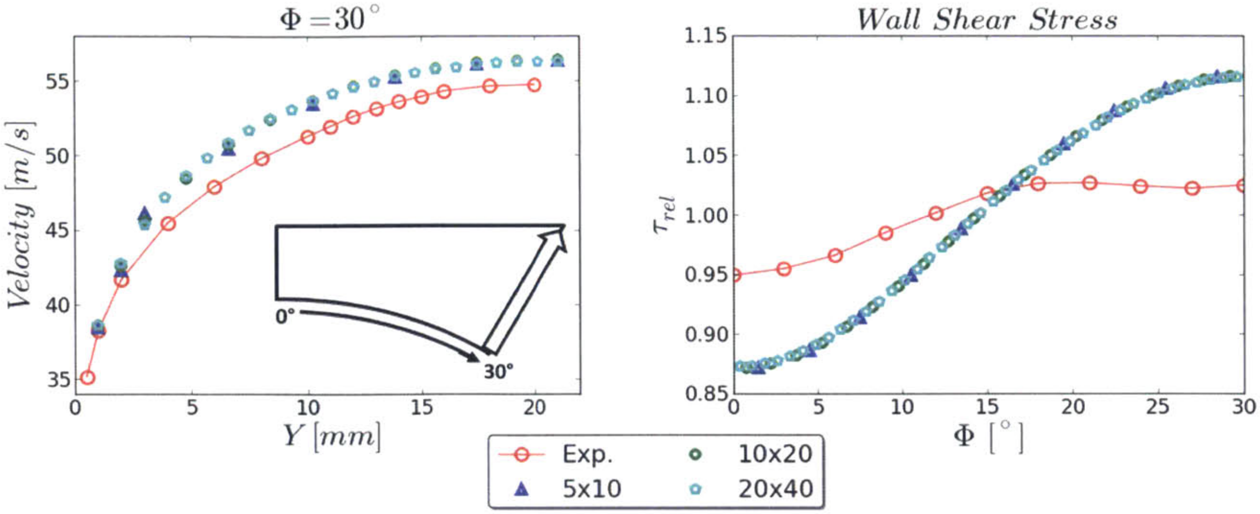

Figure 5.8 Triangular fuel rod mesh convergence (standard *k*-ε model)

A Richardson extrapolation of the maximum velocity in the computational domain could only be performed for the standard model, as the coarsest mesh for the quadratic model did not converge. The order of convergence and error on the finest grid for the standard model are listed in Table 5.3.

Again, the results of the Richardson extrapolation yield counterintuitive results for the order of accuracy and error on the finest grid for the standard model. Table 5.3 lists the maximum velocity for all three grid refinements, which shows that the differences between them is quite small. Likewise, the quadratic model results for the two finest grids are in close agreement. Both of these observations suggest that the results reported for the finest mesh reflect a grid-converged solution.

Table 5.3 Triangular fuel rod array Richardson extrapolation results

	Quadratic	***Standard***
V_{max}: h [m/s]	54.485	56.285
V_{max}: 2h [m/s]	54.603	56.381
V_{max}: 4h [m/s]	N/A	56.299
Max Spread [m/s]	0.118	0.096
Order of Accuracy	N/A	0.227
Error on Finest Grid [m/s]	N/A	0.562

5.2 Square Fuel Rod Array

5.2.1 Experimental Setup

A similar analysis of velocity and wall shear stress measurements for varying Reynolds numbers was performed by Hooper and Wood [20] for a bare square rod array in a wind tunnel. The experimental setup consisted of six rods of 7 cm radius and 9.14 m length, with a pitch-to-diameter ratio of 1.107. Pitot and Preston tubes of 1.6 mm OD were used to measure the velocity and wall shear stress profiles just before the outlet. The Reynolds number considered in these simulations is 207,600, and the experimental conditions for this experiment are summarized in Table 5.4.

Table 5.4 Experimental conditions for Hooper and Wood [20]

ρ [kg/m^3]	*μ [kg/m/s]*	*V_b [m/s]*	*Re*
1	1x10^{-5}	26.48	207,600

5.2.2 Computational Setup

The computational domain comprises two elementary flow cells, as depicted in Figure 5.9. The dimensions of the elementary flow cell are described in Figure 5.10. Again, three prism layers, each with a thickness of 1 mm have been utilized.

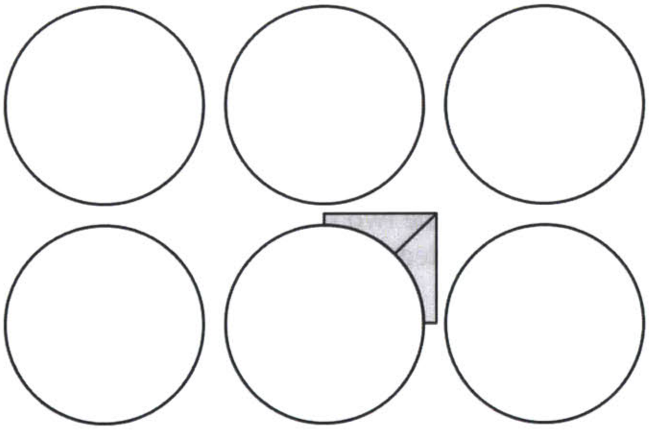

Figure 5.9 Square fuel rod array computational domain

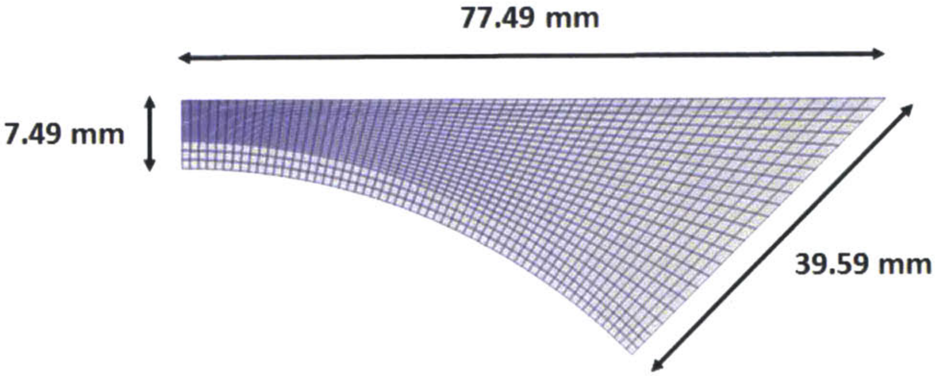

Figure 5.10 Elementary flow cell dimensions for square fuel rod array [20]

The boundary conditions applied to the computational domain are highlighted in Figure 5.11. Wall boundary conditions were applied at the fuel rod surface. Symmetry boundary conditions were enforced by setting the component of velocity normal to the surface equal to 0. An inlet velocity (sideset 1) of 26.48 m/s was prescribed and a reference pressure equal to 0 was specified for the outlet (sideset 2).

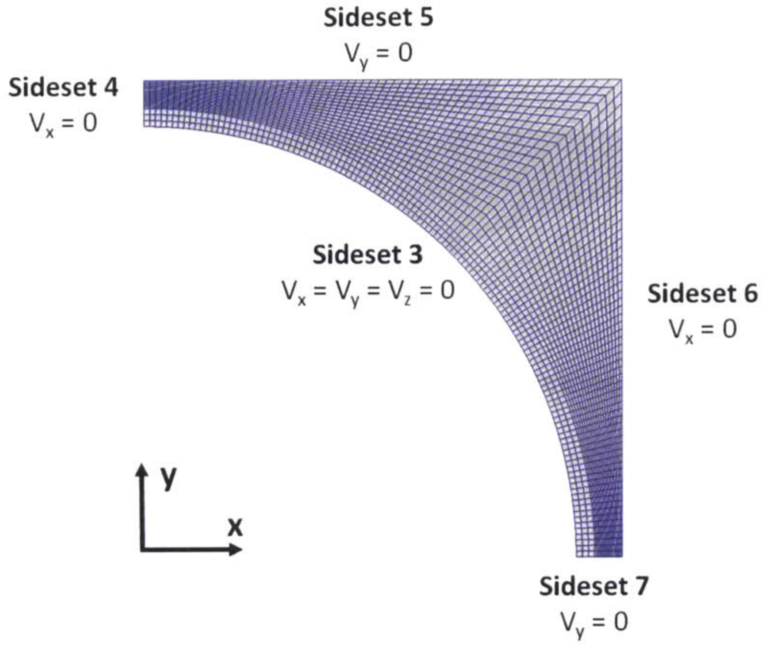

Figure 5.11 Boundary conditions for square fuel rod array simulations

Three grids of increasing refinement were used for this study. Refinement in the axial direction (z) was fixed constant at 60 elements, while the radial and azimuthal spacing was refined by a factor of 2. Three wall layer elements, each of 1 mm thickness were used for all mesh sizes. The cross-sectional view of all three elementary flow cell mesh sizes is illustrated in Figure 5.12 and the mesh sizes are listed in Table 5.5.

Table 5.5 Mesh refinements examined for square fuel rod array simulations

Wall Elements	*r*	*θ*	*z*	*Total Elements*
3	5	15	60	14,400
3	10	30	60	46,800
3	20	60	60	165,600

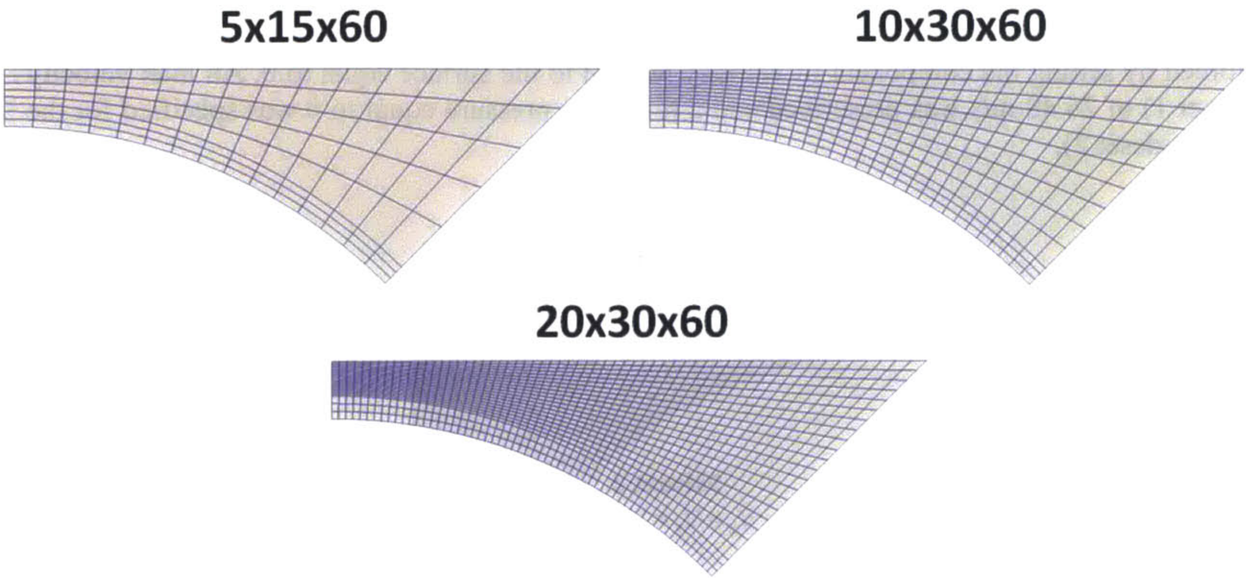

Figure 5.12 Mesh refinements examined for square fuel rod array simulations

5.2.3 ***Results***

Simulation results for the square rod array are shown in Figure 5.13, where the standard and quadratic models are both plotted for comparison. The quadratic model matches the radial velocity profile at φ=45°, but drastically underpredicts the velocity profile at the φ=0° location. The wall shear stress prediction is quite unexpected, as it initially increases with the angle φ, levels off around φ=30-35°, and dips down considerably afterwards. The standard model underpredicts the velocity in the near-wall region—to an even greater extent than the quadratic model—and overpredicts it at the φ=45° location; likewise, the predicted wall shear stress profile is monotonically increasing from φ=0-45° and therefore doesn't match the experimental results.

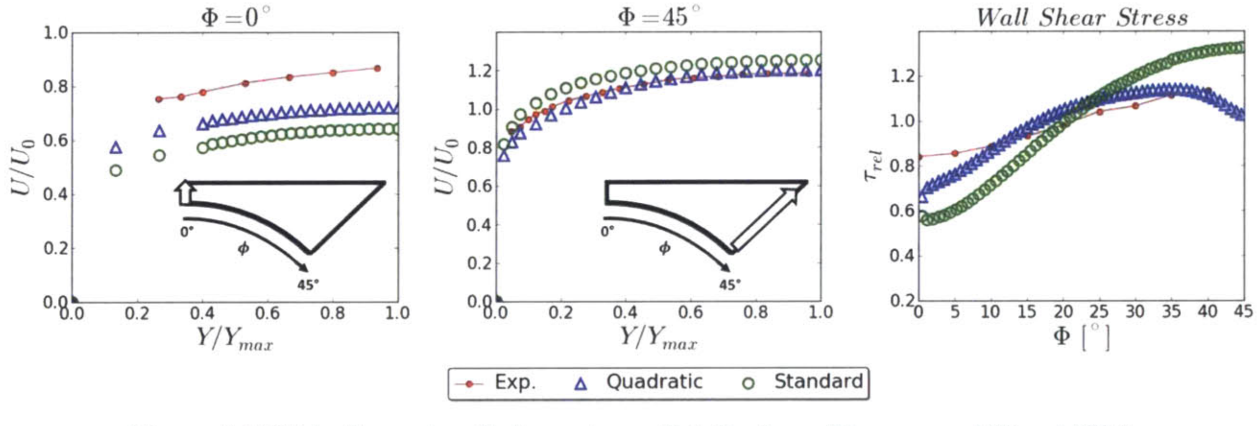

Figure 5.13 Velocity and wall shear stress distributions (Hooper and Wood [20])

The secondary flow profiles for both the quadratic and standard model are shown in Figure 5.14. As observed with the triangular array, the quadratic model predicts a spiraling vortex with a magnitude that is approximately 0.1% that of axial velocity profile, while the standard model predicts negligible secondary flows. Again, the secondary flow profile breaks down near the corners of the simulation for the quadratic model, which therefore points to an issue with the boundary conditions and explains the model's weak performance in this region.

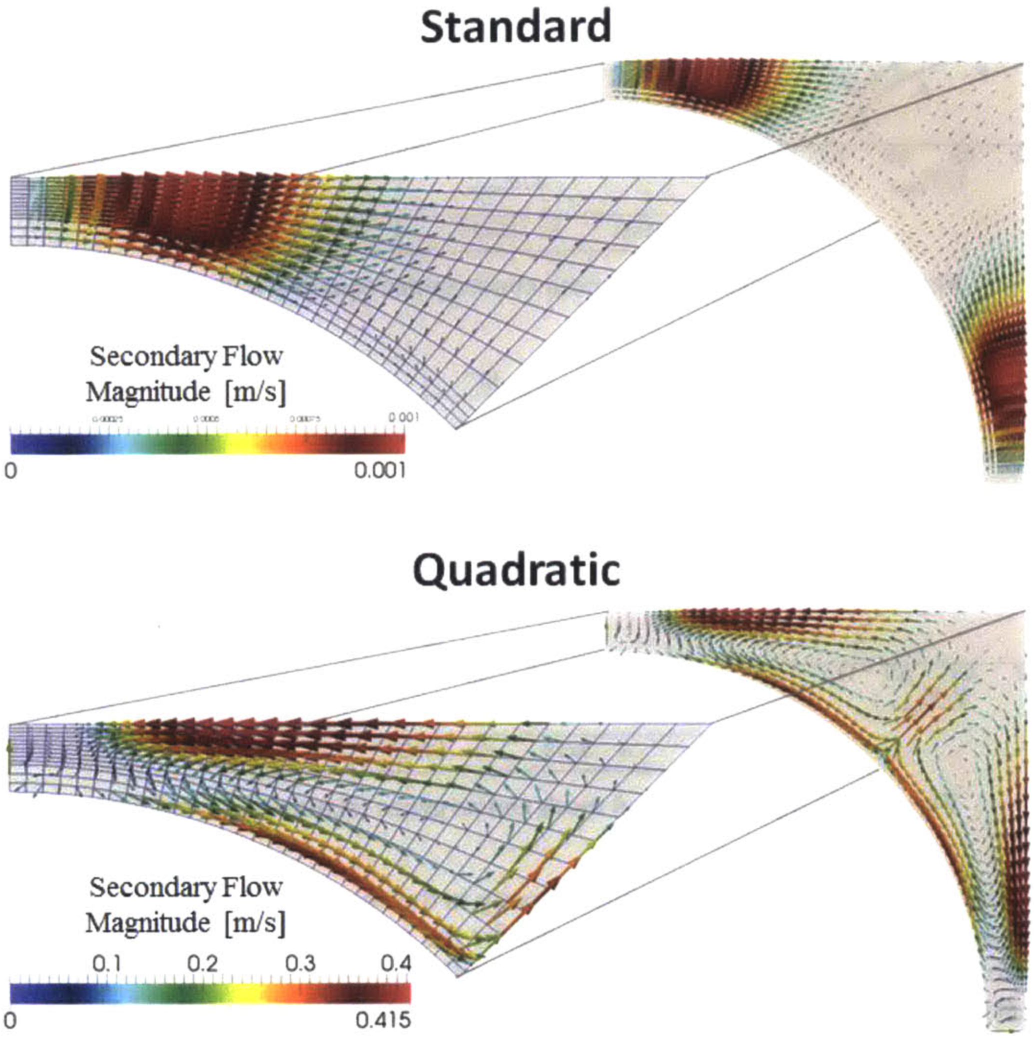

Figure 5.14 Secondary flow profiles for square fuel rod array simulations

5.2.4 Grid Refinement Study

The grid convergence of the quadratic and standard *k-ε* models for the square array are displayed in Figure 5.15 and Figure 5.16, respectively. The standard model behaves near identically for all three refinements for both cases, which is a prime indicator that grid convergence is achieved. As with the triangular fuel rod array simulations, the quadratic model did not achieve proper convergence for the coarsest mesh in both instances. The two finer meshes did achieve convergence and their values are almost superimposed, which implies that good convergence is achieved for the two fine grids.

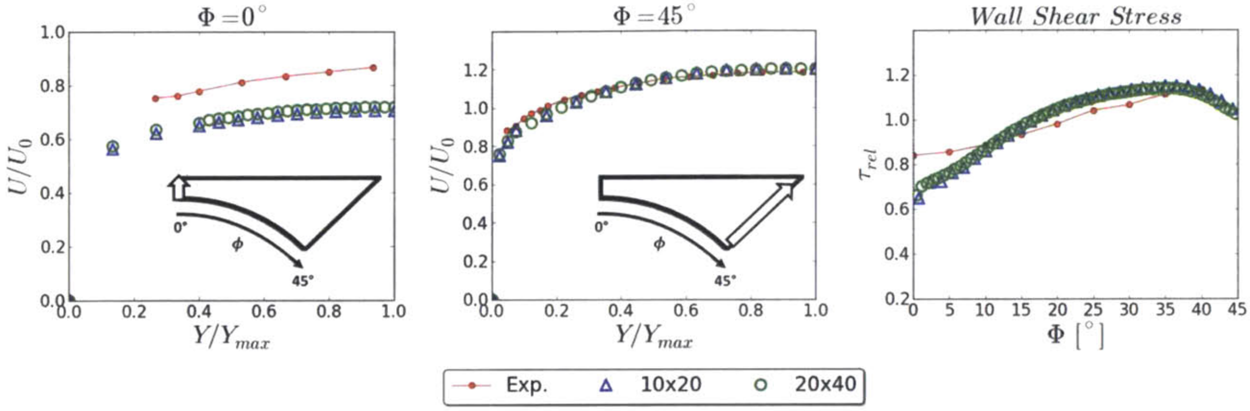

Figure 5.15 Square fuel rod mesh convergence (quadratic *k*-ε model)

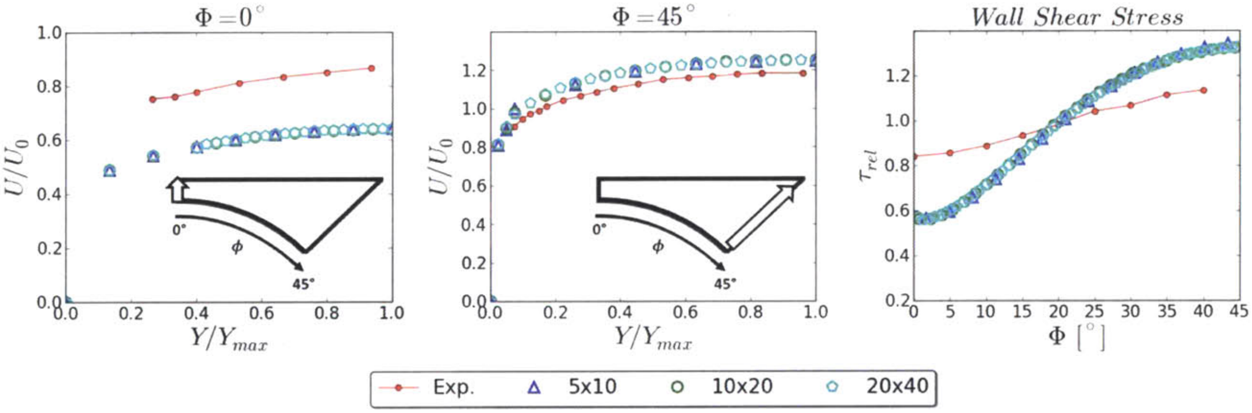

Figure 5.16 Square fuel rod mesh convergence (standard *k*-ε model)

A Richardson extrapolation of the maximum velocity in the computational domain was performed only for the standard model as the coarsest mesh for the quadratic model did not converge. The order of convergence and error on the finest grid for the standard model are listed in Table 5.6. While the order of accuracy seems nonsensical, the spread of the maximum velocity values for standard and quadratic models is quite small, which demonstrates that the results reported for the finest mesh reflect a grid-converged solution.

Table 5.6 Square fuel rod array Richardson extrapolation results

	Quadratic	***Standard***
V_{max}: h [m/s]	31.832	33.136
V_{max}: 2h [m/s]	31.8386	33.1349
V_{max}: 4h [m/s]	N/A	33.0303
Max Spread [m/s]	0.0066	0.1057
Order of Accuracy	N/A	6.571
Error on Finest Grid [m/s]	N/A	1.170×10^{-5}

As a final note, the inability of the coarsest mesh to converge for the quadratic model applied to the triangular and square fuel rod arrays is due to the fact that the meshes were simply too coarse. That is, there weren't enough cells to resolve the secondary flows, which prevented the simulation from reaching a solution, and is not attributed to a specific shortcoming of neither the solver nor the model implementation.

6 Best Practices for Application to Fuel Assembly Calculations

A comprehensive sensitivity study for the quadratic model applied to the triangular fuel rod array experiments by Mantlik et al. [19] has been performed in order derive best practices and guidelines for its application to nuclear fuel related problems. The impact that the number of wall layer elements, symmetry boundary conditions, axial refinement, and time-step pose on the convergence and resulting solution are explored herein.

6.1 Wall Layer Treatment

An unexpected challenge encountered in the work is the sensitivity to the mesh resolution in the wall layer region for the quadratic model. More specifically, the use of a single wall layer element was discovered to be insufficient to ensure proper convergence of the quadratic model. Adopting two boundary fitted wall layer elements proves robust on all tested configurations.

Figure 6.1 shows the grid convergence at φ=30° (or lack thereof) of node-centered flow properties for the triangular fuel rod array with the prescription of a single wall layer element of 1 mm thickness, which corresponds to a $y+$ in the range of 50-60. Consideration of only the axial velocity component (V_z) leads to the incorrect conclusion that a grid-converged solution has been obtained. Inspection of additional flow quantities—including the cross-flow velocity components (V_x and V_z), turbulent kinetic energy k, and turbulent dissipation rate ε—reveals stark discrepancies between the values, which signify that a grid-converged solution has not been achieved.

This lack of grid convergence is attributable to the hybrid two-layer scalable wall-function approach that is used in Hydra-TH to model the near-wall region. In this approach—which aims at being applicable over a wide regime of flow conditions and near wall mesh resolutions—the k-equation is solved throughout the entire flow domain, while the ε-equation is solved only up to the wall layer element. (For a more detailed discussion of the precise formulation, the interested reader is referred to the Hydra-TH theory manual [50]). Since the k-equation is solved up to the wall, the resulting solution is therefore particularly sensitive to the elements in the near-wall region, and the resulting grid refinement near the wall has a significant impact on the distribution. Additional wall layers are therefore critical.

The prescription of two or three wall layer elements of similar thickness is a suitable remedy that promotes a grid-converged solution. The grid convergence of relevant flow parameters at φ=30° for the use of two and three wall layer elements are plotted in Figure 6.2 and Figure 6.3 for reference. As can be seen, the velocity components (with the minor exception of V_y) and associated turbulence quantities demonstrate superb convergence between the medium-sized (10x20) and fine (20x40) grids. Note that the coarse (5x10) mesh results are not included as the simulation was unable to converge. This is not associated with a limitation of the quadratic model, and has been attributed to the fact the mesh is simply too coarse to allow adequate resolution.

As a final note, the secondary flow predictions for the cases of one and three wall layer elements on the medium-sized (10x20) grid are displayed in Figure 6.4. (The two wall layer element case yields near identical predictions as the three wall layer element case and therefore has been omitted for brevity). The use of one wall layer element leads to a grossly inaccurate and unphysical prediction of the secondary flows that are an order of magnitude larger than experimental observations. Three wall layer elements allows for proper resolution of the secondary flows that are of the right order of magnitude.

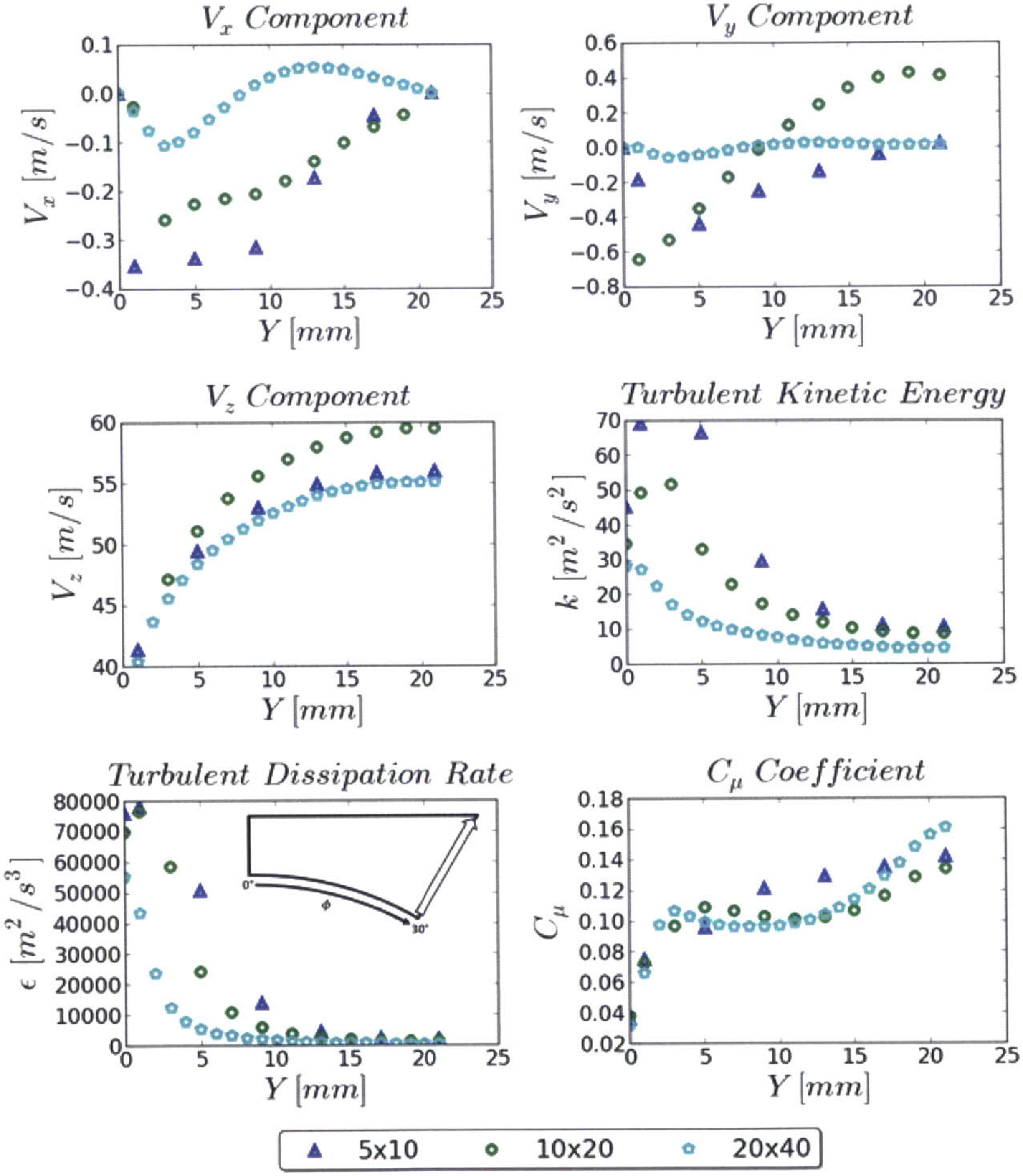

Figure 6.1 Lack of grid convergence for 1 wall layer element (Mantlik et al. [19] at φ=30°)

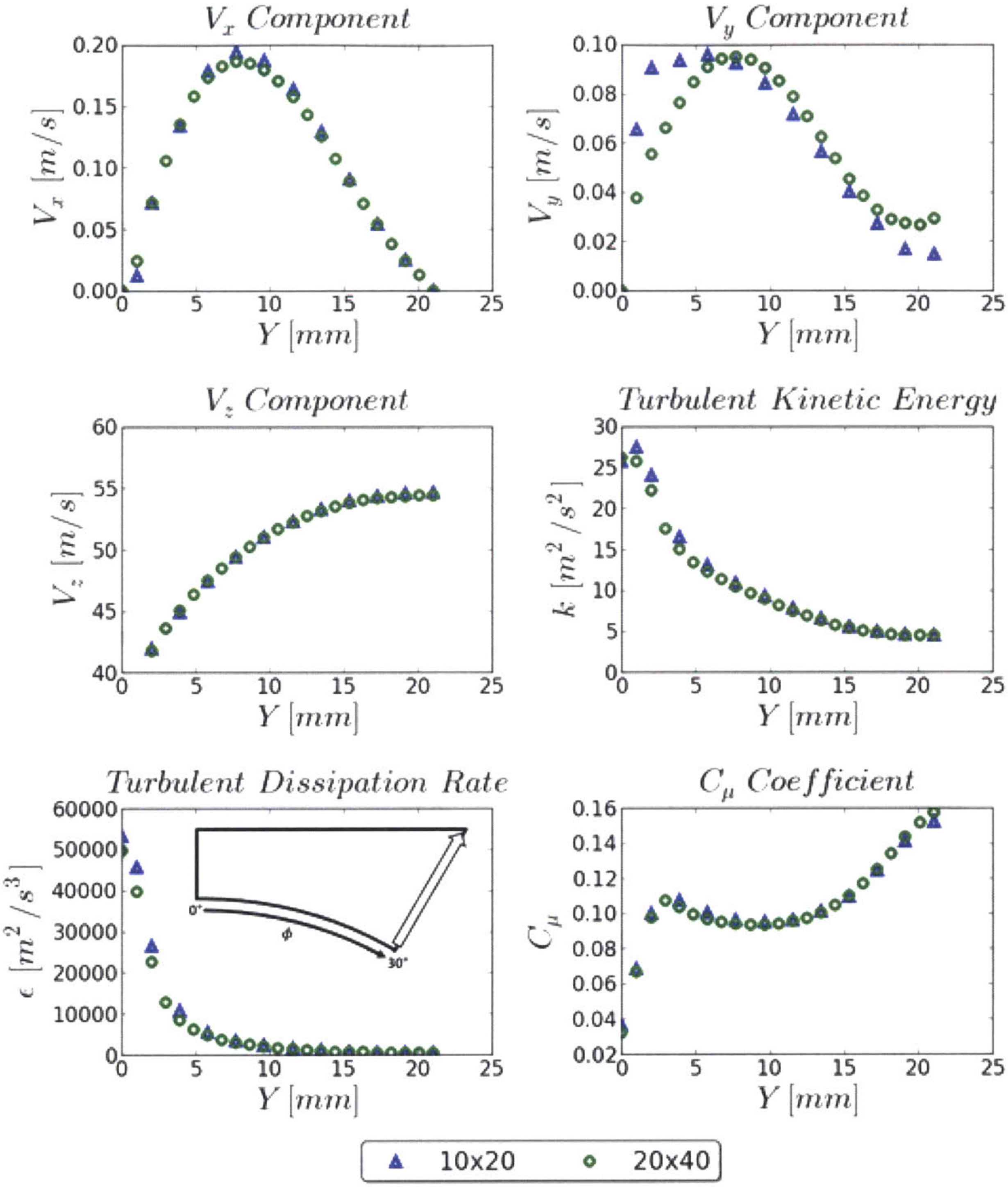

Figure 6.2 Grid convergence using 2 wall layer elements (Mantlik et al. [19] at φ=30°)

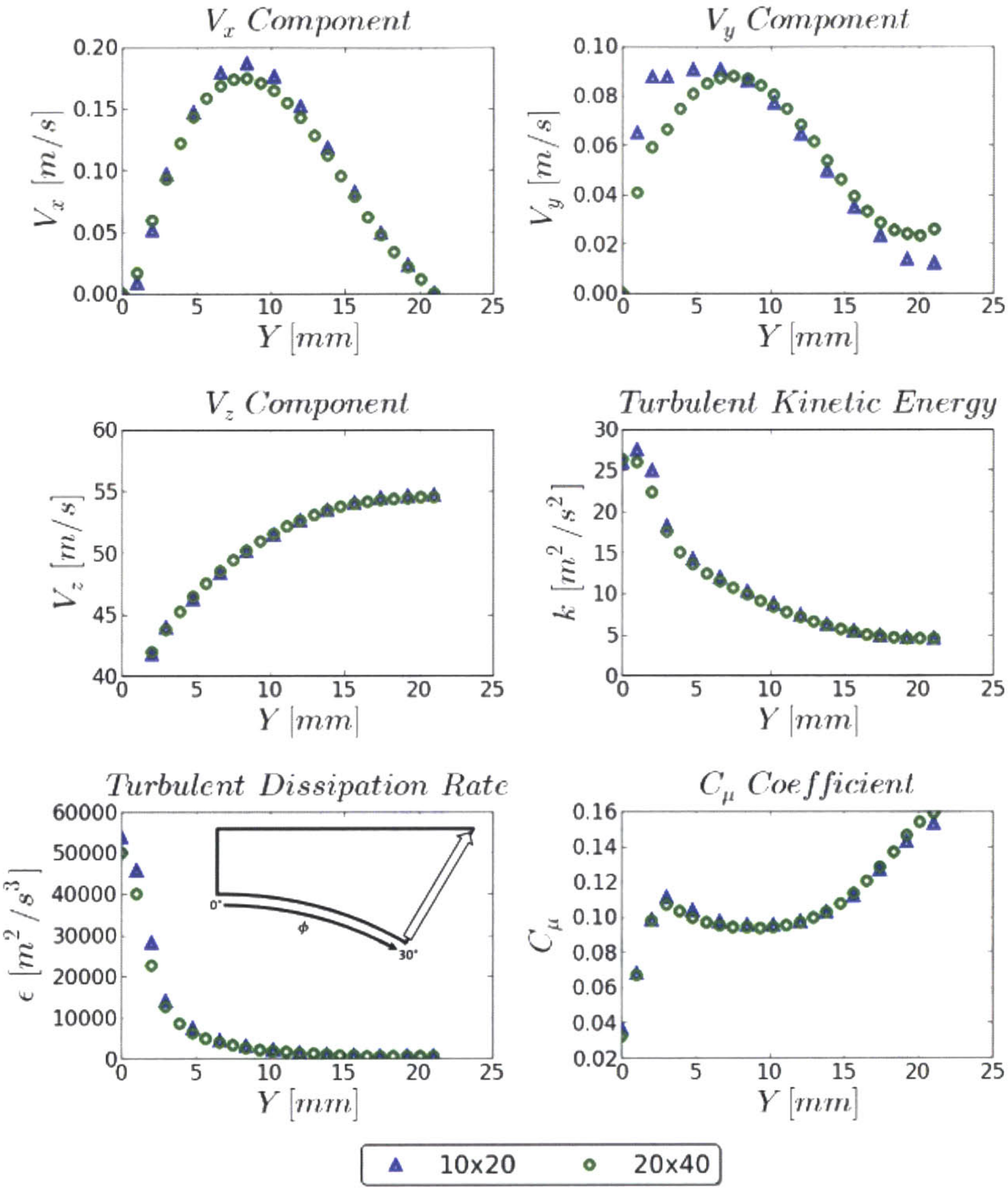

Figure 6.3 Grid convergence using 3 wall layer elements (Mantlik et al. [19] at φ=30°)

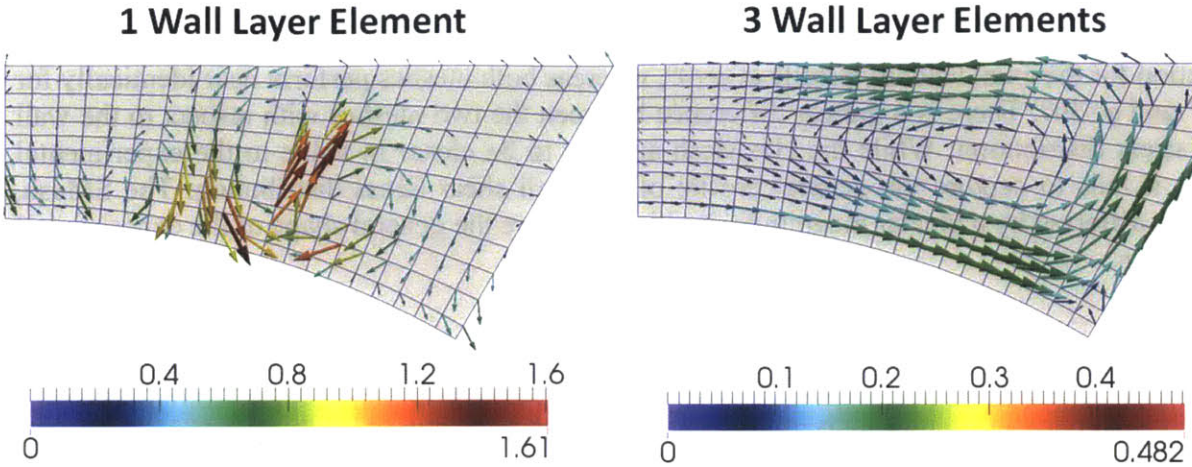

Figure 6.4 Secondary flow magnitudes [m/s] for wall layer element sensitivity study

6.2 Need for Coordinate Symmetry

Recall that in order to specify a symmetry velocity boundary condition in Hydra-TH, the surface normal vector must coincide with a coordinate direction. This feature influenced the creation of the 'SMesh' computational domain that is depicted in Figure 5.1. The 'SMesh' comprises six elementary flow cells and can be computationally expensive as the mesh is progressively refined. It is therefore worthwhile to examine the implications of modeling and simulating one elementary flow cell—which is referred to here as the 'HexMesh'—as the smaller mesh would require fewer computational resources with a faster run-time.

The computational mesh for the HexMesh is shown in Figure 6.5. However, in order to specify the symmetry boundary condition at the slanted wall (sideset 4) both the *x*- and *y*-velocity components need to be set to zero. It was postulated that this would have an impact on the secondary flows and resulting flow profile, both of which are examined here.

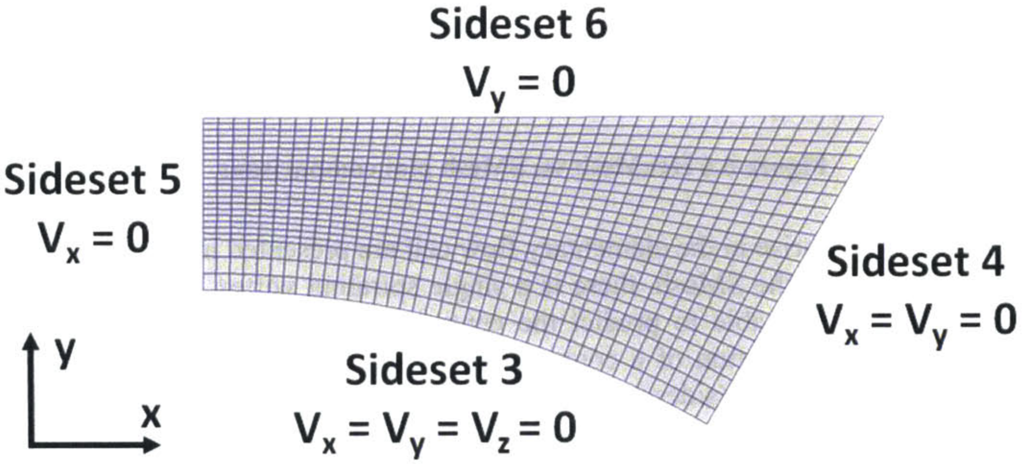

Figure 6.5 Computational domain and boundary conditions for HexMesh

The velocity and wall shear stress distributions for both the SMesh and HexMesh '20x40' fine mesh are plotted in Figure 6.6 for comparison. As can be seen, the SMesh yields a slightly better prediction for the axial velocity profile at φ=0°, whereas both meshes perform near identically for φ=15° and φ=30°. There is a greater difference between the two meshes with respect to the wall shear stress distribution. While the HexMesh appears to be closer in value to the experimental results, it fails to capture the general profile of the wall shear stress distribution. The SMesh, although differing by a greater magnitude, is able to capture the general shape of the experimental distribution.

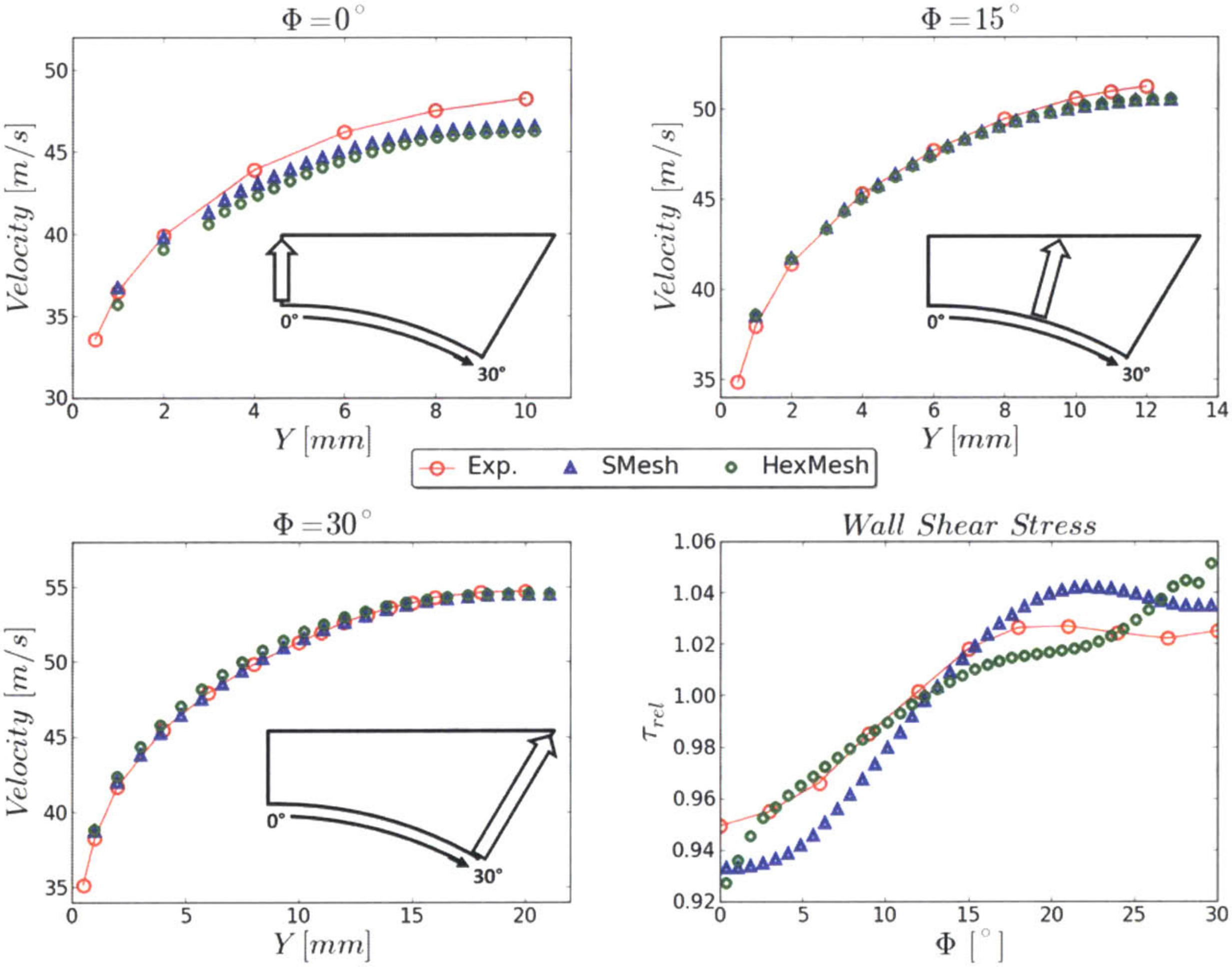

Figure 6.6 HexMesh vs. SMesh plot comparisons

The secondary flows that arise in the elementary flow cell are presented in Figure 6.7 for both the SMesh and HexMesh. For the SMesh, there is a single spiraling vortex that all velocity vectors adhere to. The HexMesh is able to predict the central vortex, however, the proximity to the boundary leads to the formulation of a counterflowing small vortex in the bottom left corner. Further, forcing the slanted wall (sideset 4) velocity components to zero suppresses the secondary flow velocity vectors in the top right corner, which has also forced the core of the vortex further to the left. Together, both of these factors lead to an incorrect prediction of the secondary flows, with a weaker overall magnitude.

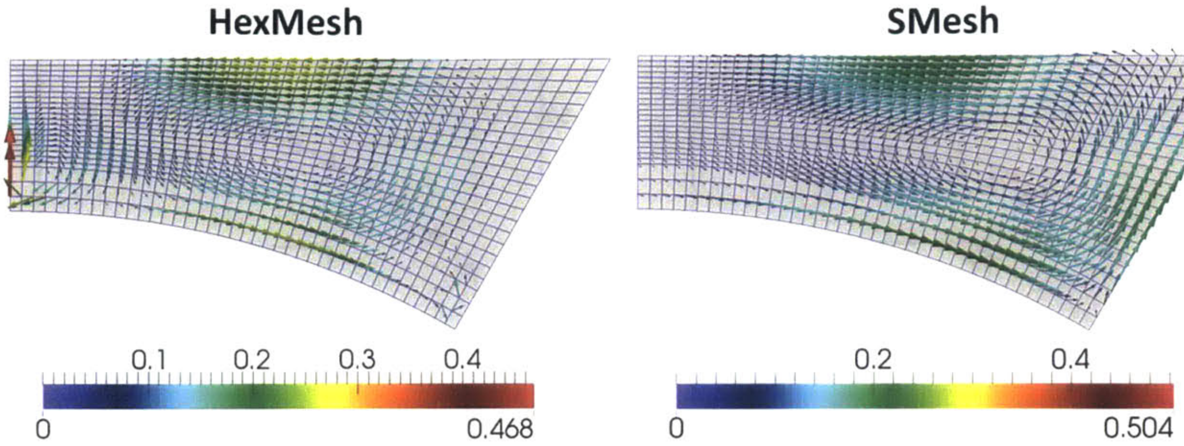

Figure 6.7 Secondary flow magnitudes [m/s] comparison for HexMesh and SMesh

6.3 Axial Refinement

Since Hydra-TH currently does not support a periodic flow boundary condition, it is often necessary to simulate the entire developing length in order to ensure that a fully developed flow has been achieved. This result can lead to a very long flow domain, and great care must be taken when crafting the mesh in the axial (primary) flow direction. It is therefore necessary to utilize an axial meshing scheme that minimizes the number of grids in the axial direction in order to reduce the computational expense. Two such strategies include biasing the mesh using a growth factor and using large aspect ratios.

For the Mantlik et al. [19] test case, a very large aspect ratio was used. It was therefore deemed worthwhile to examine the implications of this by performing an axial grid refinement study for the moderately-refined '10x20x60' grid. Simulations incorporating 120 and 240 axial grids were performed and the resulting velocity and wall shear stress distributions are shown in Figure 6.8. As can be seen, the level of axial refinement has no appreciable impact on the relevant flow quantities as all three refinements overlap one another. Additionally, all three refinements deliver near-identical predictions for the secondary flows (no plot is shown for the sake of brevity). These results serve to suggest that large aspect ratios can be used to reduce the grid size and facilitate quicker run-times without sacrificing the level of accuracy.

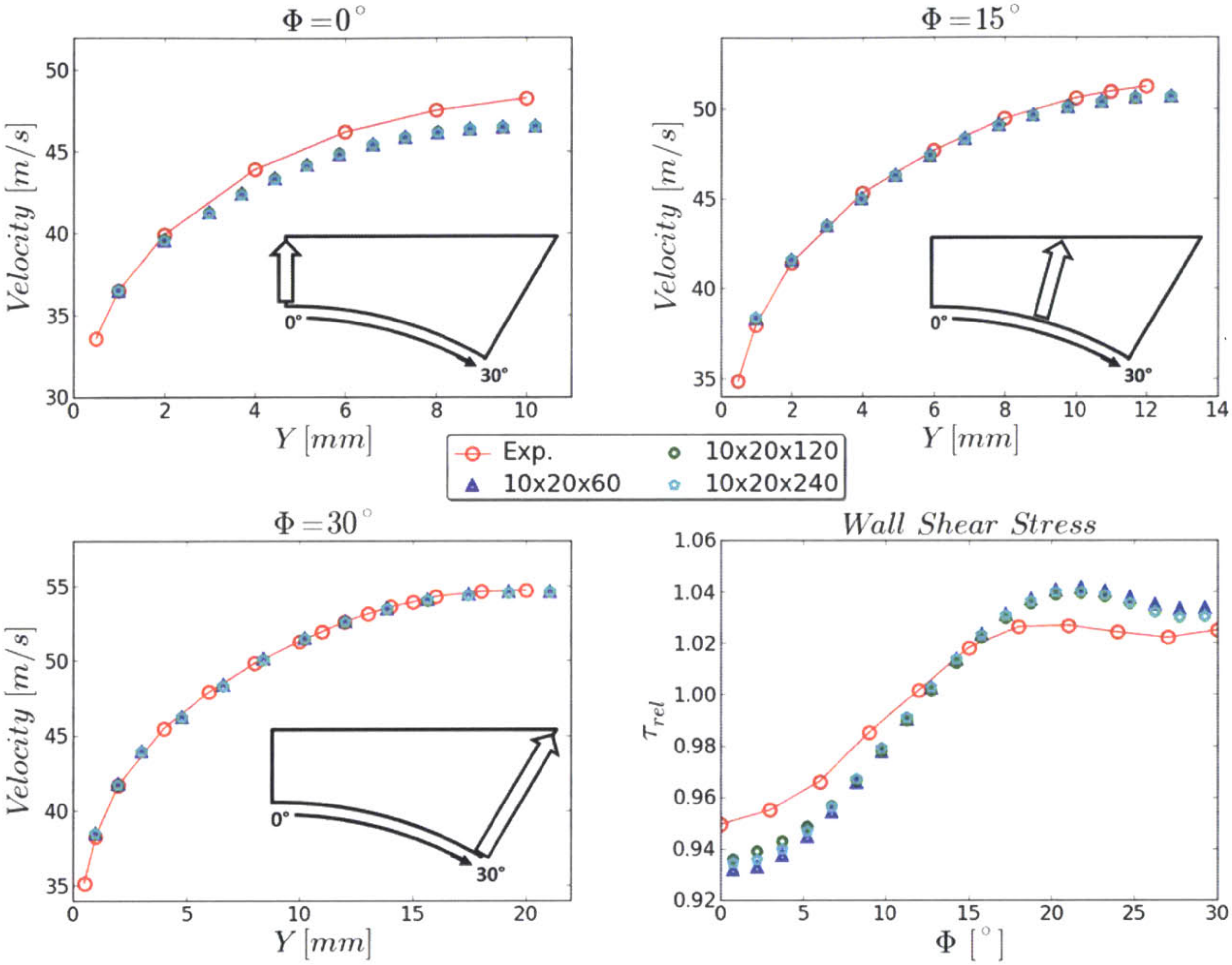

Figure 6.8 Axial refinement study of SMesh

6.4 Impact of Maximum CFL Number on Convergence

The Courant-Friedrichs-Lewy (CFL) number is a necessary condition for convergence when solving certain types of partial differential equations. It arises in the numerical analysis of explicit time integration schemes and assumes the following form for the one-dimensional case:

$$CFL = \frac{u\Delta t}{\Delta x} \tag{6.1}$$

Here, Δt is the time-step, Δx is the grid-spacing, and u is the velocity of the flow in a given cell. The CFL number therefore describes the relationship between the flow speed and the rate at which numerical information can propagate between adjacent cells. For example, if the CFL is below 1, the flow speed is slower than the rate at which the numerical wave can propagate in that cell. Conversely, if the CFL is above 1, the numerical value for the flow is faster than the rate at which numerical information can propagate between cells, which can lead to a divergent simulation if an explicit time integration scheme is employed.

There has been a great deal of effort to equip Hydra-TH with fully-implicit solvers to facilitate very large time-steps (and therefore large CFL numbers), which are demonstrating very promising results [13]. Since steady-state simulations are considered here, the time-step is therefore not related to the solution accuracy, but rather is used as a means to march towards convergence; nonetheless, taking larger time-steps facilitates a quicker approach to a steady-state solution.

In all cases examined in this thesis θ was set equal to 1 in order to achieve a fully-implicit discretization; however, recall from Section 3.3.2 that the quadratic stress terms have been treated explicitly due to the complexity of their formulation. Consequently, there must be some CFL limit above which the simulation fails to converge and/or delivers poor performance. It was therefore desirable to identify this region.

In Hydra-TH, the maximum value of the CFL number to be used during the simulation can be imposed as a constraint in the input control file. Table 6.1 summarizes the range of CFL numbers that were examined for the triangular fuel rod array simulation of the moderately-refined '10x20x60' grid. An initial CFL number of 0.001 was specified and a time-step growth factor of 1.025 was employed. As the simulation progressed, the CFL steadily increased from the initial value of 0.001 to the maximum values listed in Table 6.1. Simulations for maximum CFL numbers of 0.5 and 1 failed to produce a converged solution.

Table 6.1 Maximum CFL numbers examined for sensitivity study

0.1	***0.25***	***0.5***	***1***
Converged	Converged	Failed to Converge	Failed to Converge

The convergence of the global kinetic energy is illustrated in the left plot of Figure 6.9. As can be seen, all four cases behave identically in the beginning of the simulation. This is due to the fact that an initial CFL value of 0.001 was used. As the simulation progresses, and the CFL number is allowed to increase according to the specified time-step growth factor, it is observed that the CFL=0.5 and CFL=1.0 cases diverge, increase, and oscillate. The cases for CFL=0.1 and CFL=0.25 level off and remain constant at a simulation time of 0.05 s, a prime indicator that a converged steady-state solution has been achieved. Note that the CFL=0.1 case is indeed plotted, but is completely overlapped by the CFL=0.25 case.

The residual of the turbulent kinetic energy is shown in the right plot of Figure 6.9. For the CFL=0.1 and CFL=0.25 simulations, the residual steadily declines and stabilizes at a value that is on par with the numerical precision of the computer. Conversely, for the CFL=0.5 and CFL=1.0 cases, the residual oscillates for the duration of the simulation, which further demonstrates that a converged solution has not been attained.

For completeness, the velocity and wall shear stress profiles at the plane of measurement are plotted in Figure 6.10. The CFL=0.5 and CFL=1.0 deliver nonsensical results as the solution failed to converge. Both the CFL=0.1 and CFL=0.25 results are directly mapped atop one another, which serves to suggest that further reduction in the maximum CFL number is not necessary to improve the accuracy of the simulation.

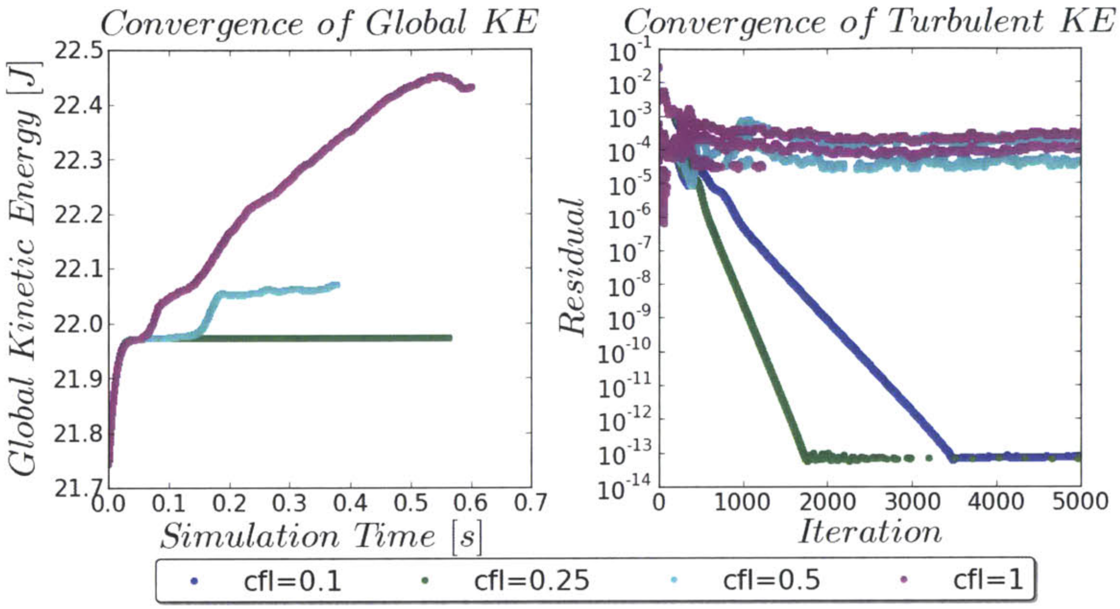

Figure 6.9 Convergence of simulations for CFL study of 10x20x60 mesh

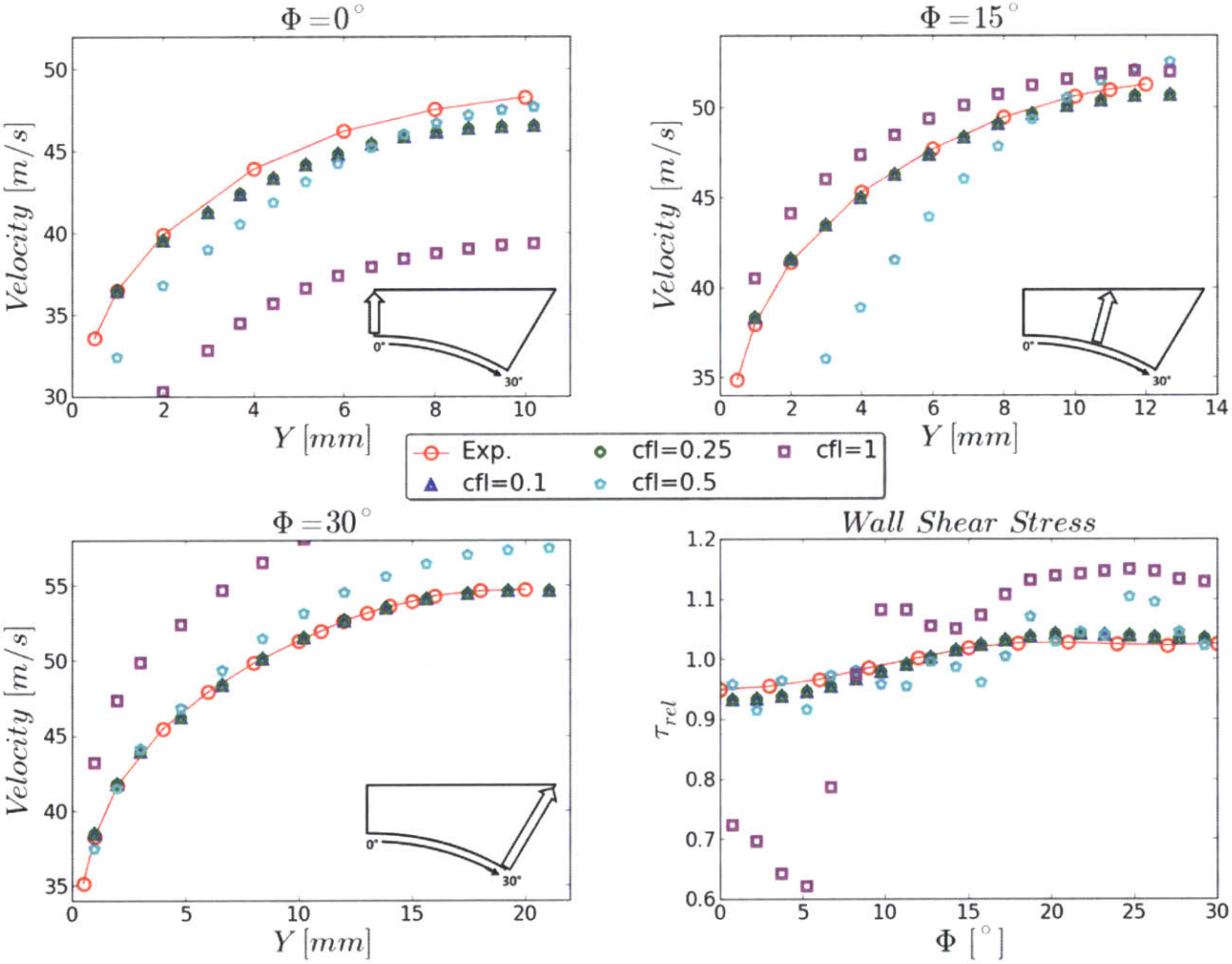

Figure 6.10 CFL study of 10x20x60 SMesh

6.5 Best Practice and Guidelines

In consideration of the sensitivity study results for the triangular fuel rod array experiments of Mantlik et al. [19], the following guidelines for the application of the quadratic model can be derived:

Wall Layer Treatment

- At least 2-3 wall layer elements of the approximate same thickness should be used in order to promote a grid-converged solution that adequately resolves the secondary flows.
- While the results for wall layer elements of 1 mm thickness are presented above, it is worth noting that a thickness of 0.8 mm was also examined, and 2-3 wall layer elements also produced grid-converged solutions.

Computational Domain and Coordinate Symmetry

- If capturing the dominant flow features such as the axial velocity profile is the objective, then the use of a smaller mesh (such as the HexMesh) should be sufficient as it would be computationally cheaper and promote a faster run-time.
- However, if resolving the impact of secondary flows is critical for adequate simulation of the problem, then great care should be taken to construct a geometry that respects the coordinate symmetry (e.g. the SMesh). An example of this includes resolving the wall shear stress distribution, which is used to predict the heat transfer coefficient.

Axial Refinement

- The use of very large aspect ratios does not demonstrate an appreciable impact on the effect and generation of turbulence driven secondary flows that arise from the channel geometry.
- However, this assertion may not be valid when the secondary flows themselves are greatly enhanced by turbulence, such as is the case with mixing vanes on fuel assembly grids. In these instances, greater refinement of the mesh downstream of the mixing vanes is highly advisable, and future work should seek to assess this impact.

Maximum CFL Number and Convergence

- In order to achieve a converged simulation, a maximum CFL in the range of 0.1 – 0.25 should be utilized.
- It is highly advised to begin the simulation with an even smaller CFL number (e.g. 0.001) and employ a time-step growth factor to incrementally increase the CFL number to its maximum specified limit.
- Specification of the maximum time-step (dtmax) can also be a good check as well.

7 Conclusion

The quadratic NLEVM developed by Baglietto and Ninokata [37] has been implemented into Hydra-TH during the course of this work. This model applies a quadratic formulation of the stress-strain relationship that captures the anisotropy of normal stresses and is able to resolve the complex secondary vortices that arise in nuclear reactor fuel assemblies. Restructuring of the code framework and *k*-*ε* class inheritance scheme was required in order to accommodate the incorporation of both the standard and quadratic model implementations.

Model assessment has been performed through simulation of 'classic' engineering test cases including a square duct and U-channel bend. The validation of the quadratic model for fuel related applications has also been performed through simulation of the triangular and square rod array experiments of Mantlik et al. [19] and Hooper and Wood [20]. The quadratic formulation has demonstrated the ability to resolve the complex secondary flow structures as well as predict velocity and wall shear stress distributions. Comparison of the quadratic model with that of the standard model allows for a greater appreciation for the utility of the model, and clearly asserts the need for resolving flow anisotropy.

A rigorous sensitivity study of the triangular fuel rod array experiment by Mantlik et al. [19] has been performed in order to derive guidelines and best practices for the use of the quadratic model to nuclear fuel related applications. The impact of the number of wall layer elements, computational domain and symmetry, axial refinement, and maximum CFL number on the simulation convergence and resulting solution have been explored.

While the objective of this work has been the implementation of the quadratic stress-strain terms to promote high-fidelity nuclear reactor fuel simulations, future work could seek to incorporate the cubic stress-strain terms in order to enhance the overall capabilities of the Hydra-TH package. Further, the capabilities of the symmetry boundary conditions should be enhanced to account for reflection of the quadratic terms as well as to promote symmetry boundary conditions for surfaces that are not coincident with a coordinate direction. Pure wall functions could also be implemented to eliminate the need for extra prism layers, but since experience has shown that two layers are required for good heat transfer predictions this might bring limited advantages.

The results of this work confirm the excellent performance of the quadratic *k*-*ε* model for application to nuclear reactor systems. The quadratic model complements the already validated LES implementation, which together provide a balanced modeling and simulation capability for the Hydra-TH toolkit. Future work should seek to extend the evaluation of the model to realistic fuel assembly configurations, including mixing vane spacers, in order to assess its performance for more complex flow geometries. The model also promises greater generality and its application should also be evaluated for simulation of flow inside the reactor vessel, during both operational and transient conditions.

Appendix A. Hydra-TH Simulation Control Files

A.1 Square Duct

```
title
Square Duct Test Case

cc_navierstokes

 # Time Integration Options
 nsteps  80000
 deltat  0.0001
 term    80.0

 solution_method
   strategy          picard
   itmax             5
   eps               1.E-3
   timestep_control off
   eps_dist          1.0e-5
   eps_p0            1.0e-5
   diagnostics       off
   convergence       on
 end

 time_integration
   type              fixed_cfl
   CFLinit           0.1
   CFLmax            1.0
   dtmax             2.5e-1
   dtscale           1.025
   thetaa            1.0
   thetak            1.0
   thetaf            1.0
 end

 # Output options
 pltype              exodusii
 filetype            distributed
 plti                500
 ttyi                1

 # Material model definition
 material
  id    1
  rho   1.
  mu    1.0e-05
 end

 materialset
 id 1
 material 1
 block 1
 end

 # SIDESETS
 # Sideset 1 - Inlet
 # Sideset 2 - Outlet
 # Sideset 3 - Left Wall
 # Sideset 4 - Top
 # Sideset 5 - Right
 # Sideset 6 - Bottom Wall

 # Turbulence Model
  tmodel nl_ke

  # Simple ICs
  initial
    velx   0.0
    vely   0.0
    velz   0.0
    tke    2.4
    eps    16.8
  end

  # Velocity BCs
  velocity
  # Inlet
     velx sideset 1 -1 0.0
     vely sideset 1 -1 0.0
     velz sideset 1 -1 5.1969
   # Wall
     velx sideset 3 -1 0.0
     vely sideset 3 -1 0.0
     velz sideset 3 -1 0.0
     velx sideset 6 -1 0.0
     vely sideset 6 -1 0.0
     velz sideset 6 -1 0.0
  end

  # Symmetry Vel BCs
  velocity
     vely sideset 4 -1 0.0
     velx sideset 5 -1 0.0
  end

  pressure
     sideset 2 -1 0.0
  end

  distance
    sideset 3 -1 0.0
    sideset 6 -1 0.0
  end

 ppesolver
   type  AMG
   amgpc HYPRE
   strong_threshold 0.85
   solver cg
   smoother ICC
   itmax 500
   itchk 1
   coarse_size 500
   diagnostics off
   convergence off
   eps 1.0e-5
 end

 momentumsolver
   type  ILUFGMRES
   itmax 500
   itchk 1
   restart 20
   diagnostics off
   convergence off
   eps 1.0e-5
 end

 transportsolver
   type  ILUFGMRES
   itmax 500
   itchk 1
   restart 20
   diagnostics off
   convergence off
   eps 1.0e-5
 end

 plotvar
   elem vel
   elem turbke
   elem turbeps
   elem dist
   elem ystar
   elem cmu
   elem pk
   elem turbnu

   node vel
   node pressure
   node dist
   node turbke
   node turbeps
   node turbnu

   side 3 yplus
   side 3 ystar
   side 3 wallshear
   side 3 surfarea

   side 6 yplus
   side 6 ystar
   side 6 wallshear
   side 6 surfarea
 end

 histvar
   elem 305     vel
   elem 139216 vel
 end


exit
```

A.2 U-Channel

```
title
U-Channel

cc_navierstokes

  nsteps  25000
  deltat  0.01
  term    400.00

  time_integration
    type   fixed_cfl
    CFLinit 1.0
    CFLmax  5.0
    dtmax   0.2
    dtscale 1.025
    thetaa  1.0
    thetak  1.0
    thetaf  1.0
  end

  load_balance
    method rcb
  end

  # Output options
  pltype   exodusii
  filetype distributed
  plti   250
  ttyi   25
# prtlev verbose
  dump   1000

  # Turbulence model
  tmodel nl_ke

  # Material model
  material
    id  1
    rho 1.0
    mu  1.0e-6
  end

  materialset
    id 10
    material 1
    block 1
  end

  # Simple IC's
  initial
    velx 0.0
    vely 0.0
    velz 0.0
    tke  0.015
    eps  1.9125
  end

  pressure
    sideset 2 -1 0.0
  end

  distance
    sideset 4 -1 0.0
    sideset 5 -1 0.0
  end

  velocity
    # Inlet
    #velx sideset 1 -1  1.0
    vely sideset 1 -1  0.0
    velz sideset 1 -1  0.0
    user velx sideset 1

    # Walls
    velx sideset 4 -1  0.0
    vely sideset 4 -1  0.0
    velz sideset 4 -1  0.0
    velx sideset 5 -1  0.0
    vely sideset 5 -1  0.0
    velz sideset 5 -1  0.0

    # Front/back symmetry
    velz sideset 3 -1  0.0
  end

  ppesolver
    type  AMG
    amgpc hypre
    itmax 50
    itchk 1
    strong_threshold 0.9
    diagnostics off
    convergence off
    eps  1.0e-5
  end

  momentumsolver
    type  ILUFGMRES
    itmax 50
    itchk 2
    restart 15
    diagnostics off
    convergence off
    eps   1.0e-5
  end

  transportsolver
    type  ILUFGMRES
    itmax 50
    itchk 2
    restart 15
    diagnostics off
    convergence off
    eps   1.0e-5
  end

  plotvar
    elem density
    elem vel
    elem procid
    elem div
    elem turbnu
    elem turbke
    elem turbeps
    node vel
    node pressure
    node turbke
    node turbeps
    node turbnu
    node dist
    node vorticity
    node helicity
    side 4 traction
    side 5 traction
    side 4 wallshear
    side 5 wallshear
    side 4 yplus
    side 5 yplus
    side 4 ystar
    side 5 ystar
    side 4 straction
    side 5 straction
  end

end
exit
```

A.3 Triangular Fuel Rod Array

```
Title
Mantlik Re = 181200

cc_navierstokes

 # Timestep
 nsteps  5000
 deltat   1.0e-4
 term     2.0

 solution_method
   strategy     picard
   itmax         5
   eps          1.E-4
   timestep_control off
   eps_dist     1.0e-5
   eps_p0       1.0e-5
   diagnostics   on
   convergence   on
  end

 time_integration
  type         fixed_cfl
  CFLinit    0.001
  CFLmax     0.25
  dtmax       2.5e-4
  dtscale      1.025
  thetaa       1.0
  thetak       1.0
  thetaf      1.0
 end

 # Output options
  pltype exodusii
  filetype distributed
  plti  1000
  ttyi  1

 # Material model definition
 material
  id  1
  rho 1.131
  mu 1.8e-05
 end

 materialset
  id 1
  material 1
  block 1
 end

# SideSet definitions
# Sideset 1 - Inlet
# Sideset 2 - Outlet
# Sideset 3 - Wall Bottom
# Sideset 4 - Wall Top
# Sideset 5 - Left Vertical
# Sideset 6 - Right Vertical
# Sideset 7 - Left Top
# Sideset 8 - Right Top

# Turbulence Model
 tmodel nl_ke

# Simple ICs
initial
 velx 0.0
 vely 0.0
 velz 0.0
 tke 8.340246
 eps 393.360122391
end

# Velocity BCs
velocity
 # Inlet
  velx sideset 1 -1 0.0
  vely sideset 1 -1 0.0
  velz sideset 1 -1 47.16
 # Wall
  velx sideset 3 -1 0.0
  vely sideset 3 -1 0.0
  velz sideset 3 -1 0.0
  velx sideset 4 -1 0.0
  vely sideset 4 -1 0.0
  velz sideset 4 -1 0.0
end

# Symmetry BCs
velocity
 # Left and Right Vertical
  velx sideset 5 -1 0.0
  velx sideset 6 -1 0.0
 # Left and Right Top
  vely sideset 7 -1 0.0
  vely sideset 8 -1 0.0
end

pressure
 sideset 2 -1 0.0
end

distance
 sideset 3 -1 0.0
 sideset 4 -1 0.0
end

ppesolver
 type  AMG
 amgpc HYPRE
 strong_threshold 0.85
 solver cg
 smoother ICC
 itmax 500
 itchk 1
 coarse_size 500
 diagnostics off
 convergence off
 eps 1.0e-5
end

momentumsolver
 type  ILUFGMRES
 itmax 500
 itchk 1
 restart 20
 diagnostics off
 convergence off
 eps 1.0e-5
end

transportsolver
 type  ILUFGMRES
 itmax 500
 itchk 1
 restart 20
 diagnostics off
 convergence off
 eps 1.0e-5
end

plotvar
 elem vel
 elem turbke
 elem turbeps
 elem dist
 elem ystar
 elem cmu
 elem pk

  node vel
  node pressure
  node dist
  node turbke
  node turbnu
  node turbeps

  side 3 yplus
  side 3 ystar
  side 3 wallshear
  side 3 surfarea
 end

end
exit
```

A.4 Square Fuel Rod Array

```
title
Hooper and Wood

cc_navierstokes

 # Timestep
nsteps  2500
deltat  1.0e-4
term    1.0

solution_method
  strategy    picard
  itmax       5
  eps         1.E-4
  timestep_control off
  eps_dist      1.0e-5
  eps_p0        1.0e-5
  diagnostics   on
  convergence   on
 end

time_integration
 type        fixed_cfl
 CFLinit     0.01
 CFLmax      0.5
 dtmax       2.5e-4
 dtscale     1.025
 thetaa      1.0
 thetak      1.0
 thetaf      1.0
end

# Output options
 pltype exodusii
 filetype distributed
 plti  500
 ttyi  1

 # Turbulence Model
 turbulence nl_ke
 end

 # Material model
 material
  id  1
  rho 1
  mu  1e-5
 end

materialset
 id 1
 material 1
 block 1
end

# Simple IC's
initial
 velx 0.0
 vely 0.0
 velz 0.0
 tke 8.34732150
 eps 394.02782455
end

# Sideset 1 - Inlet
# Sideset 2 - Outlet
# Sideset 3 - Walls
# Sideset 4 - Left Boundary
# Sideset 5 - Top Boundary
# Sideset 6 - Right Boundary
# Sideset 7 - Bottom Boundary

# Velocity BC's
velocity
 # Inlet
  velx sideset 1 -1 0.0
  vely sideset 1 -1 0.0
  velz sideset 1 -1 26.48
 # Wall
  velx sideset 3 -1 0.0
  vely sideset 3 -1 0.0
  velz sideset 3 -1 0.0
 # Left Boundary
  velx sideset 4 -1 0.0
 # Top Boundary
  vely sideset 5 -1 0.0
 # Right Boundary
  velx sideset 6 -1 0.0
 # Bottom Boundary
  vely sideset 7 -1 0.0
end

# Fixed Pressure Outlet
pressure
 sideset 2 -1 0.0
end

distance
  sideset 3 -1 0.0
end

ppesolver
 type  AMG
 amgpc HYPRE
 strong_threshold 0.85
 solver cg
 smoother ICC
 itmax 500
 itchk 1
 coarse_size 500
 diagnostics off
 convergence off
 eps 1.0e-5
end

momentumsolver
 type  ILUFGMRES
 itmax 500
 itchk 1
 restart 20
 diagnostics off
 convergence off
 eps 1.0e-5
end

transportsolver
 type  ILUFGMRES
 itmax 500
 itchk 1
 restart 20
 diagnostics off
 convergence off
 eps 1.0e-5
end

plotvar
 elem vel
 elem turbke
 elem turbeps
 elem dist
 elem ystar
 elem cmu
 elem pk
 node vel
 node pressure
 node dist

 side 3 yplus
 side 3 ystar
 side 3 wallshear
 side 3 surfarea
end

end
exit
```

Appendix B. Experimental Data Measurements

B.1 Square Duct (Hoagland [46])

Table B.1 Hoagland [46] velocity experimental data [m/s]

	x [mm]						
y [mm]	**2.54**	**6.35**	**12.7**	**25.4**	**38.1**	**50.8**	**63.5**
0.254	2.819	2.987	3.459	3.688	3.688	3.688	3.688
0.508	3.780	3.932	4.267	4.511	4.511	4.511	4.511
0.762	4.267	4.478	4.822	4.999	4.999	4.999	4.999
1.27	4.816	4.999	5.371	5.639	5.639	5.639	5.639
2.54	5.090	5.578	6.005	6.309	6.309	6.309	6.309
6.35	5.456	6.309	6.584	7.010	7.010	7.010	7.010
12.7	6.005	6.904	7.498	7.833	7.833	7.833	7.833
25.4	6.218	7.026	7.803	8.534	8.534	8.534	8.717
38.1	6.218	7.026	7.803	8.626	8.900	9.053	9.388
50.8	6.218	7.026	7.803	8.626	9.053	9.449	9.815
63.5	6.218	7.026	7.803	8.626	9.205	9.662	9.997

B.2 U-Channel Bend (Monson et al. [47])

Table B.2 Monson et al. [42] experimental data

Mean Velocity Profiles								Pressure Coefficients			
$\theta=0^\circ$		$\theta=90^\circ$		$\theta=180^\circ$		$s/H=\pi+2$		Inner Wall		Outer Wall	
U/U_m	y/H	U/U_m	y/H	U/U_m	y/H	U/U_m	y/H	s/H	C_p	s/H	C_p
1.222	0.053	1.650	0.011	-0.256	0.020	0.409	0.04	-4.733	-0.04	-4.743	-0.044
1.240	0.074	1.600	0.051	-0.271	0.030	0.471	0.027	-3.534	-0.039	-3.533	-0.045
1.261	0.124	1.529	0.101	-0.249	0.051	0.468	0.049	-1.323	-0.077	-2.348	-0.041
1.251	0.174	1.454	0.154	-0.201	0.061	0.519	0.069	-2.309	-0.044	-1.351	-0.075
1.238	0.205	1.362	0.223	-0.168	0.071	0.568	0.098	-0.004	-0.747	-0.053	0.194
1.230	0.246	1.320	0.250	0.064	0.081	0.595	0.078	2.2	-1.689	0.629	0.498
1.212	0.276	1.270	0.271	0.184	0.111	0.599	0.126	3.018	-1.336	1.269	0.513
1.178	0.294	1.220	0.293	0.466	0.132	0.65	0.169	4.309	-0.694	2.148	0.456
1.161	0.355	1.195	0.324	0.876	0.142	0.771	0.177	5.317	-0.511	2.963	0.002
1.111	0.405	1.162	0.354	0.959	0.159	0.826	0.226	7.712	-0.419	4.28	-0.699
1.088	0.455	1.124	0.372	1.141	0.17	0.889	0.248	6.514	-0.442	5.296	-0.516
1.08	0.505	1.003	0.452	1.137	0.21	0.926	0.268	9.044	-0.424	6.504	-0.449
1.058	0.535	0.970	0.481	1.183	0.23	0.937	0.297	11.335	-0.468	7.713	-0.43
1.05	0.593	0.898	0.551	1.14	0.251	0.968	0.328	10.216	-0.44	9.017	-0.431
1.018	0.614	0.873	0.569	1.148	0.281	1.019	0.368			10.202	-0.453
0.987	0.653	0.869	0.590	1.151	0.322	1.057	0.399			11.293	-0.472
0.979	0.693	0.840	0.630	1.115	0.39	1.095	0.439				
0.97	0.723	0.777	0.673	1.108	0.423	1.137	0.479				
0.938	0.752	0.752	0.699	1.085	0.473	1.164	0.51				
0.921	0.784	0.697	0.739	1.054	0.504	1.164	0.53				
0.898	0.793	0.71	0.761	1.042	0.544	1.216	0.581				
0.848	0.823	0.681	0.779	1.028	0.585	1.195	0.61				
0.848	0.84	0.68	0.801	1.006	0.625	1.219	0.63				
0.827	0.871	0.647	0.838	0.996	0.656	1.236	0.681				
0.788	0.891	0.597	0.87	0.984	0.676	1.246	0.749				
0.767	0.9	0.642	0.888	0.968	0.727	1.256	0.8				
0.705	0.92	0.63	0.91	0.951	0.764	1.246	0.851				
0.653	0.95	0.596	0.941	0.946	0.823	1.246	0.9				
0.625	0.969	0.579	0.96	0.922	0.856	1.266	0.929				
0.572	0.98	0.55	0.981	0.904	0.904	1.218	0.951				
						1.197	0.969				

B.3 Triangular Fuel Rod Array (Mantlik et al. [19])

Table B.3 Mantlik et al. [19] experimental data (Re = 181,200)

Wall Distance [mm]	Velocity [m/s]			Angle [°]	Wall Shear Stress [Pa]
	φ=0°	φ=15°	φ=30°		
0.5	33.58	34.86	35.17	0	4.972
1	36.51	37.96	38.24	3	5.001
2	39.88	41.41	41.7	6	5.059
4	43.89	45.28	45.47	9	5.159
6	46.21	47.68	47.92	12	5.246
8	47.52	49.44	49.81	15	5.332
10	48.27	50.6	51.3	18	5.375
11		50.97	51.96	21	5.378
12		51.24	52.62	24	5.364
13			53.14	27	5.353
14			53.59	30	5.368
15			53.92		
16			54.3		
18			54.62		
20			54.71		

B.4 Square Fuel Rod Array (Hooper and Wood [20])

Table B.4 Hooper and Wood [20] experimental data (Re = 207,600)

$\varphi=0°$		$\varphi=45°$		Angle [°]	τ_{rel}
Y/Y_{max}	U/U_0	Y/Y_{max}	U/U_0		
0.266	0.754	0.048	0.881	0	0.841
0.334	0.761	0.076	0.907	5	0.855
0.400	0.779	0.100	0.946	10	0.888
0.532	0.812	0.124	0.972	15	0.933
0.666	0.834	0.151	0.990	20	0.981
0.800	0.851	0.175	1.010	25	1.041
0.935	0.867	0.224	1.044	30	1.066
		0.278	1.065	35	1.114
		0.328	1.087	40	1.135
		0.381	1.106		
		0.454	1.126		
		0.531	1.150		
		0.607	1.160		
		0.683	1.168		
		0.757	1.176		
		0.834	1.184		
		0.960	1.182		

References

[1] C. Trupp and R. S. Azad, "The structure of turbulent flow in triangular array rod bundles," *Nuclear Engineering and Design,* vol. 32, no. 1, pp. 47-84, 1975.

[2] P. Carajilescov and N. E. Todreas, "Experimental and Analytical Study of Axial Turbulent Flows in an Interior Subchannel of a Bare Rod Bundle," *J. Heat Transfer,* vol. 98, no. 2, 1975.

[3] K. Rehme, "Experimental observations of turbulent flow through subchannels of rod bundles," *Experimental Thermal and Fluid Science,* vol. 2, no. 3, pp. 341-349, 1989.

[4] J. Nikuradse, "Untersuchung ueber die Geschwindigkeitsverteilung in turbulenten Stroemungen," Diss. Gottingen, 1926.

[5] V. Vonka, "Measurement of secondary flow vortices in a rod bundle," *Nuclear Engineering and Design,* vol. 106, no. 2, pp. 191-207, 1988.

[6] J. L. Lumley, "Toward a turbulent constitutive relation," *J. Fluid Mechanics,* vol. 41, no. 2, pp. 413-434, 1970.

[7] S. B. Pope, "A more general effective-viscosity hypothesis," *J. Fluid Mechanics,* vol. 72, no. 2, pp. 331-340, 1975.

[8] E. Baglietto, "Anisotropic Turbulence Modeling for Accurate Rod Bundle Simulations," in *Proceedings of 14th International Conference on Nuclear Engineering (ICONE14)*, Miami, Florida, July 17-20, 2006.

[9] E. Baglietto and H. Ninokata, "A turbulence model study for simulating tight lattice rod bundles," *Nuclear Engineering and Design,* vol. 235, no. 7, pp. 773-784, 2005.

[10] T. J. Barth and C. J. D., "The design and application of upwind schemes on unstructured meshes," in *AIAA 27th Aerospace Sciences Meeting,* Reno, Nevada, January 9-12, AIAA-89-0366, 1989.

[11] P. M. Gresho, "On the theory of semi-implicit projection methods for viscous incompressible flow and its implementation via a finite element method that also introduces a nearly consistent mass matrix. part 1: Theory," *Int. J. Numerical Methods in Fluids,* vol. 11, no. 5, pp. 587-620, 1990.

[12] P. M. Gresho and S. T. Chan, "On the theory of semi-implicit projection methods for viscous incompressible flow and its implementation via a finite element method that also introduces a nearly consistent mass matrix. part 2: Implementation," *Int. J. Numerical Methods in Fluids,* vol. 11, no. 5, pp. 621-659, 1990.

[13] R. Nourgaliev, M. Christon, J. Bakosi and A. Bui, "Newton-Krylov Based P2 Projection Solver for Fluid Flows," Tech. Rep. INL/EXT-13-28278, Idaho National Laboratory, June 2013.

[14] J. Bakosi, M. A. Christon, L. Pritchett-Sheats, B. T. Nadiga, Y. Xia, C. Wang, H. Luo and R. Nourgaliev, "Hydra-TH Verification, Validation and Thermal-Hydraulics Benchmark Problems," Tech. Rep. LA-UR-14-23461, Los Alamos National Laboratory, revised 2014.

[15] J. Bakosi, M. A. Christon, R. B. Lowrie, L. A. Pritchett-Sheats and R. R. Nourgaliev, "Large-Eddy Simulations of Turbulent Flow for Grid-to-Rod Fretting in Nuclear Reactors," Tech. Rep. LA-UR 12-26572, Los Alamos National Laboratory, 2013.

[16] A. Bui and H. Zhang, "Hydra-TH Simulation of Single-Phase Flow and Heat Transfer in a Rod Bundle Segment," Tech. Rep. INL/EXT-13-28747, Idaho National Laboratory, 2013.

[17] E. Baglietto and M. A. Christon, "Single Phase Validation of Hydra-TH for Fuel Applications," CASL Tech. Rep. CASL-U-2014-0154-000, 2014.

[18] T. Smith, "A Multi-Year Plan for Enhancing Turbulence Modeling in Hydra-TH," 2015.

[19] F. Mantlik, J. Heina and J. Chervenka, "Results of local measurements of hydraulic characteristics in triangular pin bundle," UJV-3778-R, Rzez, Czech Republic, 1976.

[20] J. D. Hooper and D. H. Wood, "Fully developed rod bundle flow over a large range of Reynolds number," *Nuclear Engineering and Design,* vol. 83, no. 1, pp. 31-46, 1984.

[21] P. R. Spalart and S. R. Allmaras, "A one-equation turbulence model for aerodynamic flows," AIAA Paper 1992-0439, 1992.

[22] S. B. Pope, Turbulent Flows, Cambridge University Press, 2000.

[23] B. E. Launder and B. I. Sharma, "Application of the energy-dissipation model of turbulence to the calculation of flow near a spinning disc," *Letters in Heat and Mass Transfer,* vol. 1, no. 2, pp. 131-137, 1974.

[24] D. C. Wilcox, "Turbulence modeling for CFD," La Canada, CA: DCW Industries, 1993.

[25] C. G. Speziale, R. Abid and E. C. Anderson, "Critical Evaluation of Two-Equation Models for Near-Wall Turbulence," *AIAA Journal,* vol. 30, no. 2, pp. 324-331, 1992.

[26] F. R. Menter, "Two-Equation Eddy-Viscosity Turbulence Models for Engineering Applications," *AIAA Journal,* vol. 32, no. 8, pp. 1598-1605, 1994.

[27] J. C. Rotta, "Statische theorie nichtomogener turbulenz," *Z. Phys,* vol. 129, pp. 547-572, 1951.

[28] B. Launder, G. Reece and W. Rodi, "Progress in the development of a reynolds-stress turbulence closure," *J. Fluid Mechanics,* vol. 68, no. 3, pp. 537-566, 1975.

[29] M. M. Gibson and B. E. Launder, "Ground effects on pressure fluctuations in the atmospheric boundary layer," *J. Fluid Mechanics,* vol. 86, no. 3, pp. 491-511, 1978.

[30] C. G. Speziale, S. Sarkar and T. B. Gatski, "Modelling the pressure-strain correlation of turbulence: an invariant dynamical systems approach," *J. Fluid Mechanics,* vol. 227, pp. 245-272, 1991.

[31] P. A. Durbin and B. A. Reif, Statistical Theory and Modeling for Turbulent Flows, Wiley, 2011.

[32] W. Rodi, "The Prediction of Free Turbulent Boundary Layers Using a Two-equation Model of Turbulence," Ph.D. Thesis, Imperial College, London, 1972.

[33] W. Rodi, "A new algebraic relation for calculating the Reynolds stresses," *ZAMM,* vol. 56, pp. 219-232, 1976.

[34] T. H. Shih, J. Zhu and J. L. Lumley, "A Realizable Reynolds Stress Algebraic Equation Model," NASA TM-105993, 1993.

[35] T. J. Craft, B. E. Launder and K. Suga, "Development and application of a cubic eddy-viscosity model of turbulence," *Int. J. Heat and Fluid Flow,* vol. 17, pp. 108-115, 1996.

[36] F. S. Lien, W. L. Chen and M. A. Leschziner, "Low-Reynolds-Number Eddy-Viscosity Modelling Based on Non-Linear Stress-Strain/Vorticity Relations," in *Proc. 3rd Symposium on Engineering Turbulence Modelling and Experiments*, Crete, 1996.

[37] E. Baglietto and H. Ninokata, "Anisotropic Turbulence Modeling for Application to Industrial Engineering Internal Flows," *Int. J. Transport Phenomena,* vol. 8, no. 2, pp. 85-101, 2006.

[38] W. P. Jones and B. E. Launder, "The prediction of laminzarization with a two-equation model of turbulence," *Int. J. Heat Mass Transfer,* vol. 15, pp. 301-314, 1972.

[39] B. I. Davidov, "On the statistical dynamics of an incompressible turbulent fluid," *Dok. Akad. Nauk S.S.S.R.,* vol. 136, pp. 47-50, 1961.

[40] F. H. Harlow and P. I. Nakayama, "Transport of turbulence energy decay rate," University of California Report LA-3854, Los Alamos Science Laboratory, 1968.

[41] K. Hanjalic, "Two-dimensional Asymmetric Turbulent Flow in Ducts," Ph.D. Thesis, University of London, 1970.

[42] V. Yakhot, S. A. Orszag, S. Thangam, T. B. Gatski and C. G. Speziale, "Development of turbulence models for shear flows by a double expansion technique," *Physics of Fluids,* vol. 4, no. 7, pp. 1510-1520, 1992.

[43] T. H. Shih, W. Liou, A. Shabbir, Z. Yang and J. Zhu, "A new k-e eddy viscosity model for high reynolds number turbulent flows," *Computers and Fluids,* vol. 24, pp. 227-238, 1995.

[44] L. F. Richardson, "The approximate arithmetical solution by finite differences of physical problems including differential equations, with an application to the stresses in a masonry dam," *Philosophical Transactions of the Royal Society,* vol. 210, pp. 459-470, 1911.

[45] L. F. Richardson and J. A. Gaunt, "The deferred approach to the limit," *Philosophical Transactions of the Royal Society,* vol. 226, pp. 636-646, 1927.

[46] L. C. Hoagland, "Fully developed turbulent flow in straight rectangular ducts: secondary flow, its cause and effect on the primary flow," Ph.D. Thesis, Massachusetts Institute of Technology, 1960.

[47] D. Monson, H. Seegmiller, P. McConnaughey and Y. Chen, "Comparison of Experiment with Calculations Using Curvature-Corrected Zero and Two Equation Turbulence Models for a Two-Dimensional U-Duct," AIAA 90-1484, 1990.

[48] M. L. Shur, M. K. Strelets, A. K. Travin and P. R. Spalart, "Turbulence Modeling in Rotating and Curved Channels: Assessing the Spalart-Shur Correction," *AIAA Journal,* vol. 38, no. 5, pp. 784-792, 2000.

[49] T. M. Smith and M. A. Christon, "Enhanced Turbulence Model Capabilities in Hydra-TH," L3 Milestone THM.CFD.P9.06, 2015.

[50] M. A. Christon, J. Bakosi, M. M. Francois and R. Nourgaliev, "Hydra-TH Theory Manual," Tech. Rep. LA-UR-11-05387, Los Alamos National Laboratory, revised November 2013.